TUM School of Natural Sciences
TECHNISCHE UNIVERSITÄT MÜNCHEN

3D impurity transport and dynamic wall evolution in the fusion experiment ASDEX Upgrade

Lennart Bock

Vollständiger Abdruck der von der TUM School of Natural Sciences der Technischen Universität München zur Erlangung des akademischen Grades eines Doktors der Naturwissenschaften (Dr. rer. nat.) genehmigten Dissertation.

Vorsitz:	Prof. Dr. Martin Zacharias
Prüfer*innen der Dissertation:	1. Prof. Dr. Ulrich Stroth
	2. Prof. Dr. Sebastijan Brezinsek

Die Dissertation wurde am 23.03.2023 bei der Technischen Universität München eingereicht und durch die TUM School of Natural Sciences am 13.06.2023 angenommen.

Abstract

In magnetic confinement fusion experiments, the generated heat and particle fluxes from the plasma onto the vessel walls can exceed material limits. Radiative cooling via injection ("seeding") of small amounts of nitrogen into the plasma edge has been proven to be an effective measure to limit these fluxes in the tokamak experiment ASDEX Upgrade (AUG). This nitrogen is partially stored in the surface layers of the tungsten walls and re-enters the plasma after being eroded due to heat and particle loads on the wall elements. To effectively control the radiation induced by nitrogen in the plasma, a model for nitrogen retention in the wall and nitrogen fluxes into the plasma is required.
Previous work has successfully demonstrated the applicability of the WallDYN simulation scheme coupled to 2D plasma and impurity transport simulations to interpret the retention of nitrogen in the divertor region of AUG, where a tokamak is essentially toroidally symmetric. However, at the outer mid-plane, where probes and limiters break this symmetry, the nitrogen deposition as computed by WallDYN coupled to 2D models for plasma and impurity transport was overestimated by at least one order of magnitude.
This work aims to investigate the influence of non toroidally symmetric first wall geometries on both the background plasma solution and the finally resulting migration of nitrogen. To that end the 3D plasma modelling code EMC3-EIRENE and the recently developed WallDYN-3D scheme are applied to AUG thereby resolving the 3D geometry of its first wall.
The influence of the 3D geometry on the plasma backgrounds is investigated by modelling a AUG discharge, where nitrogen was seeded from the divertor dome. In these calculations different approximations of the first wall are compared: a 2D case with a toroidally symmetric wall geometry and a 3D case that includes poloidal rib limiters and a mid-plane collector probe. First, the input parameters for perpendicular transport are adjusted such, that the simulated plasma solution in 3D wall geometry matches the available experimental data. Then, using the same input parameters, the simulations are repeated in 2D geometry and the resulting 2D plasma solution is compared to the 3D solution. In previous work the same discharge has been modelled with a 2D toroidally symmetric first wall and a 2D plasma modelling code, but the nitrogen areal densities found experimentally by ion beam analysis on the outer mid-plane manipulator could not be matched by simulations. The explanation then was that the 3D geometry of the manipulator could not be properly approximated in the 2D calculation. To test this hypothesis the simulated plasma background in full 3D wall geometry is used in 3D WallDYN simulations to calculate the nitrogen deposition at the mid-plane collector probe and in the divertor.
The influence of the poloidal position of the seeding location on nitrogen deposition in the divertor and on the mid-plane collector probe is then investigated in a set of dedicated AUG discharges. During these discharges also the fluence

dependence of nitrogen accumulation on the manipulator is investigated by exposing different positions of the manipulator to different numbers of identical discharges. These discharges are then modeled using EMC3-EIRENE with 3D wall geometry and the resulting plasma backgrounds are used in 3D WallDYN calculations of the nitrogen deposition on the manipulator and divertor.
The findings in this work resolve discrepancies between simulated nitrogen deposition profiles and experimentally obtained results at the outer mid-plane manipulator of AUG, by extending the simulation models to 3D. They further highlight the importance of including 3D geometry for impurity transport in the plasma edge and underline the crucial role of neutral particles in simulations.

Zusammenfassung

In Fusionsexperimenten, die auf magnetischem Einschluss basieren, überschreiten Wärme- und Teilchenflüsse aus dem Plasma schnell die Materialgrenzen der Wandelemente. Im Tokamak experiment ASDEX Upgrade (AUG) wurde gezeigt, dass Strahlungskühlung durch das Einbringen kleiner Mengen von Stickstoff in den Plasmarand, eine effektive Maßnahme zum Kontrollieren dieser Flüsse ist. Dieser eingebrachte Stickstoff lagert sich teilweise in den oberen Schichten der Wolframwand ab und wird wieder in das Plasma eingebracht, nachdem er durch die Wärme- und Teilchenbelastung der Wandelemente erodiert ist. Zur effektiven Kontrolle der Strahlung durch Stickstoff ist daher ein Modell zur Stickstoffanreicherung in der Wand und der Stickstoffemission aus der Wand nötig.
In früheren Untersuchungen wurde die Anwendbarkeit des WallDYN Simulationsschemas, gekoppelt an 2D Codes für Plasma- und Verunreinigungstransport, bei der Anreicherung von Stickstoff im Divertor demonstriert. Während ein Tokamak im Divertor im Wesentlichen toroidal symmetrisch ist, brechen Sonden und Limitierer diese Symmetrie an der äußeren Mittelebene. In diesen Bereichen wird die Anreicherung von Stickstoff durch WallDYN um mindestens eine Größenordnung überschätzt, wenn 2D Modelle verwendet werden.
In dieser Arbeit wird der Einfluss einer nicht toroidal symmetrischen Wandgeometrie auf simulierte Plasmalösungen und der resultierenden Migration von Stickstoff untersucht. Dazu wird der 3D Plasma-Modellierungs-Code EMC3-EIRENE und das neu entwickelte WallDYN-3D Schema auf AUG angewendet, um die 3D Geometrie der ersten Wand aufzulösen.
Der Einfluss der 3D Geometrie auf simulierte Plasmalösungen wird durch die Modellierung einer AUG Entladung untersucht, bei der Stickstoff im Divertor eingeleitet wurde. In diesen Rechnungen werden verschiedene Näherungen der Geometrie der ersten Wand verglichen: Eine 2D Variante mit einer toroidal symmetrischen Wandgeometrie and eine 3D Variante, mit poloidalen rib Limitierern und einer Kollektorsonde an der äußeren Mittelebene. Im ersten Schritt wurden die Eingabeparameter für den senkrechten Transport so angepasst, dass die simulierte Plasmalösung in 3D Wandgeometrie und die vorhandenen experimentellen Daten übereinstimmen. Dann wurde die Simulation mit identischen Inputparametern in 2D Wandgeometrie wiederholt und die resultierende 2D Plasmalösung wird mit der 3D Lösung verglichen.
In früheren Untersuchungen wurde die selbe Entladung mit einer 2D toroidal symmetrischen Wand und einem 2D Plasma-Modellierungs-Code untersucht. Dabei haben die simulierten Flächendichten von Stickstoff am Mittelebenenmanipulator die mit Ionenstrahlanalyse bestimmten Ergebnisse weit überschätzt. Die Erklärung dafür war, dass die 3D Geometrie des Mittelebenenmanipulator nicht in den 2D Rechnung abgebildet werden konnte. Um diese Hypothese zu überprüfen, wurde die Plasmalösung in 3D Wandgeometrie in

WallDYN-3D Simulationen genutzt, um die Stickstoffdeposition am Mittelebenenmanipulator und im Divertor zu berechnen.
Der Einfluss der poloidalen Position des Stickstoffventils auf die Stickstoffdeposition im Divertor und am Mittelebenenmanipulator wird in einer weiteren AUG Entladungsreihe untersucht. Während dieser Entladungen wurde außerdem die Abhängigkeit der Stickstoffdeponierung von der Fluenz am Mittelebenenmanipulator untersucht, indem verschiedene Positionen am Mittelebenenmanipulator unterschiedlich vielen Entladungen ausgesetzt werden. Diese Entladungen werden dann mit EMC3-EIRENE in 3D Wandgeometrie modelliert und die resultierenden Plasmalösungen werden in WallDYN-3D Rechnungen genutzt, um die Stickstoffdeponierung am Mittelebenenmanipulator und im Divertor zu berechnen.
Die Ergebnisse in dieser Arbeit klären Unstimmigkeiten zwischen simulierter Stickstoffdeponierung und experimentellen Ergebnissen am Mittelebenenmanipulator von AUG durch die Erweiterung der Simulationsmodelle auf 3D Geometrien. Sie verdeutlichen weiterhin die Bedeutung von 3D Geometrie für Verunreinigungstransport im Plasmarand und belegen die wichtige Rolle von Neutralteilchen in Simulationen.

Contents

Chapter 1

Background and motivation

In times of rapidly changing climate the need for sustainable energy sources is rising to ensure a working infrastructure and to cope with humanity's growing energy demands. Common renewable sources like solar and wind are on the rise, but their intermittency and dependence on favourable weather conditions are struggling with providing a base power load. Nuclear fusion, the power source of the sun, is a promising candidate to provide this base power load in the future and could shape the energy landscape combined with intermittent energy sources. Additionally, nuclear fusion is extremely efficient: 1 g of fusion fuel delivers as much energy as 10 t of coal [1]. Fusion power plants would therefore run with very small amounts of fuel and are inherently safe as the energy providing fusion reaction is a non cascading reaction and can only be sustained if external parameters are favourable. However, the technologically feasibility of a power plant based on nuclear fusion has not yet been demonstrated.

A very promising fusion reaction to achieve a net energy gain in a reactor on earth is the fusion of deuterium (D or ^{2}H) and tritium (T or ^{3}H), which can be achieved by heating up a D-T mixture to a temperature of about 100 million Kelvin. At these temperatures matter turns into a plasma, where electrons are no longer bound to their nuclei. In magnetic confinement fusion devices the plasma is confined by magnetic fields inside a vacuum chamber and is heated by external heating systems. With devices in the tokamak configuration, temperatures and densities to achieve net energy gain were in principle already achieved [2], but instabilities arising in the plasma thus far prevent actual net energy gain. Next generation fusion experiments like ITER in the EU or SPARC in the US are currently under construction and are explicitly aiming to demonstrate net energy gain by magnetic confinement fusion devices.

Even if the plasma performs well, another fundamental challenge related to high power and particle fluxes reaching the wall, has to be solved. The power load can damage the wall material and particles bombarding the wall lead to erosion of the wall material and accumulation of impurities in the plasma, which leads to worse performance. To reduce the accumulation of impurities

in the central plasma, the region of strong plasma-wall interaction is directed away from the plasma onto specifically designed target plates, often consisting of tungsten for its favourable properties under high heat loads. This design is called divertor configuration and has the disadvantage of focusing the power and particle loads from the plasma onto a small area, which can easily exceed material limits [3]. Therefore so called radiative cooling is employed, where gaseous impurities are seeded into the edges of the plasma to cool it down before it reaches the target plates, and consequentially reduce the loads onto the target plates while maintaining the plasma performance [4].

A prominent choice for such a gaseous species is nitrogen. Impurities such as nitrogen interact with the wall, adding a layer of complexity to the plasma-wall interaction. In the case of tungsten as a wall material and nitrogen as seeding impurity, the implantation of nitrogen ions into the wall leads to the formation of tungsten nitride layers [5] that are re-eroded by impinging particles from the plasma. The wall in fusion experiments therefore acts as a history dependent source for impurities. Hence, to optimize radiation control and plasma performance, it is required to understand the retention and release of impurities from the wall.

Re-eroded particles are transported through the plasma and eventually are re-deposited, leading to a cycle of erosion, transport through the plasma and deposition which is called impurity migration [6–8]. Impurity migration leads to changes in the wall composition and hence controls the net erosion of the walls and formation of mixed materials with potentially unfavourable properties (e.g. more brittle, less resistance to heat). Additionally, during the re-deposition of material layers, radioactive tritium can be incorporated into the wall. While the fusion reaction itself does not lead to radioactive waste, the activation of wall materials via high-energy neutron impact and the incorporation of radioactive tritium result in radioactive in-vessel components.

In previous experiments, the migration of nitrogen has been investigated with probes in the divertor and at the outer mid-plane in the ASDEX Upgrade (AUG) tokamak at the Max Planck Institute for Plasma Physics in Garching. It has been shown that results from 2D impurity migration modelling can successfully reproduce experimentally obtained deposition profiles of nitrogen at the target plates in the divertor [9–11], but they overestimate deposition at the mid-plane above the target plates [12]. A suspected reason is the missing influence of 3D geometrical features, which can only be included if the applied modelling scheme is extended to 3D geometries.
In this work, the results of 3D impurity migration simulations of nitrogen in AUG are presented and calculated areal densities are compared to experimental results obtain from nuclear reaction analysis. As a first step, the plasma discharge carried out in a previous work on AUG [12] was analysed and another set of nitrogen seeded discharges was carried out to investigate the discharge resolved deposition profiles of nitrogen at the mid-plane utilising the rotating collector probe of the mid-plane manipulator system and to investigate

the possible influence of a different seeding location. Additional samples were exposed to the plasma at the target plates with the divertor manipulator system to compare experimental and simulated areal densities of nitrogen at two points simultaneously. The newly exposed probes at the mid-plane and in the divertor were analysed with nuclear reaction analyses (NRA) to determine the areal density of deposited nitrogen.
In a next step, 3D simulations of the plasma edge are conducted with the fluid code package EMC3-EIRENE (section 4.1) and the influence of 3D geometrical features on the plasma is investigated numerically. The simulation results serve as a basis to run the impurity migration code WallDYN (section 4.3), which recently has been extended to 3D geometries [13]. To include depth profile effects during nitrogen deposition, results obtained from WallDYN are used as an input for the SDTrimSP code (see section 4.2) that calculates particle trajectories in solids based on the binary collision approximation. Areal densities obtained from the combination of WallDYN and SDTrimSP are then compared to experimentally obtained areal densities to be able to interpret nitrogen migration outside the divertor and in 3D.
The structure of the thesis is as follows: In chapter 2 the fundamental idea of nuclear fusion in magnetic confinement devices, the tokamak configuration, the transport physics in the edge of the plasma and the physics of plasma-wall interactions are introduced. The experimental methods and setups, like nuclear reaction analysis and the tokamak AUG, are described in chapter 3. Chapter 3.5 then presents the results obtained from laboratory experiments and AUG. The simulation codes and applied models are described in chapter 4 and the results obtained from these simulation codes are shown in chapter 5. At the end, a discussion summarises obtained results in chapter 6.

Chapter 2

Magnetic Confinement Fusion, Transport Physics and Plasma-Wall Interaction

In this chapter, the concept of nuclear fusion is introduced together with the approach of magnetic confinement as a means to utilize the energy of nuclear fusion on earth. Afterwards a theoretical description of the behaviour of plasma in magnetic confinement devices is briefly explained and in the last part the physics of the interaction between this plasma and the wall of magnetic confinement devices is introduced.

2.1 Nuclear fusion and magnetic confinement

Nuclear fusion is the process of nuclei joining together to form a energetically more favourable nucleus and additional subatomic particles, e.g. neutrons, as by-products. One of the most promising reaction on earth is the fusion of deuterium D (^{2}H) and tritium T (^{3}H) to a helium nucleus (^{4}He) and a neutron (n):

$$\mathrm{D} + \mathrm{T} \rightarrow {}^4\mathrm{He}\,(3.52\,\mathrm{MeV}) + \mathrm{n}\,(14.06\,\mathrm{MeV}), \tag{2.1}$$

which releases 17.58 MeV in total.
Nuclei are charged positively and repel each other which is described by the so-called Coulomb barrier. To overcome this repulsion, reactive nuclei need sufficiently high kinetic energies and hence matter in which fusion occurs is a plasma. [i].
The cross-section of the D-T fusion reaction reaches its maximum at energies between 50 and 80 keV [14] which, in a thermal distribution, corresponds to temperatures in the range of 10 – 20 keV. At these temperatures, matter is in the plasma state, which can be described as a (partially) ionized, quasi-neutral

[i] Note that in plasma physics temperature if mostly given in terms of energy, with $T[\mathrm{eV}] = k_\mathrm{B} \cdot T[\mathrm{K}]$, e.g. $1\,\mathrm{eV} \hat{=} 11605\,\mathrm{K}$, where k_B is the Boltzmann constant

gas, that is governed by long-range electro-magnetic interactions.
To utilize fusion as an energy source, it is necessary to achieve a so called burning plasma at temperatures around 10 – 20 keV, where fusion reactions can sustain the plasma temperature without additional external heating. This does not only require sufficiently high temperatures T but also a high density n and a high energy confinement time τ_E, where τ_E is a measure for the thermal insulation of the plasma and describes how long energy is confined to a given volume. These three quantities define the so called triple product $nT\tau_E$. From an energy balance it can be deducted that the triple product has to fulfil the simplified inequality [15, 16]

$$nT\tau_E > 3 \times 10^{24}\,\mathrm{eVsm^{-3}} \tag{2.2}$$

for a burning plasma. As a measure for this ignition condition the Q-factor is defined as the ratio of power produced by fusion P_{fusion} divided by the external heating power $P_{heating}$

$$Q = \frac{P_{fusion}}{P_{heating}}. \tag{2.3}$$

At $Q = 1$ fusion reactions produce the same amount of energy as is provided by external heating and hence a burning plasma is achieved for $Q \to \infty$. To enable stable fusion conditions and to prevent material damage, it is essential that the plasma does not get in touch with the wall of a fusion experiment or future fusion power plant in an uncontrolled way. A proven method for that is magnetic confinement, where the plasma is trapped by a magnetic field inside a vacuum vessel.
The nowadays most researched configurations are the tokamak and the stellarator. In both approaches, the plasma is confined by a torus shaped magnetic field that is either solely created by external magnetic field coils in the case of a stellarator or by a combination of magnetic field coils and an induced electrical current in the case of a tokamak. In the scope of this thesis, only the tokamak configuration will be explained in more detail in section 2.2. An overview of results and challenges in both configuration can be found in [17].

2.2 The tokamak configuration

Since the 1950s fusion research is being conducted with so called tokamaks, where the magnetic field has a toroidal shape and is generated by a combination of external magnetic field coils and an internally driven current through the plasma which is illustrated in figure 2.1. The toroidal field coils produce a toroidal magnetic field that decays as $1/R$ with the major radius R. The inner side of the magnetic field is therefore often referred to as High Field Side (HFS), while the outer side is labelled Low Field Side (LFS).
This inhomogeneity of the magnetic field leads to charge dependent particle drifts forces (for more details on drifts refer to [15]) which leads to a charge

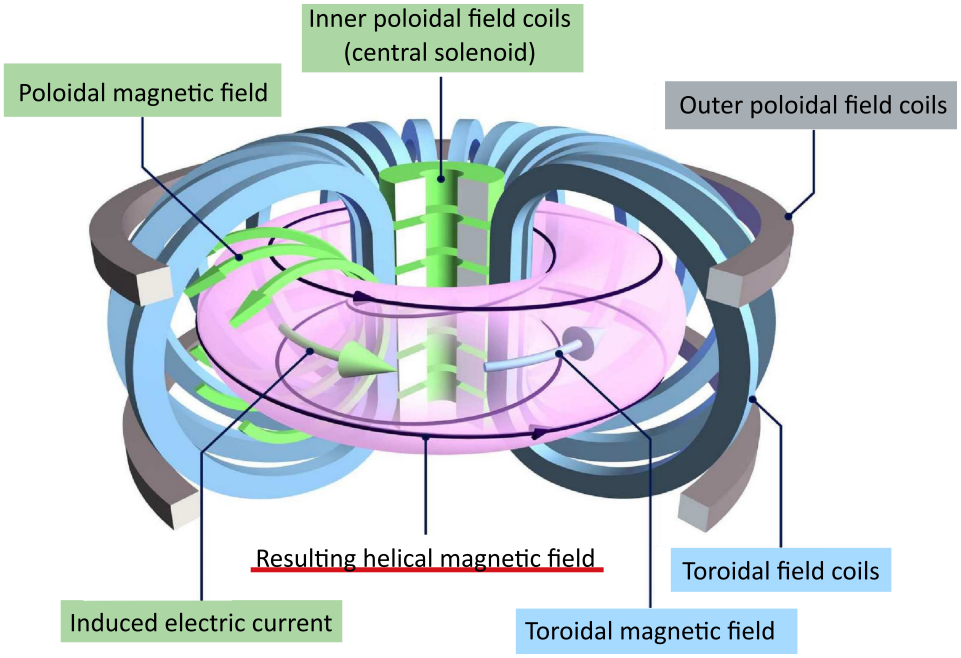

Figure 2.1: Illustration of the magnetic configuration following the tokamak principle. The inner poloidal field coils induce an electric current inside the plasma (green). The toroidal field coils are responsible for the toroidal magnetic field, producing the resulting helical magnetic field. Outer poloidal field coils are used for positioning and shaping of the plasma.

separation. In the standard AUG configuration, ions drift upwards, while electrons will accumulate on the bottom side. This results in an additional vertical electrical field, producing a drift towards the LFS which would lead to poor confinement.
To counteract the charge separation an additional poloidal magnetic field is created by a toroidal current that is induced in the plasma via the solenoid at the center of the torus. This results in helical magnetic field lines that connect the upper and lower side of the torus. Currents, called Pfirsch-Schlüter-Currents, along these field lines reduce the charge separation significantly [15] and improve the confinement. Tokamaks additionally feature outer poloidal field coils that are used to shape and position the plasma inside the vacuum vessel.
If one follows a field line in such a magnetic configuration and observes where it pierces a poloidal plane at a fixed toroidal angle, the points form a Poincaré plot, indicating a so called flux surface. On such a flux surface the product of the magnetic field $\vec{B}$ and the surface normal $\vec{n}$ fulfils

$$\vec{B} \cdot \vec{n} = 0, \tag{2.4}$$

i.e. $\vec{B}$ never traverses the surfaces.
In a tokamak flux surfaces can be divided into two zones: One where helical field lines are closed and another where helical field lines eventually hit a surface. The boundary between both zones, the last closed flux surface, is called separatrix. In the scope of this thesis the zone of closed field lines, where the

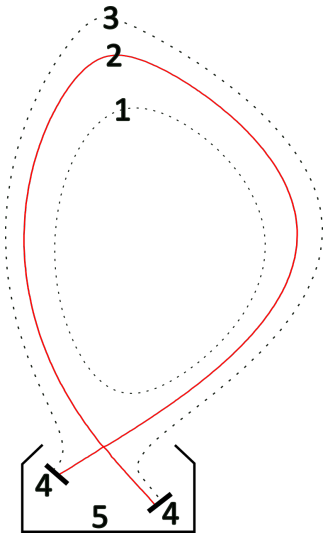

Figure 2.2: Schematics of a poloidal cross section of a magnetic field configuration in divertor configuration which is usually used in a tokamak. 1 is a flux surface in the confined region, 2 indicates the separatrix and 3 is a flux surface in the scrape off layer. 4 are target plates and the area labeled with 5 is called divertor.

plasma is confined, is referred to as core whereas the zone of open field lines is called scrape-off layer (SOL). A common way of describing the radial position associated to a flux surface is the normalized plasma radius ρ which is defined as $\rho = 0$ at the magnetic axis and $\rho = 1$ at the separatrix.
Figure 2.2 shows a schematic of these zones with exemplary flux surfaces. Surface 1 is in the core, surface 3 in the SOL and surface 2 indicates the separatrix. Additionally, so called target plates are indicated (4). Preferentially these target plates are located far away from the confined area to separate the interaction of plasma particles with solid surfaces from the confined plasma. Such an arrangement, as displayed by 5 in figure 2.2, is called divertor and is used to shield the confined plasma from impurity ions that arise from plasma interaction with the target plates. In a divertor configuration one can identify a third zone, which is located below the X-point of the separatrix and between the target plates. This zone is called private flux region.
With the tokamak concept it was possible to reach a fusion gain factor of $Q = 0.67$ in 1997 at the Joint European Torus (JET) in Culham utilizing the D-T fusion reaction, meaning that 67 % of the input heating power could be produced by D-T fusion reactions. Future fusion power plants aim at a Q factor of 10 or higher [18] to effectively generate electricity from fusion and to achieve ignition, where the plasma heating is self-sustained by heating through the generated alpha particles from D-T fusion.
Since 1997 research efforts worldwide focused on key issues missing to bridge the gap between research reactors and pilot power plants. These efforts include [19]:

- mitigating plasma disruption

- improving plasma stability
- deepening the understanding of plasma-wall interaction
- tritium operation

The majority of above mentioned research efforts aim at preparing the physical and operational conditions of the international fusion research reactor ITER, with the goal to demonstrate the scientific and technological feasibility of fusion energy for electricity generation by achieving a gain factor of $Q \geq 10$.
The research presented in this thesis can be attributed to the third point in the list, deepening the understanding of plasma-wall interactions.

2.3 Theoretical Description of Plasmas

The work presented in this thesis focuses on the modeling of parameters of dedicated plasma discharges and the transport processes in these discharges. This chapter introduces the underlying theoretical models.

2.3.1 The Fluid Model

Describing a fusion plasma on microscopic scale requires the computation of the interaction of about 10^{20} particles per cubic metre. Assuming that fields and forces act on a macroscopic scale, i.e. acting on volumes containing many particles, one can make use of a particle distribution function $f_a(\vec{x}, \vec{v}, t)$ for particle species a at location $\vec{x}$ with velocity $\vec{v}$ at time t.
Then

$$\frac{\partial f_a}{\partial t} + \vec{v}\frac{\partial f_a}{\partial \vec{x}} + \frac{\vec{F}_a}{m_a}\frac{\partial f_a}{\partial \vec{v}} = \left(\frac{\partial f_a}{\partial t}\right)_{coll} \tag{2.5}$$

is the kinetic equation [20], where $\vec{F}_a$ is the force acting on the particles, m_a is the particles mass and $\left(\frac{\partial f_a}{\partial t}\right)_{coll}$ describes the influence of collisions. Particles in a fusion plasma are subject to electro-magnetic forces and with the electric field $\vec{E}(\vec{x}, t)$ and the magnetic field $\vec{B}(\vec{x}, t)$ the force term reads

$$\vec{F}_a(\vec{x}, \vec{v}, t) = q_a\left[\vec{E}(\vec{x}, t) + \vec{v} \times \vec{B}(\vec{x}, t)\right] \tag{2.6}$$

for a particle with charge q_a, when gravitational forces are omitted. If f_a is close to a Maxwellian distribution one can calculate so-called moments of f_a as measures in velocity space. The k-th moment is given by

$$\int \vec{v}^k f_a d\vec{v} = n_a \left\langle \vec{v}^k \right\rangle . \tag{2.7}$$

Hence the zeroth moment results in the number density

$$n_a(\vec{x},t) = \int f_a(\vec{x},\vec{v},t)\, d\vec{v} \tag{2.8}$$

and the first moment is related to the average fluid velocity $\vec{u}_a$ as

$$n_a\vec{u}_a(\vec{x},t) = \int \vec{v} f_a(\vec{x},\vec{v},t)\, d\vec{v}. \tag{2.9}$$

To obtain more information about the system it is advantageous to formulate the particle velocity as $\vec{v} = \vec{u}_a + \vec{v}_{\text{therm}}$ with the thermal velocity $\vec{v}_{\text{therm}}$. Then the second moment relates to the temperature T_a and the pressure p_a as

$$\frac{3}{2} n_a T_a = \frac{3}{2} p_a = \frac{1}{2} m_a \int \vec{v}_{\text{therm}} \vec{v}_{\text{therm}}^{\intercal} f_a d\vec{v}. \tag{2.10}$$

Note, that here $\vec{v}_{\text{therm}}\vec{v}_{\text{therm}}^{\intercal}$ is a tensor and the above equation holds true only, if the tensor has no non-diagonals entries. More generally the second moment defines the pressure tensor

$$\overleftrightarrow{P}_a = m_a \int \vec{v}_{\text{therm}} \vec{v}_{\text{therm}}^{\intercal} f_a d\vec{v} = p_a \overleftrightarrow{1} + \overleftrightarrow{\Pi}_a, \tag{2.11}$$

with the unity tensor $\overleftrightarrow{1}$ and the anisotropic part $\overleftrightarrow{\Pi}_a$.
Using these identities the kinetic equation 2.5 can be integrated over velocity space yielding the continuity equation for species a which describes the **particle balance**

$$\frac{\partial n_a}{\partial t} + \frac{\partial (n_a \vec{u}_a)}{\partial \vec{x}} = S(\vec{x},t), \tag{2.12}$$

where $S(\vec{x},t) = \int \left(\frac{\partial f_a}{\partial t}\right)_{coll} d\vec{v}$ is a source term arising from e.g. ionization processes.
Taking the first moment of the kinetic equation, yields the **momentum balance** or sometimes also called force balance

$$m_a \frac{\partial n_a \vec{u}_a}{\partial t} + \frac{\partial}{\partial \vec{x}} \cdot \left(m_a n_a \vec{u}_a \vec{u}_a^{\intercal} + \overleftrightarrow{P}_a \right) - q_a n_a \left(\vec{E} + \vec{u}_a \times \vec{B} \right) = \vec{R}_{ab} + \vec{S}_{m,neut,a}. \tag{2.13}$$

The right hand side terms arise from the first moment of the collisional term in equation 2.5, i.e. $\int m_a \vec{v} \left(\frac{\partial f_a}{\partial t}\right)_{coll} d\vec{v} = \vec{R}_{ab} + \vec{S}_{m,neut,a}$.
Here, $\vec{R}_{ab}$ is the momentum change due to collisions of particle species a and b, i.e. friction between a and b, while $\vec{S}_{m,neut,a}$ is a momentum source from collision of species a with neutral particles, e.g. from charge exchange.
To get the **energy balance** the second moment of equation 2.5 is taken to obtain [21]

$$\begin{aligned}&\frac{\partial}{\partial t}\left(\frac{m_a n_a}{2}u_a^2+\frac{3}{2}n_a T_a\right)+\frac{\partial}{\partial \vec{x}}\cdot\left(\frac{5}{2}n_a m_a T_a \vec{u}_a+\vec{q}_a\right)\\&+\frac{\partial}{\partial \vec{x}}\cdot\left(\frac{1}{2}n_a m_a u_a^2 \vec{u}_a+\vec{u}_a\cdot\overleftrightarrow{\Pi}_a\right)-q_a n_a u_a \vec{E}\\&=Q_{ab}+\vec{u}_a\vec{R}_{ab}+S_{e,neut,a}.\end{aligned} \tag{2.14}$$

Here, Q_{ab} is the heat transferred from species a to species b via collisions and $S_{e,neut,a}$ is the energy source from collisions with neutral particles. Both terms arise from $\int \frac{m_a}{2} m_a \vec{v}\vec{v}^{\intercal}\left(\frac{\partial f_a}{\partial t}\right)_{coll} d\vec{v}$. On the left hand side $\vec{q}_a$ is the heat flux density of species a.
The set of equations 2.12, 2.13 and 2.14, also called Braginskii equations, is not closed as both the anisotropic part of the pressure tensor $\overleftrightarrow{\Pi}_a$ as well as the heat flux density $\vec{q}_a$ consist of higher moments of f_a. To close the equations both $\overleftrightarrow{\Pi}_a$ and $\vec{q}_a$ are usually expressed via a diffusive ansatz or a polynomial of higher moments of n_a, $\vec{u_a}$ and T_a [22, 23].

2.3.2 Impurity Transport

Apart from the plasmas hydrogenic species additional particles that are not involved in the fusion process will always be present. These are called impurities. In a pure D-T plasma fusion reaction will produce helium ash. The He ash can dilute the plasma fuel, but does not radiate strongly. Another source of impurities is from plasma-wall interactions (see section 2.4), where neutral atoms are released from plasma facing components via sputtering. The majority of these particles enter the plasma and ionize. While most ionized impurities directly return to the surface (also called prompt re-deposition) some are transported in the SOL and might even reach the confined plasma. Typically the transport of impurities is divided into transport parallel to $\vec{B}$ and perpendicular to $\vec{B}$. The perpendicular flux density $\Gamma_\perp$ of species with density n is given by

$$\Gamma_\perp = -D_\perp \frac{\mathrm{d}n}{\mathrm{d}r} - v_{\text{pinch}} n, \tag{2.15}$$

with a cross-field transport coefficient $D_\perp$ and an inward convection velocity v_{pinch}. Both $D_\perp$ and v_{pinch} are not calculable from first principles, but are adapted to match experimental measurements.
To get an estimate for the flux density parallel to $\vec{B}$ the force acting on an impurity ion with charge Z and mass m_Z is assumed to follow ([24] p. 298)

$$\begin{aligned}F_Z &= F_{\nabla p} &&+F_F &&+F_E &&+F_{\nabla T_e} &&+F_{\nabla T_i}\\&= -\frac{1}{n_Z}\frac{\mathrm{d}p_Z}{\mathrm{d}s} &&+m_Z\frac{\left(v_{\parallel,i}-v_{\parallel,Z}\right)}{\tau_s} &&+ZeE_\parallel &&+\alpha_e\frac{\mathrm{d}T_e}{\mathrm{d}s} &&+\beta_i\frac{\mathrm{d}T_i}{\mathrm{d}s}\end{aligned} \tag{2.16}$$

with s being the distance in parallel direction, pointing upstream away from the target.

- $F_{\nabla p}$ is the impurity pressure gradient force.
- F_F is the friction force arising from the difference of main ion velocity $v_{\parallel,i}$ and impurity velocity $v_{\parallel,Z}$. τ_s is the parallel collisional diffusion time derived following Spitzer [25].
- F_E is the electrostatic force arising from the parallel electric field.
- $F_{\nabla T_e}$ is the electron temperature gradient force with $\alpha_e \propto Z^2$.
- $F_{\nabla T_i}$ is the ion temperature gradient force with $\beta_i \propto Z^2$.

The pressure gradient force in equation 2.16 can be interpreted as parallel velocity diffusion. To get a diffusion equation similar to equation 2.15 in parallel direction some simplifications have to be made.
If the impurities are thermalised everywhere ($T_Z = T_i = \text{const.}$), there are no temperature gradients and the only forces are the pressure gradient force and the friction force.
With a stagnant background ($v_i = 0$) and high collisionality, such that ion inertia can be neglected, the forces on impurity ions are in balance, $F_Z = 0$, and equation 2.16 can be rearranged to read ([24] p. 301)

$$\Gamma_\parallel = -D_\parallel \frac{\mathrm{d}n_Z}{\mathrm{d}s}, \tag{2.17}$$

with the parallel diffusion coefficient

$$D_\parallel = \tau_s v_{th}^2, \qquad \text{where} \qquad v_{th} = \sqrt{\frac{T_Z}{m_Z}} \tag{2.18}$$

is the thermal velocity of the impurity ions. Thus in its most simple form, the motion of impurity ions in a fixed plasma background is the diffusion along impurity density gradients.

2.3.3 Impurity Migration

The cycle of impurities that are eroded from a wall tile, transported through the plasma and eventually re-deposited on a surface, where they can potentially also be re-eroded, is called impurity migration.
This process leads to the formation of mixed material layers with potentially unfavourable properties such as the incorporation of radioactive tritium. Additionally, the intrinsic source of impurities eroded from plasma facing components can lead to unwanted dilution of the hydrogenic fuel in the confined plasma and to unwanted radiation losses.

Understanding impurity migration and thus the dynamic evolution of material layers is therefore required to understand the intrinsic sources of impurities. To self-consistently calculate impurity fluxes and the evolution of the wall the code WallDYN [26] has been developed, which is introduced in section 4.3.

2.4 Plasma-Wall Interaction

Particles in the SOL will eventually interact with plasma facing components, where they are either implanted, back-scattered as neutral atoms or released as molecules after recombination. Surfaces are therefore sinks for a plasma [24] and emit a flux of neutral atoms and molecules back into the plasma.
The cycle of particle impact, re-emission, ionisation and impact again is called re-cycling and the number of incident particles that are lost to the surface is generally almost equal to the number of particles that are re-emitted back into the plasma, i.e. the recycling coefficient is close to 1.
For particle species where the number of re-emitted particles from the wall is lower than the number of incident particles from the plasma the term partial re-cycling species is often used.

2.4.1 Plasma sheath

A plasma is defined by quasi-neutrality, i.e. the electron density equals the ion density ($n_e \approx n_i$). However, plasma parameters adjacent to a conducting wall are dominated by a region of net charge with $n_e < n_i$, the sheath. It develops due to different particle flux densities Γ of ions and electrons, if the effect of the electric field in the sheath is neglected. The flux density of a particle species with density n is proportional to the thermal velocity $v_{th} = \sqrt{2T/m}$, where T is the particle temperature and m is the mass, like

$$\Gamma_n \propto v_{th} n. \tag{2.19}$$

Hence, the flux density is proportional to $m^{-1/2}$ and is significantly larger for electrons than for ions. This leads to the sheath region with $n_e < n_i$ and a negative potential build-up at the surface. The resulting electric field is screened on the scale of the Debye length

$$\lambda_D = \sqrt{\frac{\epsilon_0 T_e}{n_e e^2}} \tag{2.20}$$

with ϵ_0 being the permittivity of free space and e the elementary charge.
Ions in the electrostatic sheath are accelerated towards the surface by the electric field and the average impact energy follows (chapter 2.9 in [24])

$$\bar{E}_{\text{impact}} = 2T_i + 3ZT_e, \tag{2.21}$$

where Z denotes the charge state of the ion. The $3ZT_e$ result from the acceleration due to the electric field in the sheath and the $2T_i$ follow from the ion speed at the sheath edge, which is equals to the ion thermal velocity, according to the Bohm criterion [24]. Since the impact energy goes with the charge state and the electron temperature, plasma impurities can have a significantly higher impact energy than main plasma ions. This results in much higher sputter yields for impurities (compare to formula 2.39) than for main plasma ions.

2.4.2 Particle collisions in solid matter

Fast particles (beyond thermal energies) are implanted into the surface material where they further interact with atoms in the lattice structure and eventually are deposited after loosing all kinetic energy via elastic collisions with other atoms and in-elastic interaction with target electrons.
The movement of particles that penetrate into the material can be approximated by a series of independent, binary collisions, as long as the free mean path is larger than D, the distance between the points of intersections (x_1 and x_2) of asymptotes, in figure 2.3. Figure 2.3 shows the scattering geometry for binary collisions, where p is the so-called impact parameter. This binary collision approximation is utilized in codes that calculate sputter and reflection yields of particles fluxes on material surfaces, such as SDTrimSP (see section 4.2).

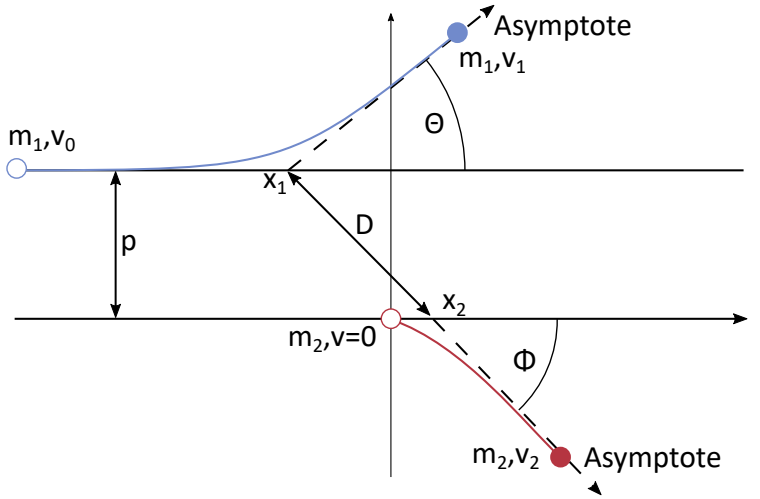

Figure 2.3: Scattering geometry with asymptotes for binary collisions.

If an incoming particle, the projectile, with mass m_1 and energy E_0 (velocity v_0) scatters at a target atom in the target, the projectile will change its trajectory by Θ and will continue on its path with energy E_1 (velocity v_1). The target with mass m_2 will obtain energy E_2 (velocity v_2) and will be deflected by angle Φ as a result. If the collision is not purely elastic, an inelastic energy loss Q occurs.

From energy and momentum conservation the angles Θ and Φ or the energies after the collision E_2 and E_3 can be calculated. Solving for the angles results in [27]

$$\cos\Theta = \frac{1}{2}\sqrt{\frac{E_1}{E_0}}\left(1+\frac{m_2}{m_1}\right) + \frac{1}{2}\sqrt{\frac{E_0}{E_1}}\left[1-\frac{m_2}{m_1}\left(1-\frac{Q}{E_0}\right)\right] \tag{2.22}$$

$$\cos\Phi = \frac{1}{2}\sqrt{\frac{E_2}{E_0}}\left(\frac{1+\frac{m_2}{m_1}}{\sqrt{\frac{m_2}{m_1}}}\right) + \frac{1}{2}\sqrt{\frac{E_0}{E_2}}\frac{1}{\sqrt{\frac{m_2}{m_1}}}\frac{Q}{E_0} \tag{2.23}$$

and the energy transfer reads

$$\frac{E_1}{E_0} = \frac{m_1 m_2}{(m_1+m_2)^2}\left(\cos\Theta \pm \sqrt{\left(\frac{m_2}{m_1}\right)^2\left(1-\frac{1+\frac{m_2}{m_1}}{\frac{m_2}{m_1}}\frac{Q}{E_0}\right)^2 - \sin^2\Theta}\right)^2 \tag{2.24}$$

$$\frac{E_2}{E_0} = \frac{m_1 m_2}{(m_1+m_2)^2}\left(\cos\Phi \pm \sqrt{\left(1-\frac{1+\frac{m_2}{m_1}}{\frac{m_2}{m_1}}\frac{Q}{E_0}\right)^2 - \sin^2\Phi}\right)^2 . \tag{2.25}$$

Note that the energy transferred from the projectile to the target in equation 2.25 is maximized for purely elastic scattering ($Q = 0$) and heads-on collisions ($\Phi = 0$), resulting in

$$\left.\frac{E_2}{E_0}\right|_{max} = 4\frac{m_1 m_2}{(m_1+m_2)^2}, \tag{2.26}$$

which is maximized for $m_1 = m_2$.

Typically the set of equations is solved by calculating the scattering angle with a centre-of-mass ansatz, where the binary collision is reduced to the interaction of a single quasi particle with the interaction potential $V(r)$. The quasi particle then has a reduced mass of

$$\mu = \frac{m_1 m_2}{m_1+m_2} \tag{2.27}$$

and the kinetic energy

$$E_r = \frac{\mu}{2}v_0^2. \tag{2.28}$$

The scattering angle in the centre-of-mass system is then given by [27]

$$\bar{\theta} = \pi - 2p \int_R^\infty \frac{1}{r^2 g(r)} dr \tag{2.29}$$

$$\text{with} \qquad g(r) = \sqrt{1 - \frac{V(r)}{E_r} - \frac{p^2}{r^2}} \tag{2.30}$$

with R being the distance of closest approach, also called apsis, and r the distance between scattering centre and the projectile.
The angles Θ and Φ in the binary ansatz can then be computed via

$$\tan\Theta = \frac{\frac{m_2}{m_1} f \sin\bar{\theta}}{1 + \frac{m_2}{m_1} f \cos\bar{\theta}} \tag{2.31}$$

$$\tan\Phi = \frac{\sin\bar{\theta}}{1 - f\cos\bar{\theta}} \tag{2.32}$$

$$\text{with} \qquad f = \sqrt{1 - \frac{1 + \frac{m_2}{m_1}}{\frac{m_2}{m_1}} \frac{Q}{E_0}}.$$

The interaction potential is generally given by the interaction of nuclei that are shielded by their electron clouds and can be described by a radial symmetric Coulomb potential

$$V(r) = \frac{1}{4\pi\epsilon_0} \frac{Z_1 Z_2 e^2}{r} \cdot U\left(\frac{r}{a}\right), \tag{2.33}$$

with Z_1 and Z_2 being the atomic numbers of projectile and target, e the electron charge, r the radius measured between the atoms, ϵ_0 the electric constant, $U\left(\frac{r}{a}\right)$ the screening function and a the screening length given by

$$a = \left(\frac{9\pi^2}{128}\right)^{\frac{1}{3}} a_B \left((Z_1^x + Z_2^x)^y\right)^{-\frac{1}{3}}, \tag{2.34}$$

with a_B being the Bohr radius. The screening function is generally given by

$$U\left(\frac{r}{a}\right) = \sum_{i=1}^{n} c_i \exp\left(-d_i \frac{r}{a}\right), \tag{2.35}$$

where $\sum_{i=1}^{n} c_i = U(0) = 1$. The sets of parameters x, y, c_i and d_i are adapted for the interacting species.

The probability $d\omega$ that a projectile is scattered by an angle segment $d\Theta$ when hitting a target with surface number density δ is given by the cross section $d\sigma$. It is the area a projectile has to hit to be scattered by $d\Theta$. This probability is given by

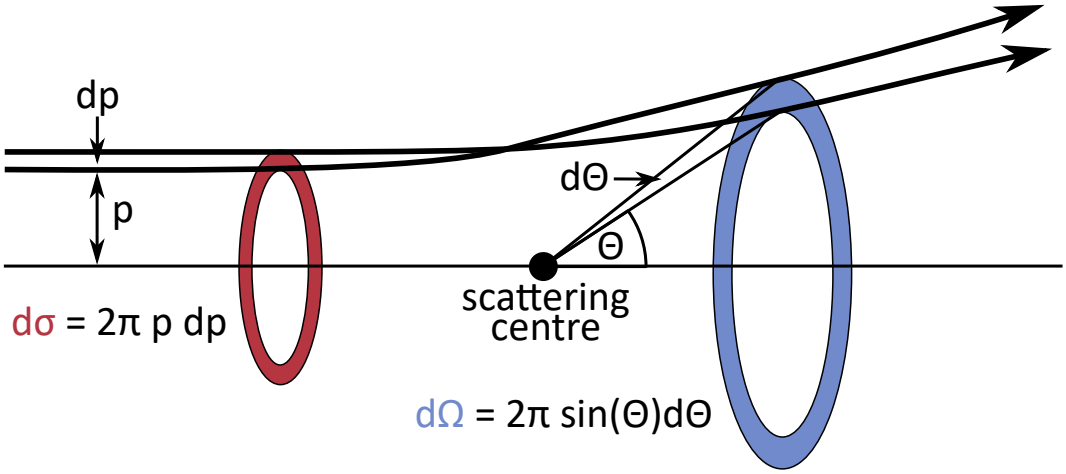

Figure 2.4: Illustration of the differential cross section for scattering.

$$d\omega = \delta d\sigma = \delta 2\pi p dp. \tag{2.36}$$

For diagnostical purposes (e.g. Nuclear-Reaction-Analysis, see section 2.5) it is often of interest to know the probability of scattering into a solid angle segment $d\Omega$. This can be expressed by the differential cross section $\frac{d\sigma}{d\Omega}$ via

$$\frac{d\sigma}{d\Omega} = \frac{p}{\sin\Theta}\frac{dp}{d\Theta}. \tag{2.37}$$

In figure 2.4 particle trajectories for scattering at angles Θ and $\Theta + d\Theta$ are illustrated with the resulting cross section $d\sigma$, that can be calculated with the impact parameter p, and the solid angle segment $d\Omega$, as given by equation 2.37.

2.4.3 Sputtering

If ions or neutrals hit a solid surface with sufficient energy, momentum can be transferred to atoms in the lattice such that a threshold energy E_{th} is exceeded and the target atom is emitted from the surface. This is called physical sputtering and results in the injection of impurities from plasma facing components into the plasma. If these impurities are ionized and transported through the plasma they eventually hit another surface with high energies, resulting in so called self-sputtering, where surface material is eroded by projectiles of the same mass, which transfers momentum much more efficiently (see equation 2.26).

Sputtering processes are usually characterized by the sputter yield

$$Y = \frac{N_{sputter}}{N_{proj}}, \tag{2.38}$$

which is the ratio of sputtered particles $N_{sputter}$ by the number of incoming projectiles N_{proj}.
In general, the number of sputtered particles and hence the sputter yield depends on a variety of parameters like the angle of incidence α, the threshold energy E_{th}, the surface binding energy U_s, the masses of projectile and surface atoms m_1 and m_2 and the nuclear stopping cross section $S_n(E)$, that depends on the energy of the projectile E. For normal incidence ($\alpha = 0\,^\circ$) the sputter yields follows the revised Bohdansky formula [28]

$$Y \propto S_n(E) \left(1 - \left(\frac{E_{th}}{E}\right)^{2/3}\right) \left(1 - \frac{E_{th}}{E}\right)^2, \tag{2.39}$$

where E_{th} depends on m_1, m_2 and U_s. The dependence on the angle of incidence α is investigated in [29, 30].
Surfaces often consist of mixtures of different elements and the partial sputter yield Y_i of an element i depends on its surface concentration η_i. As surface elements usually have different partial sputter yields, the less sputtered element will be enriched at the surface. The ratio of partial sputter yield, Y_A and Y_B with surface concentration, η_A and η_B is, in equilibrium, given by

$$\frac{Y_A}{Y_B} = r\frac{\eta_A}{\eta_B}, \tag{2.40}$$

with the preferential sputtering parameter r. As a rule of thumb the heavier surface element is sputtered less and will be dominant in mixed layers.

2.4.4 Reflection

Particles hitting a surface are either deposited after transferring their energy to surrounding particles or they can be reflected. Reflection, also called backscattering, is characterized by the reflection yield which, similar to the sputter yield in equation 2.38, is defined by,

$$R = \frac{N_{refl}}{N_{proj}} \tag{2.41}$$

with the number of incoming projectiles N_{proj} and the number of reflected particles N_{refl}.

2.4.5 Deposition

If the influx Γ_{in} of a particle species to a surface is larger than the sum of reflected particles Γ_{refl}, self sputtered particles $\Gamma_{sput,self}$ and particles sputtered by other projectiles $\Gamma_{sput,other}$

$$\Gamma_{in} > \Gamma_{refl} + \Gamma_{sput,self} + \Gamma_{sput,other} = \Gamma_{Gross}, \tag{2.42}$$

a layer of projectile particles is deposited at the surface. The right hand side of the equation is called the gross erosion flux Γ_{Gross}.
Volatile species like nitrogen form mixed layers of finite thickness with the wall material, while layers of non-volatile species grow continuously (e.g. beryllium layers). Implanted species may also diffuse further into the material where they can be retained.

2.5 Nuclear Reaction Analysis

To determine the surface composition of plasma facing components after experiments, a common technique is ion beam analysis, where a sample is irradiated with energetic ions to either analyse scattered particles or by-products of nuclear reactions at the surface. At IPP, ion beam analysis is conducted with a 3 MV tandem accelerator featuring a variety of ion beams including ^{1}H, D, ^{3}He and ^{4}He [31]. Nuclear reaction analysis (NRA) is a technique where a sample is irradiated with nuclei and the energetic spectra of products from nuclear reactions, are measured. The reaction utilised in this thesis to analyse the content of ^{15}N in a sample by irradiating it with 1 MeV protons is

$$^{15}\mathrm{N} + {}^{1}\mathrm{H} \rightarrow {}^{12}\mathrm{C} + {}^{4}\mathrm{He}, \tag{2.43}$$

which in short is written as ^{15}N(^{1}H, ^{4}He)^{12}C. The number of resulting α particles is counted at a reaction angle of 135° with a detector having a solid angle of $\Delta\Omega = 22$ msr.
Using the differential cross section for this reaction from [32] the counts are converted to a ^{15}N surface number density following [33]

$$\sigma_{^{15}\mathrm{N}} = \frac{N_\alpha}{\frac{d\sigma}{d\Omega}\big|_{135°,1\,\mathrm{MeV}}\,\Delta\Omega Q}, \tag{2.44}$$

where Q is the number of projectiles that hit the target, N_α is the total amount of α particles detected and $\Delta\Omega = 22$ msr is the solid angle of the detector.

Figure 2.5 shows energy spectra obtained by NRA from a sample exposed in AUG with the MEM. The spectra were measured at different locations on the sample. The detector was calibrated such that channels 30 to 80 correspond to the expected energy of measured α particles.
To substract the background an additive fit function was applied to the data following

$$p = A + \frac{B}{x} + Ce^{\frac{-(x-x_0)^2}{2\sigma^2}}, \tag{2.45}$$

where x refers to the channel number and the fitting parameters A, B, C, x_0 and σ were optimised with `curve_fit` from `scipy.optimize` [34]. This allows

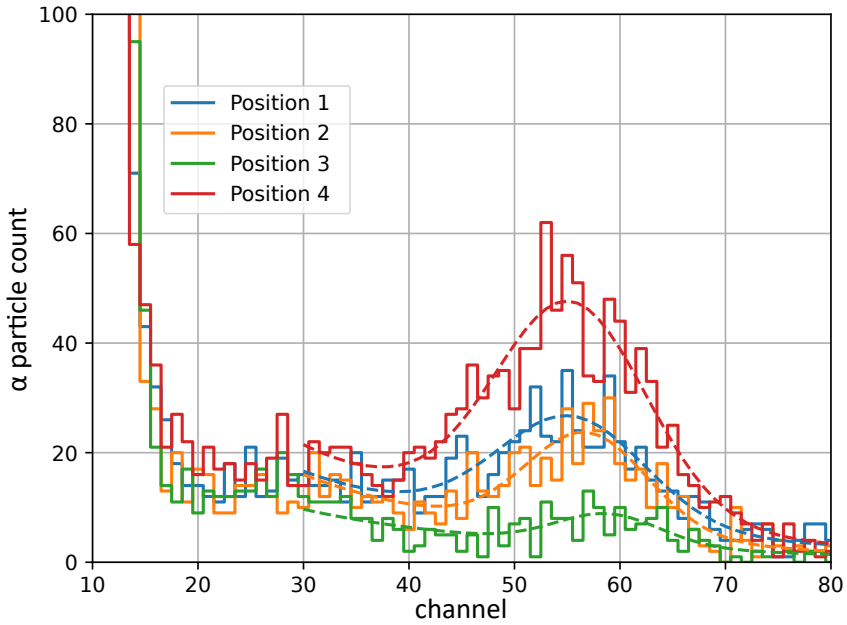

Figure 2.5: Calculated spectra obtained from NRA at different locations on a sample. The dashed lines are fitted with equation 2.45.

for a direct integration of the Gaussian part for background free proton counts. The linear and Gaussian contributions obtained from fitting are plotted in figure 2.6.
An error was estimated by counting the raw signal counts including the background and subtracting the counts from integrating the linear part of equation 2.45 resulting in differences of less than 5 % when compared to the integration of the Gaussian part only.

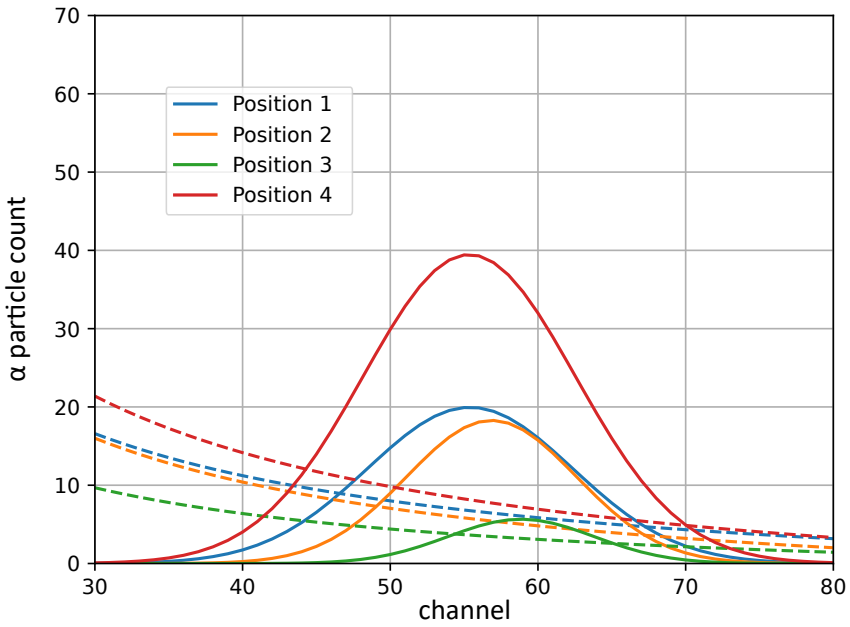

Figure 2.6: Linear and Gaussian contribution to fitted spectra in figure 2.5.

Chapter 3

Experimental investigations

This chapter introduces the concept of analysed and conducted experiments in the course of this thesis. In section 3.2 an introduction is given to ASDEX Upgrade, the fusion experiment where plasma discharges for this thesis were carried out, and some of its diagnostical and heating systems are explained briefly. In the last part of this chapter, experimental results from analysed and conducted experiments are given in section 3.5.

3.1 Experimental concept

The experimental part of this thesis is inspired by previous work in [12], where the ^{15}N migration in ASDEX Upgrade was experimentally investigated by analysing the amount of deposited ^{15}N on probes in the divertor and at the outer mid-plane after exposure to a nitrogen-seeded deuterium plasma. The advantage of ^{15}N over ^{14}N is the small abundance of only 0.37 % in atmospheric N_2, allowing for background free determination of N deposition from impurity migration processes. The interpretation of deposition results requires the use of simulations that depend on constant plasma parameters and are ideally compared to experimental results at more than one location.
Therefore, discharges conducted in the course of this thesis were designed to be in low-confinement L-mode and have stable plasma parameters over the duration of the discharge. In contrast to the setup in [12] the poloidal position of the ^{15}N seeding valve was changed from the divertor to the top of the chamber to investigate whether the poloidal position has an effect on the deposited ^{15}N. Deposition probes were installed in the divertor manipulator system and at the outer mid-plane with the mid-plane manipulator system (see subsection in section 3.3) to measure ^{15}N deposition at two positions simultaneously and enable a comparison of simulated and experimental results (see section 5). In [12] the deposition probe at the mid-plane was used without a cap. To obtain discharge resolved deposition profiles at the mid-plane, the probe was covered by a cap with a small slit during discharges conducted for this thesis. The probe below the slot was rotated between discharges.

The toroidal and poloidal position of the installed probes can be seen in the experimental results (section 3.5) in figures 3.6 and 3.7, respectively.

3.2 ASDEX Upgrade

The **A**xial **S**ymmetric **D**ivertor **EX**periment (ASDEX) Upgrade is a tokamak located at the Max Planck Institute for Plasma Physics (IPP) in Garching, Germany. An overview of some technicals details of ASDEX Upgrade and typical plasma parameters are listed in table 3.1.

Table 3.1: Some technical details and typical plasma parameters in ASDEX Upgrade

Magnetic field strength	up to 3.1 T
Plasma current	0.4 – 1.6 MA
Heating power	up to 27 MW
Pulse duration	< 10 s
Data per pulse	about 40 GB
Major radius	1.65 m
Horizontal plasma radius	0.5 m
Vertical plasma radius	0.8 m
Plasma volume	14 m^3
Electron density	1e20 m^{-3}
Plasma temperature	60 – 100 million degree

A photo from inside the vacuum chamber can be seen in figure 3.1, where the tungsten coated plasma facing components in the divertor structure and those covering the central solenoid are visible.
The coating allows investigations of the effect of heavy impurities on plasma performance and the feasibility of tungsten as a first wall material to withstand high heat loads during plasma operation. It was shown that tungsten fulfils two important conditions: the erosion was moderate and the tungsten concentrations in the plasma core could be controlled via central heating of the plasma [35, 36].
ASDEX Upgrade is also known to easily access the so called H-mode (high confinement mode), which was discovered in its predecessor machine ASDEX in 1984 [37] and is foreseen to be used in ITER to achieve the desired performance. In H-mode the energy is typically confined 2 times longer than in low confinement mode (L-mode) [38] which can be related to a transport barrier in the plasma edge.
The divertor structure in ASDEX Upgrade is optimized for plasma discharges in a so-called lower single null configuration, where the last closed flux surface has a single X-point above the lower divertor structure. A schematic of a poloidal cut of ASDEX Upgrade is depicted in figure 3.2, where an exemplary magnetic field configuration in lower single null configuration is indicated by

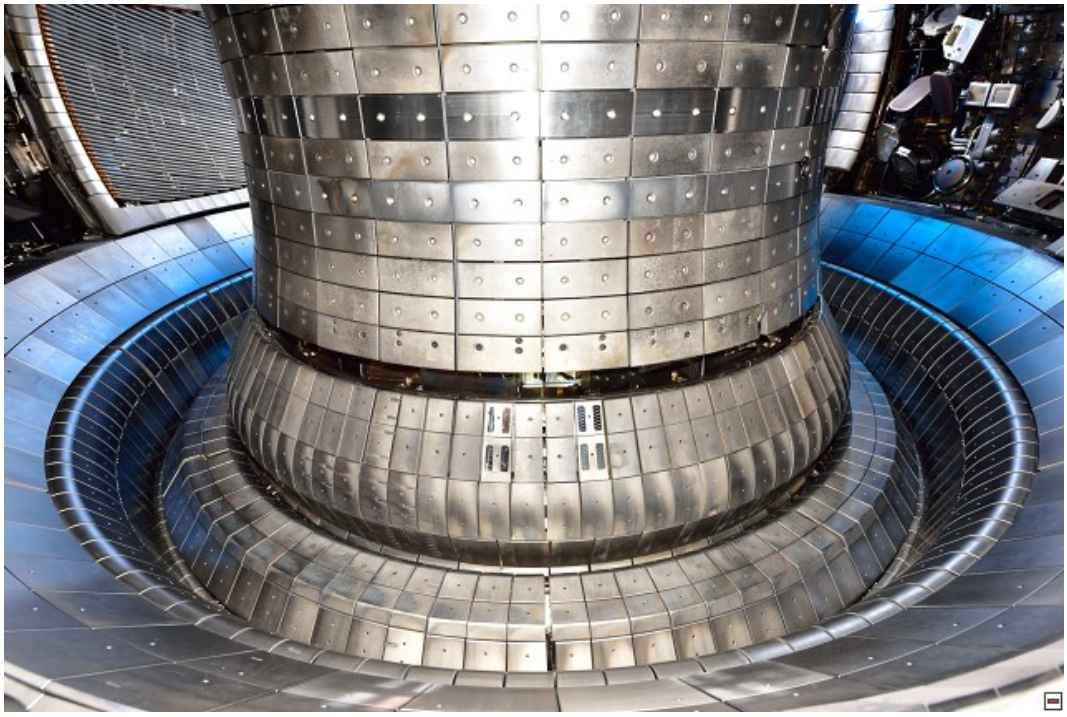

Figure 3.1: A view inside the plasma chamber of ASDEX Upgrade. One can the plasma facing components covering the central solenoid and the divertor structure. The grid structure on the left hand side is an antenna of the ion cyclotron resonance heating system.

the dotted red lines with the solid line representing the separatrix. The green dotted lines represent the open field lines in the Scrape-Off-Layer (SOL).
The black surfaces indicate plasma facing components (PFCs) while the gray structure is a poloidal limiter. The yellow areas show poloidal field coils and the surrounding blue lines display the vessel structure with its many ports for gas fueling, diagnostical systems and heating.

3.3 Diagnostics

ASDEX Upgrade features about 70 diagnostics to measure plasma parameters, magnetic fields, surface temperatures of in-vessel components and occurring forces [39]. The following subsections will briefly introduce diagnostics and tools that are relevant for this thesis.

3.3.1 Magnetic Equilibrium Reconstruction

In section 2.1 the concept of flux surfaces has been introduced briefly. To relate experimentally obtained data to their position within the magnetic configuration it is crucial to reconstruct the flux surfaces from the magnetic probe array in ASDEX Upgrade by solving the Grad-Shafranov equation (GSE) numerically [2].

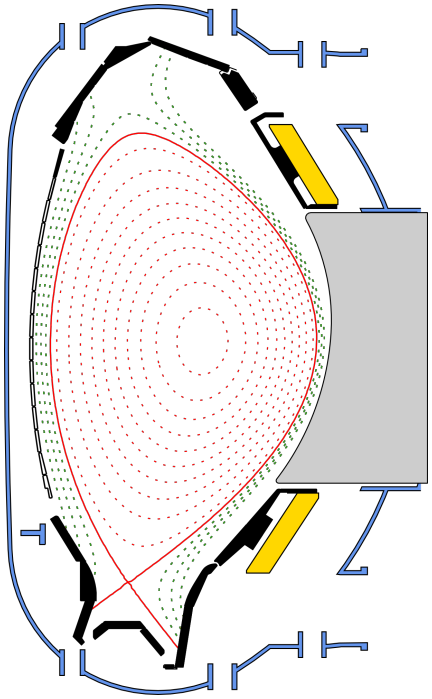

Figure 3.2: Cut in the poloidal plane of ASDEX Upgrade. The blue lines indicate the vessel structure with gaps for pumping ducts and diagnostics. In yellow two poloidal field coils are visible while the black structures are plasma facing components (PFCs). On the low field side the poloidal cut of a limiter can be seen in gray. The dotted red lines are an exemplary poincaré plot of the closed magnetic field lines and the solid red line indicates the separatrix. The green dotted line represent the open field lines of the Scrape-Off-Layer.

The GSE describes the magnetohydrodynamical equilibrium by relating the poloidal magnetic flux to the current distribution in the plasma. At ASDEX Upgrade a commonly used solver is the CLISTE [40] equilibrium code where both magnetic flux and current distribution are parametrised. The free parameters of the parametrisation are varied such that the predicted measurements in an assumed magnetic topology agree with experimental measurements. The reconstructed magnetic field is used in this thesis to generate grids for simulations and determines the radial position of the separatrix, which is used to determine the radial position of other diagnostics.

3.3.2 Thomson Scattering Diagnostic

The Thomson scattering diagnostic is based on the scattering of monochromatic light, emitted from a laser, by electrons in the plasma. By analysing the scattered light one can simultaneously measure electron temperature T_e and electron density n_e in the plasma, because the scattered power spectrum is directly proportional to the electron velocity distribution [41].
ASDEX Upgrade features edge and core Thomson scattering systems to obtain electron and temperature profiles from both regions in a single discharge [42].

The core system consists of 16 channels and has a spatial resolution of 25 mm, while the edge system with 10 channels is designed for a spatial resolution of 3 mm. The radial position of profiles obtain with the edge diagnostics can have uncertainties of up to 1.5 cm due to fluctuations of electron temperature and density in the SOL and uncertainties in the radial positions of the magnetic equilibrium.
Data from the Thomson scattering diagnostic is used in this thesis to compare simulated profiles of T_e and n_e to experimental data and to determine the electron density at the separatrix $n_{e,sep}$ as input parameter for simulations.

3.3.3 Bolometry

Bolometers measure the power of incoming electromagnetic radiation by measuring the heating of a material irradiated by the radiation. The heating is typically determined by the temperature-dependent electrical resistance of the material.
In fusion research bolometers are used to measure the spectrally integrated radiation from the plasma along a line of sight. By combining an array of bolometers it is possible to cover a plasma volume with several lines of sight to determine the total radiation from that volume.
ASDEX Upgrade has two different arrays of bolometers. A system of foil based bolometers with a timescale of a few milliseconds that consists of 128 lines of sight and an arrays of diode based bolometers that is able to resolve time scales down to 50 μs. The diode system's lines of sight duplicates the foil array's lines of sight with 256 lines to enable comparison and absolute calibration of both diagnostics [43]. Unlike the foil bolometers, the diode based bolometers measure the incident radiation power via a photocurrent and undergo a spectrally dependent degradation. In combination with the absolutely calibrated foil bolometers, however, the diode bolometers can be recalibrated while measuring the power deposition with high temporal resolution.
In this thesis bolometry data was used to estimate the effective fraction of heating and radiated power in chosen simulation volumes.

3.3.4 Infrared Thermography

To study the heat flux onto plasma facing components (PFCs) infrared (IR) thermography is widely used in fusion research facilities. ASDEX Upgrade is equipped with a real time capable system [44]. The IR camera measures a photon flux that is related to the surface temperature of the observed object via Planck's law. From the temporal evolution of the objects surface temperature the heat flux density onto that surface can be computed using the heat diffusion equation for the bulk of the object. For the real time system in ASDEX Upgrade this is done numerically by the THEODOR [45] code.

The heat flux densities on the outer divertor tiles obtained with infrared thermography is used in this thesis to compare simulated heat flux densities with experimental data.

3.3.5 Langmuir Probes

Langmuir probes consist of one or multiple electrodes that are inserted into the plasma. From the current-voltage characteristics of the plasma exposed probe tip the electron density, electron temperature and plasma potential can be extracted via modeling.
In the divertor of ASDEX Upgrade so called „triple probes“ [46], consisting of three electrodes, are installed. In contrast to probes with a single electrode, where the current-voltage characteristics is obtained by sweeping the voltage, triple probes measure three points of the current-voltage characteristic simultaneously. This allows for a much faster measurements at the cost of loosing some information about the exact shape of the characteristics.
In this thesis the electron temperature and the saturation current obtained from Langmuir probes at the inner and outer divertor tiles are used to compare simulated and experimental data.

3.3.6 Divertor and Midplane Manipulator Systems

To study plasma surface interactions two manipulator systems are installed at ASDEX Upgrade [47, 48] in the divertor and at the low field side midplane. They can be equipped with multiple probes ranging from sets of Langmuir probes to material samples that can be exposed to the plasma.
The mid-plane manipulator (MEM) consists of a long arm that can be be exposed to the plasma or also be retracted. Additionally, the probe head can be rotated. In figure 3.3 the deposition probe of the MEM is displayed with and without a cap to limit plasma exposure to specific areas of the cylinder. The cylinder itself consists of graphite and is coated with tungsten.
The manipulator system in the divertor (DIM) consists of two wall tiles at fixed positions. These tiles can either be equipped with a set of fixed probes that are replaced after a day of discharges, or with a probe head, that can be rotated after each discharge, to obtain discharge specific results. For the work in this thesis both manipulators were equipped with material samples to analyse the deposition of impurities during discharges in ASDEX Upgrade (see section 3.5). Figure A.1 (see appendix) is a photo of one wall tile of the DIM equipped with six samples in light grey and six dummy samples in dark grey.

3.3.7 Charge Exchange Recombination Spectroscopy

The charge exchange recombination spectroscopy (CXRS) diagnostics is used to determine impurity densities, temperatures and flows in fusion plasmas [49].

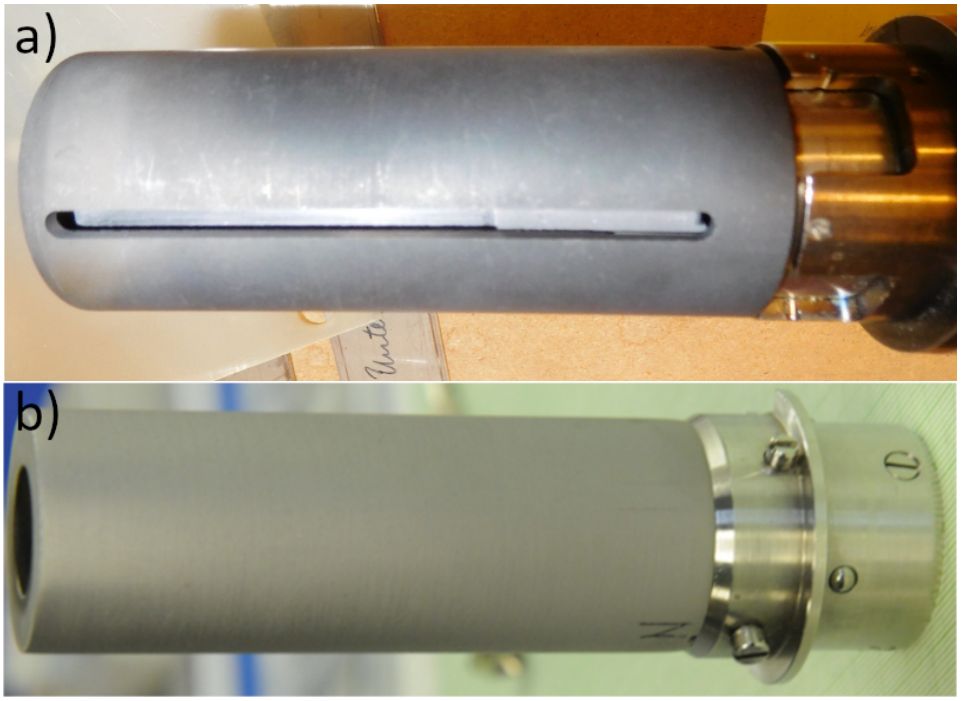

Figure 3.3: a) The deposition probe head covered with a cylinder as used in discharge #35616 and b) the tungsten coated graphite cylinder as used in discharge #32024.

It measures the spectral intensity distribution of photons emitted from the excitation decay of impurities in the plasma. The excitation is a result of a charge exchange between neutral atoms and impurity ions. In ASDEX Upgrade the CXRS utilises the radiation emitted from impurities after interacting with neutral particles from beam injection, a heating system that is described under section 3.4 [50]. Data evaluated by CXRS is used in this thesis to obtain experimental ion temperature profiles and compare them to simulated profiles.

3.3.8 Lithium Beam Spectroscopy

By injecting beams of atomic lithium into the plasma edge, it is possible to obtain highly spatially and temporally resolved electron density profiles [51, 52]. Due to collision of the neutral lithium atoms with plasma electrons, the Lithium atoms become excited and emit line radiation when going back to their groundstate. The lithium beam spectroscopy method at ASDEX Upgrade is based on the Li(2p) $\rightarrow$ Li(2s) emission at 670.8 nm, which is only weakly temperature dependent. Since this excitation comes from electron impact excitation the electron density is proportional to the intensity of the line radiation, $n_e \propto I_{2p \rightarrow 2s}$.
The lithium beam spectroscopy is used in this thesis to get reliable electron density profiles in the SOL for comparison with simulated profiles and to have another value for the electron density at the separatrix.

3.3.9 Integrated Data Analysis

The integrated data analysis (IDA) at ASDEX Upgrades combines the measurements from lithium beam (LB) spectroscopy, laser interferometry (LI), electron cyclotron emission (ECE) and Thomson scattering spectroscopy (TS) in an Bayesian probability framework to determine coherent profiles of n_e and T_e [53]. Therefore, Bayes theorem is applied to the likelihood and prior probability distribution functions (pdf) p of the diagnostics like

$$\begin{aligned} p\left(n_e, T_e | d_{LB}, d_{LI}, d_{ECE}, d_{TS}\right) \propto & p\left(d_{LB} | n_e, T_e\right) \\ & \times p\left(d_{LI} | n_e\right) \\ & \times p\left(d_{ECE} | n_e, T_e\right) \\ & \times p\left(d_{TS} | n_e, T_e\right) \\ & \times p\left(n_e, T_e\right). \end{aligned} \tag{3.1}$$

Here, d_X denotes the forward model of the diagnostics measurements. An explanation of the forward model and the construction of p based on the model can be found in [54] and [55], respectively. The prior pdf $p\left(n_e, T_e\right)$ is zero for negative densities and temperatures and includes vanishing gradients at the plasma center. Further, optional prior information is given in [53].

3.4 Heating Systems

ASDEX Upgrade is equipped with a variety of heating systems utilising different physical mechanisms. In the following the different systems are explained briefly.

3.4.1 Ohmic Heating

In section 2.2 it is briefly explained that the poloidal magnetic field is created by an induced electric current in toroidal direction. The current carrying electrons collide with the plasma particles resulting in electrical resistivity and hence in Ohmic heating of the plasma. Since the collisionality decreases with temperature, also the effective heating power decreases with temperature and hence the maximum achievable temperature with Ohmic heating is limited. To further increase the temperature additional heating mechanisms are necessary.

3.4.2 Microwave and Radio-Frequency Heating

Charged particles gyrate around magnetic field lines due to the Lorentz force. The respective cyclotron frequencies for ions and electrons, $\omega_{ci,ce}$, lie in the range of radio and microwave frequencies, respectively, for typical magnetic field strengths in magnetic confinement fusion.

Electro-magnetic waves with frequencies that are harmonics of $\omega_{ci,ce}$ can be absorbed by the plasma, heating the respective species. Heating schemes utilising this absorption are called ion and electron cyclotron resonance heating (ICRH and ECRH). Because the cyclotron frequency depends on the magnetic field strength the heating occurs locally and the heating position can be adjusted by tuning the frequency of the respective heating waves. The heated particles distribute the heating power via collisions with colder particles.

3.4.3 Neutral Beam Injection

Another scheme to heat a plasma is neutral beam injection, where highly energetic, neutral particles are injected into the plasma. Because neutral particles are not deflected by the magnetic field, the neutral beam can penetrate deep into the plasma, where the neutral particles ionise and distribute their energy via collisions. The high energetic beam ($60 - 100\,\mathrm{keV}$ [56]) usually consists of neutral hydrogen or deuterium atoms that not only heat, but also fuel the plasma.

3.5 Experimental results

In this chapter chosen discharges carried out in AUG are introduced and experimental results are presented. Discharge #32024 has been conducted in a previous post-doctoral study and was re-analysed for this thesis to conduct analyse the migration of ^{15}N with 3D codes. The discharge #35616 is an exemplary discharge of a discharge series conducted in the course of this thesis to study the sensitivity of ^{15}N deposition in the divertor and at the mid-plane on the seeding location of ^{15}N.

3.5.1 ASDEX Upgrade Discharge #32024

The L-mode discharge #32024 was conducted during post-doctoral studies by Gerd Meisl, IPP, to investigate the re-distribution of ^{15}N in AUG. It was part of the discharge series from #32019 to #32024 which had the purpose to study nitrogen migration and implantation in the first wall as well as to investigate the ammonia production in nitrogen seeded discharges. Related experimental and simulation results from 2D WallDYN studies are presented in [12].
In the present thesis the discharge was analysed to extract relevant data for 3D WallDYN modelling: plasma parameters of the discharge to produce a 3D plasma background and re-deposition measurements of ^{15}N in the divertor and at the mid-plane to compare 3D WallDYN results to experimental data. The re-deposition measurements were taken from [12], figure 6 and figure 8.
The plasma was electron cyclotron heated with 0.445 MW. The deuterium plasma was seeded with ^{15}N.
Discharges in AUG easily achieve H-mode and L-mode discharges often switch to the so-called I-phase, an intermediate mode with oscillations in the temperature and density profiles at the edge of the confined region, usually around $\rho = 0.95$. The discharge #32024 stays in L-mode for most of the time, while transitioning into I-phase from $t = 1.0$ to 2.5 s and around $t = 4.5$ s as indicated by the oscillations between $f = 3$ and 4 kHz in the spectrogram of Langmuir probe temperature data in figure 3.4. The corresponding Langmuir probe was located at $\rho = 1.01$ in the outer divertor.
Experimental deposition data usually represents the deposited impurities after either a single discharge or a discharge series. When modeling the deposition with simulation schemes like WallDYN, a static plasma background is assumed and hence it is important to analyse oscillations of plasma parameters to ensure the applicability of the model. I-phase oscillations in divertor data are usually not a big concern for impurity migrations studies, because the erosion yield time-averaged over the oscillations of the impact energy is close to the erosion yield of the time-averaged particle impact energy: $\langle Y_{\mathrm{ero}}\left(E(t)\right)\rangle_t \approx Y_{\mathrm{ero}}\left(\langle E(t)\rangle_t\right)$, if the oscillation amplitude is not too large.
Figure 3.5 a) shows time-traces of the fueling rates of D_2 and $^{15}N_2$ during discharge #32024. The ^{15}N seeding rate was modulated to achieve an average seeding rate of 2.9×10^{20} ^{15}Ns^{-1} [12]. Figure 3.5 b) shows the contribution

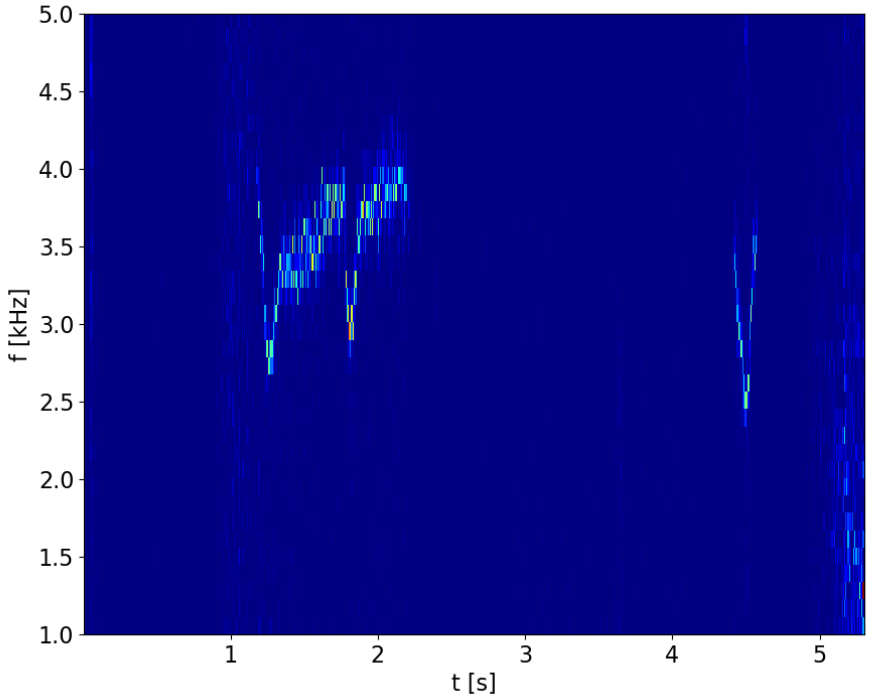

Figure 3.4: Spectrogram of the Langmuir probe temperature data at the outer divertor at $\rho = 1.01$ for discharge #32024.

of different heating schemes as well as the radiated power. The short NBI blips were used for spectroscopic measurements of the ion temperature of the plasma, while both ion density and electron density for this discharge were taken from the integrated data analysis software [53].
The electron density and temperature are constant during most the discharge, as displayed in figure 3.5 c) and d). The green area around $t = 3.0\,\mathrm{s}$ indicates the time window that is reproduced by simulations in section 4. The net input power, the radiated power and the separatrix density are taken from the time average from $t = 2.95$ to $t = 3.05\,\mathrm{s}$ and the experimentally obtained radial profiles of T_e and n_e are used as a benchmark for the simulated radial profiles.
To study impurity migration, deposition probes were installed on the divertor and the mid-plane manipulator systems (DIM and MEM), with the mid-plane probe slightly protruding out of the limiter shadows (see figure 3.7). The ^{15}N impurities were injected from two different valves at opposing toroidal angles in the divertor dome, while the main fueling species D was injected from one valve at the outer mid-plane and another valve in the divertor with a distance of roughly 67.5° in toroidal direction. For the D_2 fueling, the valves Co02A in sector 2 and Du05B in sector 5 were used and the $^{15}N_2$ impurities were seeded from valves Du09X and Du01X in sectors 9 and 1. All used seeding valves of relevance for this theses as well as the position of DIM and MEM are indicated

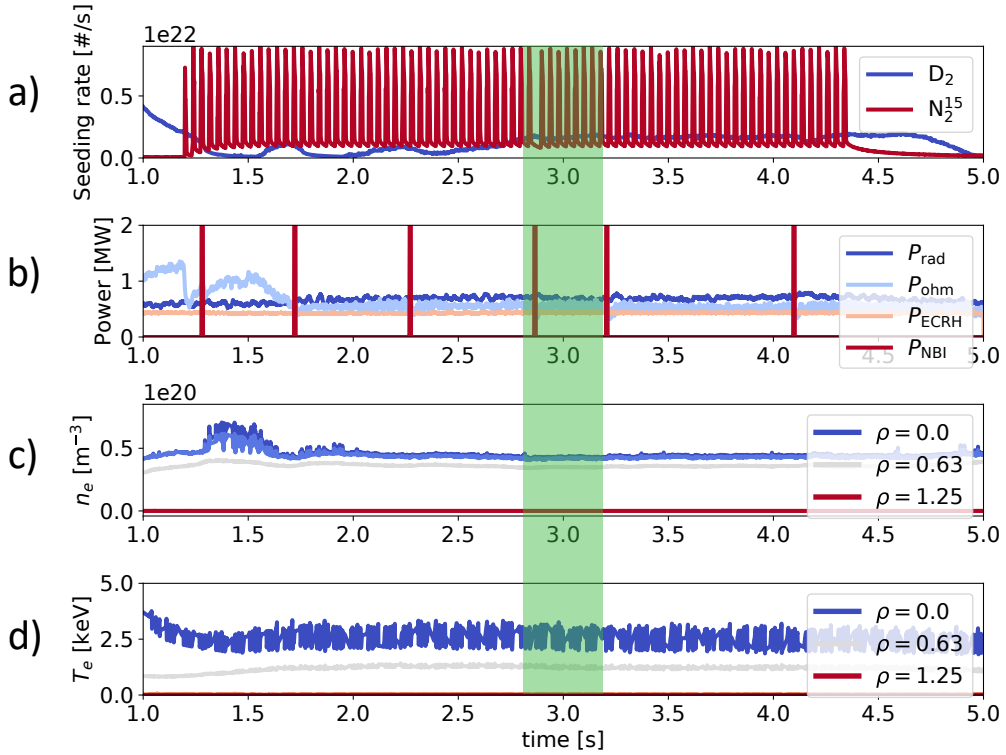

Figure 3.5: Time traces of the discharge #32024. a) Fueling rates of deuterium and nitrogen, b) radiated power and heating power of Ohmic heating, electron cyclotron heating and NBI blips, c) density at different radial positions, d) electron temperature at different radial positions.

in figure 3.6.
Figure 3.7 shows the magnetic configuration of the discharge with the separatrix as a solid red line. The positions of the MEM and DIM are indicated in blue and were not changed during the discharge series from #32019 to #32024. An example of how the DIM with deposition samples looks like can be seen in figure A.1 (in the appendix).
During the discharge series four sets of samples were exposed in the DIM [12] to study the dependence of deposited ^{15}N on the surface roughness:

- polished bulk W samples
- W coated fine grain graphite samples with polished surface
- W coated fine grain graphite samples with milled structure
- polished bulk Mo samples.

The results of NRA performed by G. Meisl [12] for the different samples are displayed in figure 3.8. More ^{15}N was deposited on the W coated milled and polished probes than on the bulk W and on the bulk Mo probes. The coated

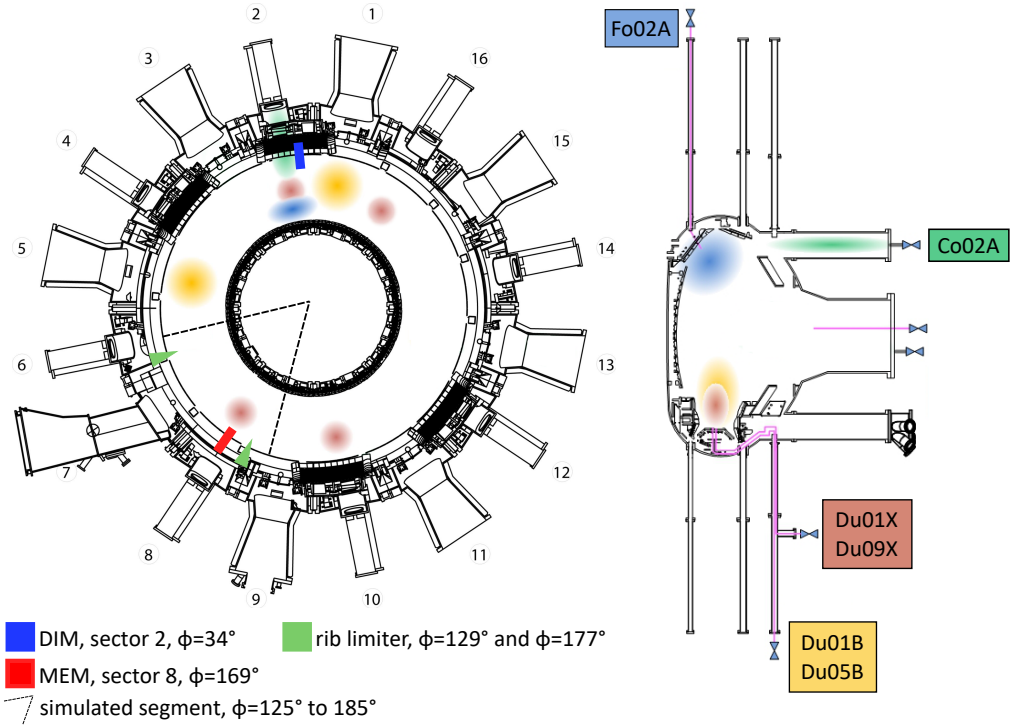

Figure 3.6: Position of gas valves used in the series of discharges around #32024 and #35616, an indicator of the simulated section and indicators for the positions of DIM, MEM and rib-limiters. Toroidal and poloidal cross section on the left and right, respectively.

probes also show a higher deposition close to the strikeline that the bulk probes. Additionally the deposition on bulk Mo samples is very similar to the deposition on bulk W samples. These measurements are compared with simulated ^{15}N deposition in the outer divertor in section 5.2.

In the discharge series the MEM probe was used without the cap, see figure 3.3 b), to investigate the dependence of ^{15}N deposition on the connection length between probe and nearby limiters, which is about 0.3 m for the nearby limiter and about 1.5 m for the distant limiter [12]. The ^{15}N deposition at the midplane deposition probe as determined by NRA is plotted in figure 3.9 with connection lengths represented by the angular position on the cylinder. The angles are defined as positive for deposition measurements pointing towards the nearby limiter (smaller connection lengths) and negative pointing towards the distant limiter (larger connection lengths), with 0° directed to the top of the vessel. The decay length lies between 0.6 cm for deposition profiles facing the nearby limiter (red values) and 3.0 cm facing the distant limiter (blue values) [12]. In section 5.2 the experimental ^{15}N deposition profiles between the angles of $85° - 95°$ and $-85° - -95°$ are compared to the front and backside of the MEM in WallDYN simulations, respectively.

It is apparent that the maximum areal densities measured in the divertor in figure 3.8 are more than three times higher compared to values at the midplane deposition probe in figure 3.9, even though the probe protruded out of

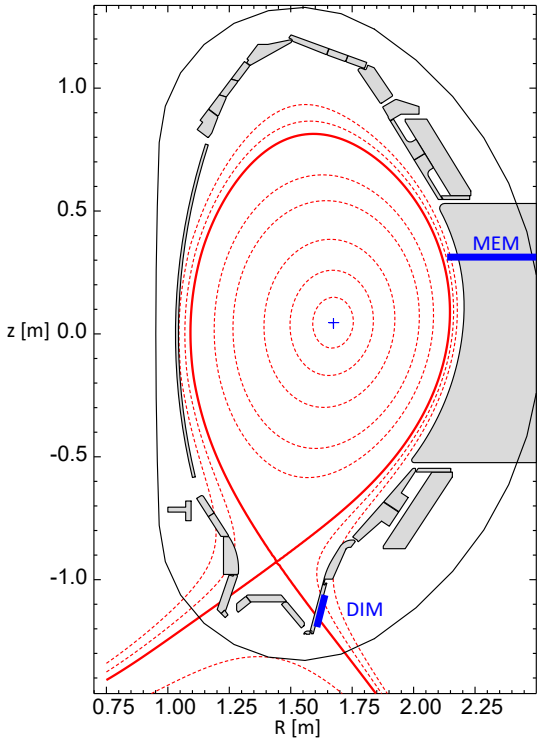

Figure 3.7: Magnetic configuration of discharge #32024 with indicators for the position of the mid-plane deposition probe (MEM) and the divertor manipulator samples (DIM).

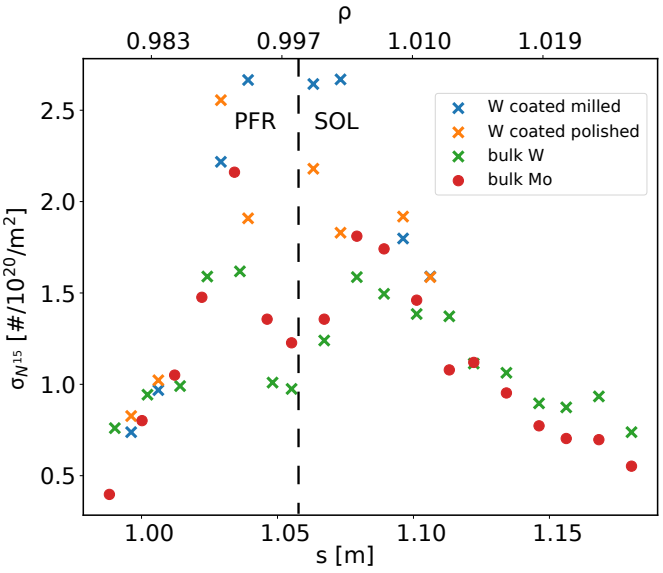

Figure 3.8: Areal ^{15}N density from NRA measurements of DIM samples exposed in the discharge series from #32019 to #32024. The vertical, dashed lines indicates the strikeline position. Data acquisition and analysis performed in [12].

the limiter shadow into the plasma. The experimental ^{15}N deposition results on both divertor and mid-plane deposition probe are crucial to benchmark

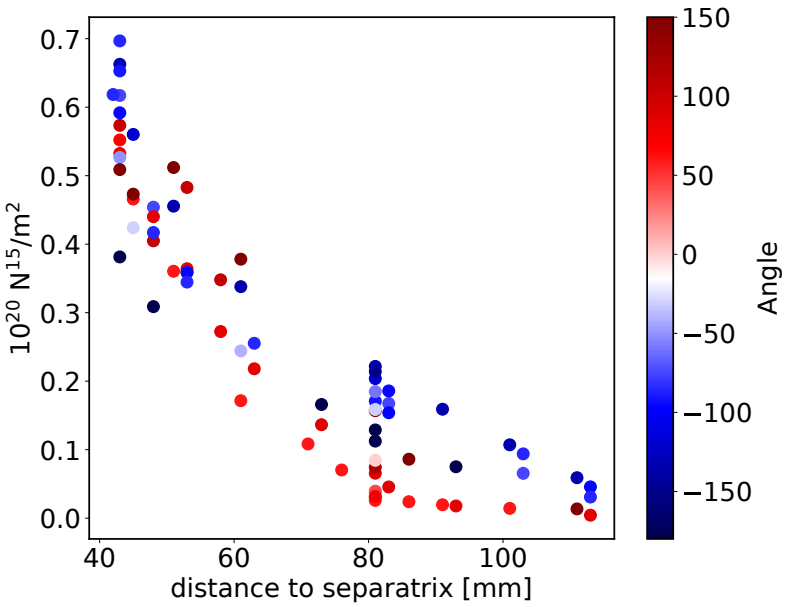

Figure 3.9: Areal ^{15}N density from NRA measurements of MEM sample exposed in the discharge series from #32019 to #32024. The angle represents the connection length between MEM and nearby limiters. Points on the probe facing the nearby limiter are red, while points facing the distant limiter are blue. Data and NRA performed in [12] by Gerd Meisl, IPP.

simulated deposition results of 3D WallDYN at two different locations.

3.5.2 ASDEX Upgrade Discharge #35616

To investigate the migration of ^{15}N, when seeded from the top instead of the divertor, and to obtain discharge resolved ^{15}N deposition profiles at the mid-plane the discharge series from #35609 to #35617 was conducted, where #35614 had no plasma. Discharge #35616 was electron cyclotron heated with 0.78 MW and aimed to be a flat top L-mode discharge. While the averaged divertor data implied stable conditions for discharges #35615 , #35616 and #35617, an analysis of divertor Langmuir data revealed that all discharges in the series were in I-phase.
Figure 3.10 depicts the spectrogram of Langmuir temperature data at $\rho = 1.01$ in the outer divertor during discharge #35616. During most of the flat top window from $t = 1.4$ to 5.0 s the spectrogram shows the typical I-phase oscillation in the range of 3 to 4 kHz.

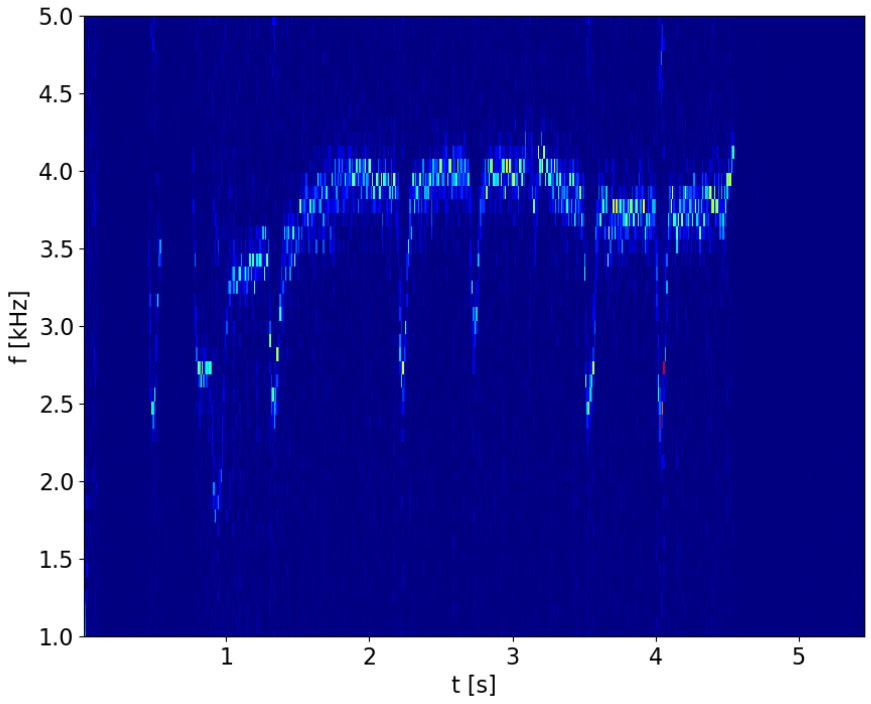

Figure 3.10: Spectrogram of the Langmuir probe temperature data at the outer divertor at $\rho = 1.01$ for discharge #35616.

A time-trace of gas fueling rates, heating power and radial values of electron density and temperature are shown in figure 3.11. The non constant fueling of D_2 is a result of a feedback mechanism to achieve stable divertor conditions. NBI blips in the heating time-trace were used to determine the ion temperature via CXRS and the green shaded area again indicates the time window reproduced by simulations in section 5.

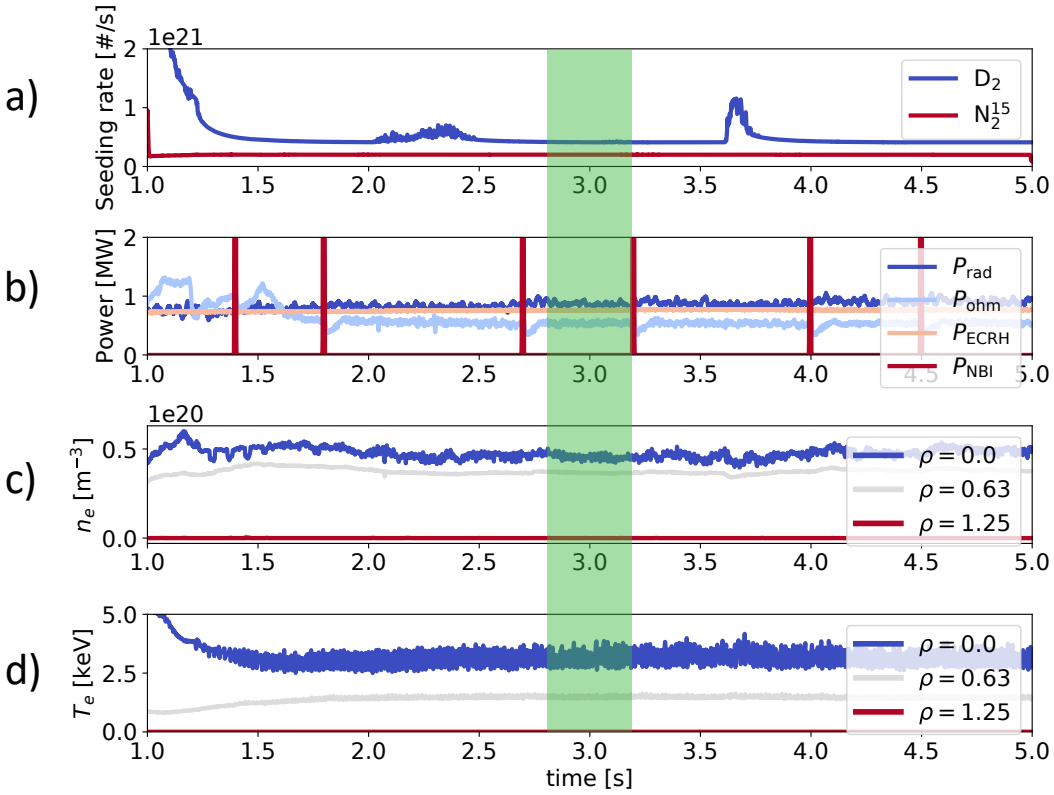

Figure 3.11: Time trace of the discharge #35616. a) Fueling rates of deuterium and nitrogen, b) radiated power and power Of ohmic heating, electron cyclotron heating and NBI blips, c) electron density and d) electron temperature at different radial positions.

The main plasma species deuterium was seeded from valves Du01B and Du05B in sectors 1 and 5 in the divertor and from valve Co02A at the top of the outer mid-plane in sector 2. The ^{15}N impurities were also seeded in sector 2 from valve Fo02A at the top of the chamber. The seeding valves are indicated in the figure 3.6.

The magnetic configuration in this discharge series was set to be identical to the configuration in #32024 which is displayed in figure 3.7. Magnetic reconstruction yields only a minimal difference in the configuration and both DIM and MEM were installed at the same positions as in previous discharges. The deposition head mounted on the MEM during this discharge series was covered by a cap with a slit and the tungsten coated graphite cylinder was rotated in between discharges to obtain discharge resolved and over several discharges accumulated deposition profiles. The W layer is about 2.5 μm thick with a Mo interlayer of about 1.3 μm thickness. In the appendix the depth profiles of the coating as given by the manufacturer can be found in figure A.3.

Four positions, separated by rotating the probe in-between discharges, were analysed with NRA to have both accumulated and discharge resolved deposition profiles for different plasma conditions:

- position 1 (accumulated): #35610 #35611 #35612
- position 2 (single discharge): #35613
- position 3 (accumulated): #35615, #35616
- position 4 (single discharge): #35617

The discharges in positions 1 and 2 still exhibited fluctuating divertor temperatures while the discharges from positions 3 and 4 showed more stable conditions.

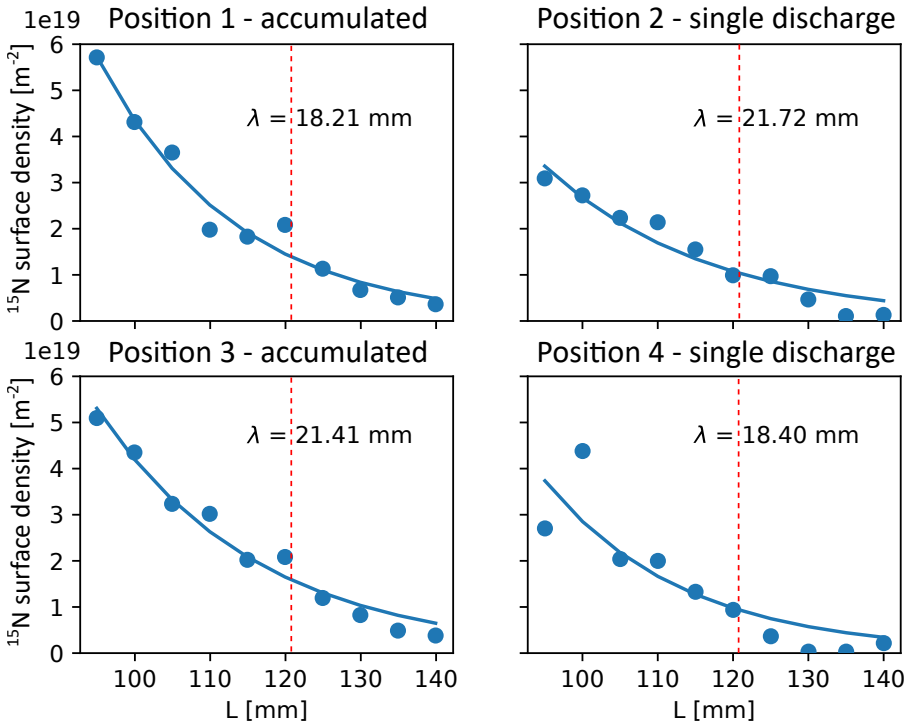

Figure 3.12: Areal density of ^{15}N deposited on the MEM probe over the distance in the NRA laboratory system L with an exponential fall-off length λ. The red dotted line indicates the limiter position during the experiments.

The exposure time per discharge is about 4 s and hence positions exposed to multiple discharges are subject to a higher ^{15}N fluence.
A photo of the deposition probe with cap is displayed in figure 3.3 a). Due to the cap a shadowing effect on ^{15}N deposition on the probe is expected, as the plasma flow along the magnetic field lines hits the probe at an oblique angle, resulting in parts of the probe being partially shielded by the cap (left figure in A.2, in the appendix). During NRA of the MEM cylinder after exposure to the discharge series it is therefore necessary to find the rotation angles with maximal deposition on the cylinder by analysing several angles at a fixed radial

position (right figure in A.2, in the appendix). Subsequent NRA measurements of the cylinder were conducted at angles with maximal deposition to exclude the shadowing effect in measured ^{15}N profiles.
Figure 3.12 shows the measured ^{15}N surface density plotted over the distance in the NRA laboratory system L along the cylindrical MEM probe for all four positions. The measured ^{15}N surface density for positions 2 and 4, where the probe was exposed to single discharges, is lower than the measured surface densities in positions 1 and 3, where the probes was exposed to several discharges and hence subject to a higher fluence of ^{15}N from the plasma. Additionally the amount of deposited ^{15}N at position 1 is only slightly larger than in position 3. Comparing the peak values of position 2 (exposed to a single discharge), position 3 (exposed to two discharges) and position 1 (exposed to three discharges) indicates a saturation of deposited ^{15}N with increasing fluence and thereby confirming results from [57, 58], where a saturation of deposited N in AUG wall elements was observed in laboratory experiments and after N seeded discharges in AUG.
The mean exponential fall-off length in figure 3.12 of $\lambda_{\text{mean}} \approx 20\,\text{mm}$ is well within the range of $\lambda = 6 - 30\,\text{mm}$ as obtained for the previous discharge series around #32024 in [12], where nitrogen was seeded from the divertor.
The peak value of $\sigma_{^{15}\text{N},peak} \approx 5.8 \cdot 10^{19}\,\text{m}^{-2}$ at position 1 in figure 3.12 corresponds to an accumulation after 3 discharges. Comparing this to a peak value of $6.5 \cdot 10^{19}\,\text{m}^{-2}$ after 5 discharges for the discharge series around #32024 in figure 3.9, shows that also the peak values are similar. As both fall-off lengths and peak values of nitrogen deposition profiles at the MEM are very similar despite the different nitrogen seeding location, it can be concluded that the deposition at the MEM is not strongly influenced by the seeding position.
For this discharge series the DIM (see section 3.3) was equipped with a total of 12 samples. Six probes were Mo coated carbon samples with different surface roughness, the other six probes are Mo covered and have Au markers. Three probes have 1 mm markers and the other three probes markers with a size of 5 mm. The six Mo coated samples were prepared with different surface roughness of $\text{R} = 4\,\text{nm}, 110\,\text{nm}, 280\,\text{nm}$ and $2\,\mu\text{m}$.
The NRA of the DIM samples was conducted by Aki Lahtinen, VTT. The results with indicators for the different samples and the strike point position are depicted in figure 3.13. The data left of the strike line lies in the private flux region, where only little ^{15}N is deposited, while most ^{15}N is deposited right of the strike line. Even though the particle fluxes are high at the strike line, the high temperature leads to strong re-erosion of deposited particles (see section 2.4.1) which typically results in a peak of deposition next to the strike line, where the re-eroded particles are directly re-deposited.

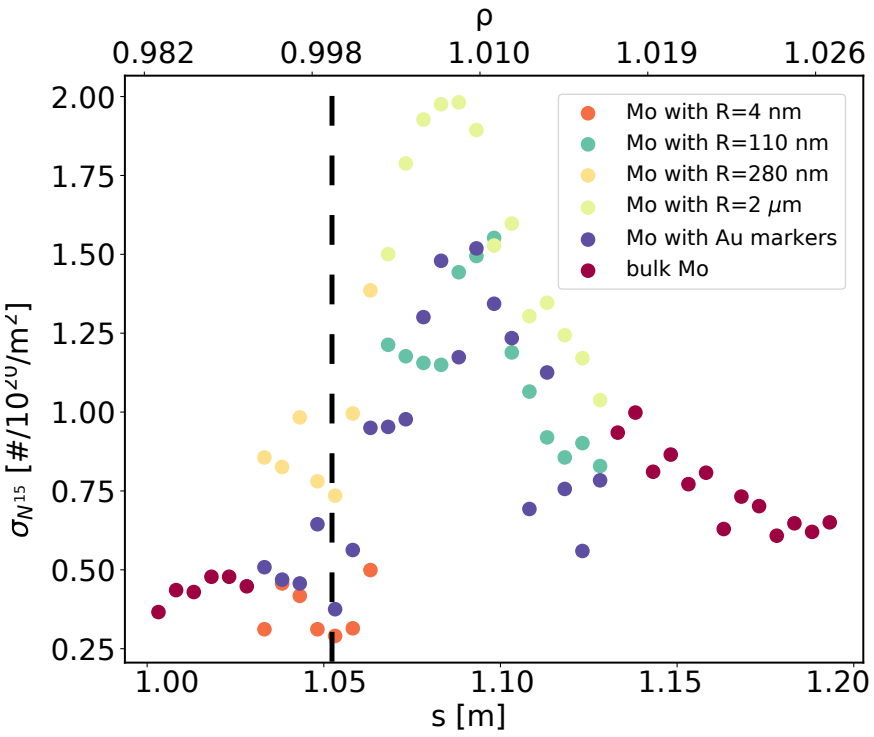

Figure 3.13: ^{15}N surface density profiles on the DIM samples exposed in the discharge series from #35610 to #35617. The vertical dashed line indicates the strike point position. Data and NRA from Aki Lahtinen, VTT.

Chapter 4

Impurity migration modeling

Several simulations schemes were used in the course of this thesis to simulate the migration of ^{15}N in ASDEX Upgrade with three dimensional wall geometries. The **E**dge **M**onte **C**arlo 3D (EMC3) [59,60] code (section 4.1) was used to simulate plasma backgrounds of conducted discharges. The SDTrimSP code (section 4.2) was used to generate databases for sputtering and erosion yields and to augment the WallDYN code (section 4.3). WallDYN calculates the time evolution of the impurity fluxes and surface composition based on plasma background solutions provided by EMC3-EIRENE. This chapter introduces the used simulation schemes and changes made to their default models.

4.1 The EMC3-EIRENE transport code

The EMC3-EIRENE code package treats the main plasma species as a fluid (see chapter 2.3.1) and includes impurity species via source and sink terms in the energy balance. Impurities are not treated as additional fluids. It can solve the Braginskii equations 2.12, 2.13 and 2.14 numerically in three dimensions and is able to deal with three dimensional magnetic field and wall geometries. In this thesis EMC3 has been used coupled to the Monte Carlo neutral particle code EIRENE [61].

4.1.1 Main Plasma

In section 2.3.1 the set of equations remains unclosed because the anisotropic part of the pressure tensor $\overleftrightarrow{\Pi}_a$ as well as the heat flux density $\vec{q}_a$ are still dependent on higher moments of the distribution function f_a. In EMC3 the equations are closed with a diffusive ansatz via

$$\overleftrightarrow{\Pi}_{a,\perp} = -\eta_{a,\perp}\frac{\partial u_{a,\parallel}}{\partial x_\perp} = -m_a n_a D_{a,\perp}\frac{\partial u_{a,\parallel}}{\partial x_\perp} \tag{4.1}$$

$$q_{a,\perp} = \chi_{a,\perp} n_a \frac{\partial T_a}{\partial x_\perp}, \tag{4.2}$$

where $D_{a,\perp}$ and $\chi_{a,\perp}$ are perpendicular particle and heat diffusivity of ion species a and input parameters determined by the user. Additionally the perpendicular, anomalous transport is assumed to follow a diffusion equation

$$\Gamma_{a,\perp} = n_a u_{a,\perp} = -D_{a,\perp} \frac{\partial n_a}{\partial \vec{x}_\perp}, \tag{4.3}$$

further simplifying the equations.
Source terms of 2.12, 2.13 and 2.14, indicated by S, stem from interactions with neutral particles and are calculated by EIRENE in the EMC3-EIRENE package. The in EMC3 implemented form of these equations and their Monte-Carlo solver method can be found in [62, 63].

4.1.2 Impurities

The basic idea of impurity transport in a plasma has been introduced in section 2.3.2. Assuming a force balance ($F_Z \stackrel{!}{=} 0$) in parallel direction in equation 2.16, i.e.

$$n_Z m_Z \frac{(v_Z - v_i)}{\tau_s} = -\frac{\mathrm{d}\left(n_Z T_Z\right)}{\mathrm{d}x_\parallel} + n_Z Z e E + n_Z \alpha_e \frac{\mathrm{d}T_e}{\mathrm{d}x_\parallel} + n_Z \beta_i \frac{\mathrm{d}T_i}{\mathrm{d}x_\parallel}, \tag{4.4}$$

and substituting the impurity pressure $p_Z = n_Z T_Z$ results in an explicit expression for the impurity velocity in parallel direction:

$$v_{Z,\parallel} = u_{a,\parallel} - \frac{\tau_s}{n_Z m_Z} \frac{\partial\left(n_Z T_Z\right)}{\partial x_\parallel} + \frac{\tau_s}{m_Z} \left[Z e E + \alpha_e \frac{\partial T_e}{\partial x_\parallel} + \beta_a \frac{\partial T_a}{\partial x_\parallel} \right]. \tag{4.5}$$

It is assumed that the impurity ions are in thermal equilibrium with the main ion species ($T_Z = T_a$) and that the temperature is constant on a field-line. Hence the second part of equation 4.5 can be interpreted as parallel diffusion with

$$v_{Z,\parallel}^{diff} = -\frac{\tau_s T_a}{n_Z m_Z} \frac{\partial n_Z}{\partial x_\parallel} = -\frac{1}{n_Z} D_{Z,\parallel} \frac{\partial n_Z}{\partial x_\parallel}. \tag{4.6}$$

The radial impurity drift is assumed to be anomalous, similar to the ansatz in equation 4.3 for the main ions and hence the particle balance of impurities of charge state Z can be written as

$$\frac{\partial n_Z}{\partial t} + \frac{\partial\left(n_Z v_{Z,\parallel}\right)}{\partial x_\parallel} - \frac{\partial}{\partial x_\perp} \cdot \left(n_Z D_{Z,\perp} \frac{\partial n_Z}{\partial x_\perp} \right) = S_Z^{ion} + S_Z^{rec}, \tag{4.7}$$

where S_Z^{ion} and S_Z^{rec} are the effective particle sources from ionisation and recombination coming from charge states $Z-1$ and $Z+1$, respectively.

In a simulation run with impurities the interaction with the main plasma is given by an additional term $-S_{imp}$ on the right hand side of the energy balance (equation 2.14), that describes the cooling of the main plasma due to impurity

radiation and collisional ionisation of impurities. The cooling term for an impurity with maximum charge state Z_{max} reads

$$S_{imp} = \sum_{Z=1}^{Z_{max}} P_{rad,Z} + \sum_{Z=0}^{Z_{max}-1} E_n S^{ion}_{Z\rightarrow Z+1}, \tag{4.8}$$

where $P_{rad,Z}$ is the radiation loss from impurities of charge state Z and E_n is the ionisation energy for charge state Z to $Z+1$.
The parallel position update of impurity particles in EMC3 in principle follows [13]

$$\Delta x_{Z,\parallel} = v_{Z,\parallel}\Delta t, \tag{4.9}$$

for a time step Δt. As $v_{Z,\parallel}$ is computed from equation 4.5 with the assumption of a force balance in parallel direction and in absence of strong gradients and parallel electric fields the impurity velocity in parallel direction is equivalent to the parallel velocity of the main plasma species ($v_{Z,\parallel} = u_{a,\parallel}$). The time to accelerate impurity ions to the background velocity is in these cases ignored. With the additional assumption of $T_Z = T_a$ furthermore the time for thermalisation of impurity ions and main plasma ions has been omitted. Since this assumption also defines a diffusive component for $v_{Z,\parallel}$ the model using equation 4.5 with the assumption $T_Z = T_a$ is called the diffusive model.
The thermalisation time and the omitted time for $v_{Z,\parallel}$ to accelerate to $u_{a,\parallel}$ is not an issue for light impurities in general, but can be quite significant for heavy impurities due to their high inertia.
Therefore, a so called kinetic model [13] was implemented, where the parallel impurity velocity and the impurity temperature are updated stepwise following

$$\begin{aligned}
\Delta v_{Z,\parallel} &= \frac{u_{a,\parallel} - v_{Z,\parallel}}{\tau_s}\Delta t + \sigma\sqrt{\frac{T_Z}{m_Z}\frac{2\Delta t}{\tau_\parallel}} \\
&\quad + \left(\frac{ZeE}{m_Z} + \frac{\alpha_e}{m_Z}\frac{\partial T_e}{\partial x_\parallel} + \frac{\beta_i}{m_Z}\frac{\partial T_i}{\partial x_\parallel}\right)\Delta t \\
\Delta T_Z &= \frac{T_a - T_Z}{\tau_T}\Delta t \\
\Delta x_\parallel &= v_{Z,\parallel}\Delta t + 0.5\Delta v_{Z,\parallel}\Delta t,
\end{aligned} \tag{4.10}$$

with τ_s being the Spitzer collision time (equation 6.35 in [24]), $\tau_\parallel$ the parallel collision time (equation 6.37 in [24]) and τ_T the thermalisation time (equation 6.97 in [24]). σ is a random number drawn from a Gaussian distribution with $\langle\sigma\rangle = 1$ and is implemented as $\sigma = \sqrt{-2\log\eta_1}\cos 2\pi\eta_2$, where η_1 and η_2 are uniform random numbers $\in [0,1]$. In [13] the kinetic model was compared to the diffusion-convection model. In the kinetic model the charge state integrated impurity density along a view line through the plasma is up to 100 times smaller for tungsten, while it is only up to 3 times smaller for carbon.

Hence, the kinetic model was used to calculate the WallDYN redistribution matrices for tungsten and nitrogen in this thesis.
The background plasma solutions for discharges #32024 and #35616 were calculated with the diffusive model because these simulations only include the main plasma ions and ^{15}N.

4.2 SDTrimSP

SDTrimSP [64,65] is a Monte Carlo code used to simulate projectile trajectories in solids utilizing the binary collision approximation (BCA), which is described in section 2.4. It determines the scattering angles from randomly chosen impact parameters following

$$p = p_{max}\sqrt{R}, \tag{4.11}$$

with $R \in [0, 1]$ being random and p_{max} the maximal impact parameter, which is computed from the average volume where a single collision can occur. For a cylinder with radius p_{max} and length λ one obtains

$$p_{max} = (\pi\lambda N)^{-\frac{1}{2}}, \tag{4.12}$$

where N is the number density of the target and λ is the mean free path between successive collisions which is assumed to follow the liquid model [27]

$$\lambda = N^{-\frac{1}{3}}. \tag{4.13}$$

Parameters for each collision are chosen according to these equations and the whole projectile trajectory is calculated.
SDTrimSP features a static and a dynamic mode. In the static mode the composition is fixed and sputter and reflection yields of given projectiles on a given composition can be computed. In the dynamic mode, the target composition is modified by sputtering, implantation and recoils within the target [64]. This mode allows to model mixed material formation and layer growth. Main input parameters are the surface binding energies, the choice of the scattering potential and the angle of incidence (compare to equation 2.39 in section 2.4).

4.3 WallDYN

Impurity migration, as introduced in section 2.3.3, governs the evolution of surface compositions as well as the impurity sources from sputtering at plasma facing components and hence contributes to the impurity content in the plasma and the retention of potentially radioactive fuel in the walls.
Modeling impurity migration consists of three major parts: transport in the plasma to determine the impurity fluxes onto different wall tiles, the computation of sputtering sources dependent on the surface composition and the evolution of the surface composition based on the incoming impurity fluxes.

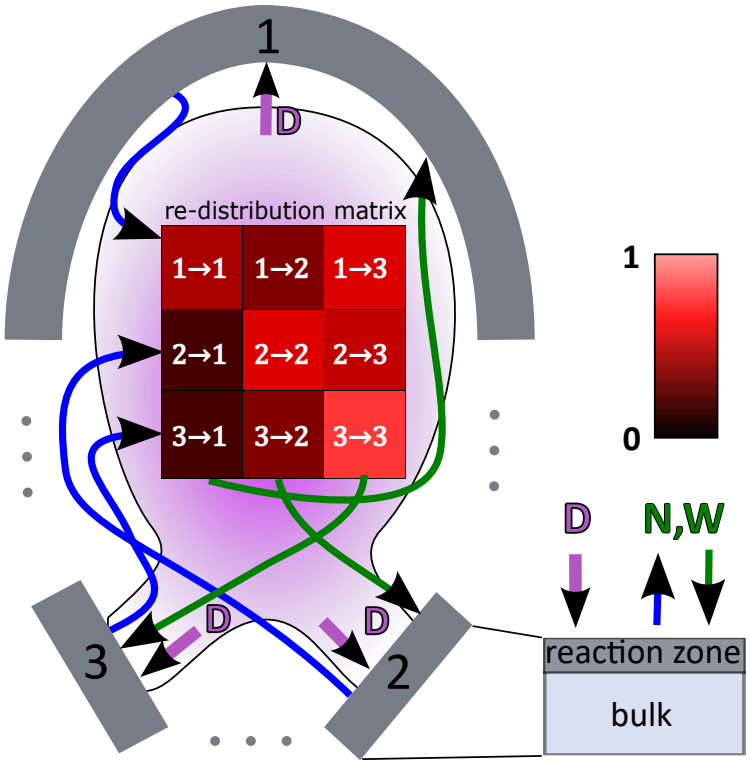

Figure 4.1: The WallDYN simulation scheme with three wall tiles, the redistribution matrix and the structure of a wall tile.

The link between the impurity fluxes onto the wall tiles and impurity sources is the transport in the plasma.
The code WallDYN [13,26] has been developed to calculate the surface compositions and impurity fluxes onto the wall self consistently by combining models for impurity transport with models for plasma-wall-interaction. To that end the wall structure of the modeled experiment is discretised into wall tiles.

4.3.1 Transport model

Each tile wk consists of a reaction zone and a bulk, illustrated in figure 4.1. The evolution of the composition of the reaction zone is calculated from a balance of particle influx Γ^{in} onto the tile and particle outflux (erosion, reflection, sublimation) into the plasma. To maintain a constant areal density (i.e. thickness) of the reaction zone it exchanges a flux with the bulk Γ^{bulk}: For net erosion material is moved from bulk to reaction zone and for net layer growth from reaction zone to the bulk. The transport of particles through the plasma is parametrised by a re-distribution matrix calculated with the kinetic transport model in EMC3-EIRENE. Each entry of this matrix contains the fraction of particles eroded from one wall tile and re-deposited on another wall tile.
In figure 4.1 the WallDYN scheme is illustrated for three wall tiles, a D plasma

with nitrogen and tungsten impurities. On each wall tile the incoming fluxes of tungsten, deuterium and nitrogen can lead to an outflux of nitrogen and tungsten. These impurities are transported through the plasma and deposited on all wall tiles with fractions determined by the pre-calculated re-distribution matrix.
The time evolution of the areal density $\sigma_{el,wk}$ for an particles species el on wall tile wk is implemented as the sum over charge states ql

$$\begin{aligned}\frac{\partial \sigma_{el,wk}}{\partial t} = &\sum_{ql}^{Z_{el}^{max}} \left(1 - RY_{el,ql,wk}\left(\sigma_{wk}, E_{el,ql,wk}, \alpha_{impact}\right)\right) \cdot \Gamma^{in}_{el,ql,wk} \\ &- \sum_{ej} \sum_{qj}^{Z_{ej}^{max}} C_{el,wk} \cdot SY_{el,ej,qj,wk}\left(\sigma_{wk}, E_{el,ql,wl}, \alpha_{impact}\right) \cdot \Gamma^{in}_{ej,qj,wk} \\ &+ \Gamma^{Bulk}_{el,wk},\end{aligned} \tag{4.14}$$

with the reflection yield RY, which depends on the surface density σ_{wk} of particle species el on wall tile wk, the particle impact energy at that wall tile $E_{el,ql,wk}$ and the particles impact angle α_{impact}. The sputter yield $SY_{el,ej,qj,wk}$ of particles species el by particles species ej with charge state qj on wall tile wk depends on the same parameters as the reflection yield. $C_{el,wk}$ is the concentration of particle species el on wall tile wk and Γ^{in} is the incoming flux that is calculated by

$$\begin{aligned}\Gamma^{in}_{el,q,wk} = \sum_{wj} \mathrm{M}_{el,q,wj,wk} \cdot \Bigg(&\sum_{ql}^{Z_{el}^{max}} RY_{el,ql,wj}\left(\sigma_{wj}, E_{el,ql,wl}, \alpha_{impact}\right) \cdot \Gamma^{in}_{el,ql,wj} \\ &- \sum_{ej} \sum_{qj}^{Z_{ej}^{max}} C_{el,wj} \cdot SY_{el,ej,qj,wj}\left(\sigma_{wj}, E_{el,ql,wl}, \alpha_{impact}\right) \cdot \Gamma^{in}_{ej,qj,wj} \\ &+ \Gamma^{src}_{el,qj,wj} \Bigg),\end{aligned} \tag{4.15}$$

where Γ^{src} represents additional fluxes into the plasma, e.g. impurity seeding, and M denotes the so called redistribution matrix $\mathrm{M}_{el,q,wj,wk}$, which is the charge state resolved parametrisation of transport of particles species el with charge q from wall tiles wj to tiles wk.
The reflection yield RY and the sputter yield SY are fitted to a database of static SDTrimSP (see section 4.2) simulations that cover the necessary range of impact angles, projectile energies and surface compositions.
The projectile energy of ions of particle species el with charge state ql on wall tile wk is assumed to follow $E_{el,ql,wl} = 3qlT^{e}_{wl} + 2T^{i}_{wl}$ in WallDYN (see equation

2.21), where the electron and ion temperatures in front of the wall tiles are taken from the plasma background. The particle impact angle α_{impact} can be set manually for every wall tile and depends on the magnetic configuration and the surface roughness of the material [66].
The original WallDYN code could only handle toroidally symmetric wall configurations because it used both plasma background solution and parametrised impurity transport results from codes that assumed toroidal symmetry (SOLPS [67] and DIVIMP [68]).
The 3D version of WallDYN [13] used in this work is coupled to EMC3-EIRENE (section 4.1) and uses the kinetic impurity model on a previously converged plasma background simulation.

4.3.2 Nitrogen surface model

The original WallDYN surface model calculates the areal densities of species by their sputter and reflection yields that are dependent on the dynamically updated surface compositions. For some gaseous species, however, the areal density saturates as a result of degassing and the original surface model is no longer sufficient.
Therefore WallDYN features an effective reflection yield which depends on the concentration of a given species in the surface. At high concentrations the reflection yield is artificially set to 1 at a user specified maximum concentration $c_{\max}$. The implemented form of this effective reflection coefficient reads

$$RY^{\text{effective}} = I\left(c\right) + \left(1 - I\left(c\right)\right) \cdot RY. \tag{4.16}$$

Here, RY is the unmodified reflection yield used in the original surface model and $I\left(c\right)$ is a unit-less function $\in [0, 1]$ that ramps up the reflection yield as

$$I\left(c\right) = \frac{1}{2} + \frac{1}{2}\tanh\left(\alpha\left(c - c_{max}\right)\right) \tag{4.17}$$

where c is the concentration of the species in the reaction zone and α a control parameter to set the steepness of the saturation ramp with a default value of $\alpha = 100$. The value for $c_{\max}$ has to be chosen considering that the reaction zone averages the concentration over the surface and depth of a wall tile.

4.3.3 Comparing WallDYN with SDTrimSP

The sputter and reflection yields of WallDYN are fitted against a database of static SDTrimSP simulations, covering the necessary range of impact angles, impact energies, impacting particle mixtures and surface compositions.
Those fits very well reproduce the SDTrimSP results for a homogenous concentration profile over depth. However, in a dynamic calculation the deposition is depth dependent and the single reaction zone in WallDYN cannot resolve these effects like SDTrimSP in a dynamic run with high resolution depth sampling.

For gaseous species the WallDYN surface model is sensitive to the species' concentration in the reaction zone, setting a too thin or too thick reaction zone influences the onset of the increased reflection coefficient that simulates out-gassing at high concentrations.
Therefore the WallDYN surface model was benchmarked against dynamic SDTrimSP simulations to compare reflection and sputter yields as well as surface concentration and areal density for varying particle energies, incoming particle mixtures of ^{15}N and ^{2}H and reaction zone width. The angle of impact was kept constant at 48 °.

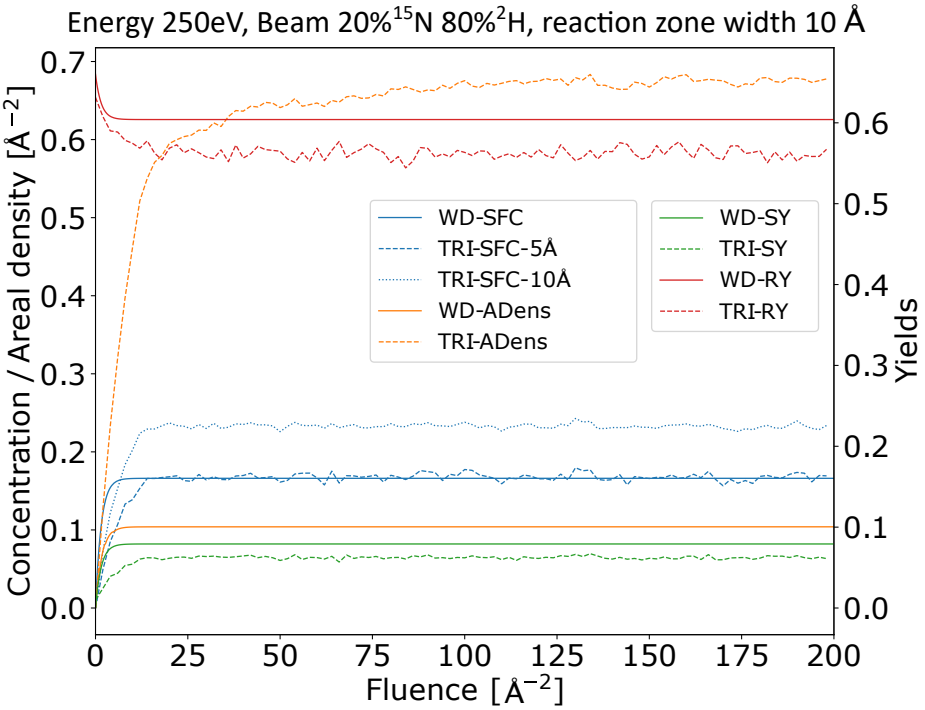

Figure 4.2: Comparison of the WallDYN surface model (WD) to SDTrimSP (TRI). SFC is the surface concentration of nitrogen, ADens is the nitrogen areal density and SY and RY are the sputter and reflection yield.

An example of such a comparison can be seen in figure 4.2, where both models are compared for an incoming particle flux consisting of 20 % of ^{15}N and 80 % of D at a particle energy of 250 eV. The values of interest are the ones for ^{15}N. Depicted are the surface concentration (SFC), the areal density (ADens) as well as the sputter and reflection yield (SY and RY) for the WallDYN surface model (WD) and the SDTrimSP simulation (TRI) over the fluence. In the WallDYN surface model the surface concentration is simply the concentration of a species in the reaction layer. SDTrimSP on the other hand features actual depth profiles and hence the surface concentration is the surface averaged concentration in a given depth. For figure 4.2 the surface concentration in SDTrimSP was averaged over two depths to be comparable to the concentra-

tion in WallDYN. For TRI-SFC-10Å the depth was chosen according to the WallDYN reaction zone width, i.e. 10 Å for this figure. TRI-SFC-5Å averages the concentration over the depth of 5 Å as specified in the SDTrimSP input file.
The concentrations obtained from WallDYN matches the concentration obtained from SDTrimSP better when SDTrimSP is only averaged over 5 Å. The SDTrimSP result for 10 Å yields a higher concentration than in the 5 Å case, revealing that more ^{15}N has been implanted between 5 and 10 Å than in the first 5 Å. The absolute values of sputter and reflection yield is quite close for both simulations, but there is a massive difference in the areal density.

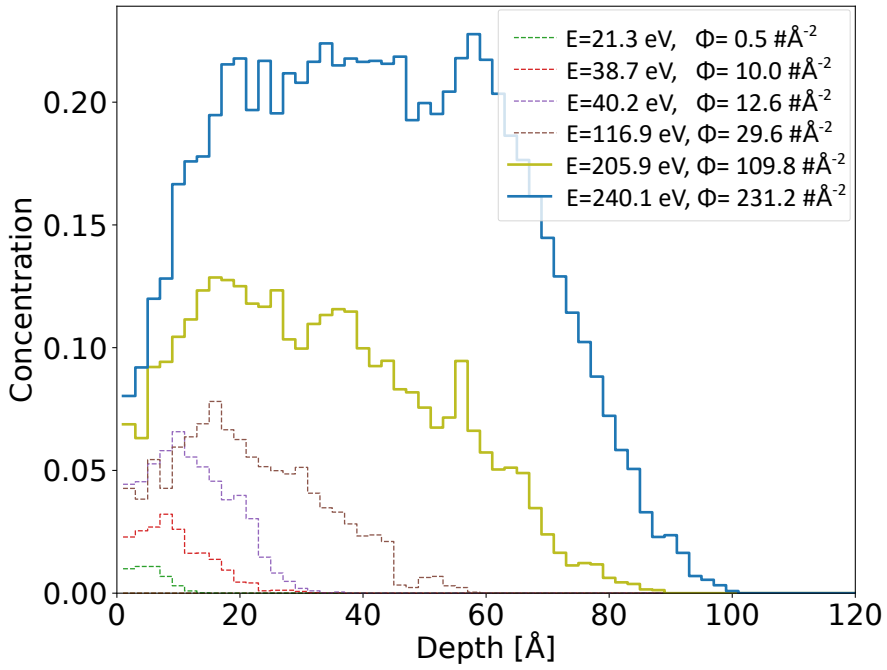

Figure 4.3: ^{15}N concentration calculated by SDTrimSP plotted over the depth for different impact energies and fluences.

As indicated by the different concentrations for different averaging depths in figure 4.2 the concentration and hence the areal density has a depth dependency. The ^{15}N concentration profiles are plotted for several impact energies and fluences in figure 4.3. While for the lowest energy and fluence the profile is almost flat over the first few Å, the maximum concentration of implanted ^{15}N shifts deeper for increasing energy.
In SDTrimSP the implantation depth depends on the impact energy while erosion processes occur on the very surface. Hence, particles can be implanted behind the eroded layers. In WallDYN all processes occur in the reaction zone and implanted particles can be eroded independently of their impact energy and hence their theoretical deposition depth. The WallDYN surface model

can therefore reproduce appropriate sputter and reflection yields, but cannot describe profile effects which lead to deviations in calculated surface concentrations and especially areal densities when compared to SDTrimSP.
To ensure that the profile effects do not impact the overall redistribution of impurity fluxes within WallDYN it is important to ensure that the gross erosion at every tile is comparable to SDTrimSP. The gross erosion is the sum of the sputtered flux and the reflected flux at a given tile

$$\Gamma^{Gross} = \Gamma^{Ero} + \Gamma^{Refl} \tag{4.18}$$

and describes the total outflux of particles at a tile.
In figure 4.4 the gross erosion fluxes of SDTrimSP and WallDYN are compared for identical input parameters that were taken from the WallDYN3D simulation of discharge #32024. Both fluxes are very similar for the displayed wall tiles. Checking the fluxes along all wall tiles shows that WallDYN predicts slightly higher gross erosion fluxes than SDTrimSP for most tiles, with an exception directly at the strike line, where WallDYN predictions are up to 40 % higher. It can be concluded that while WallDYN predicts a slightly larger gross erosion flux, the fluxes and hence the redistribution of impurities can still be adequately calculated, even though the missing depth profile effects lead to wrong areal densities.

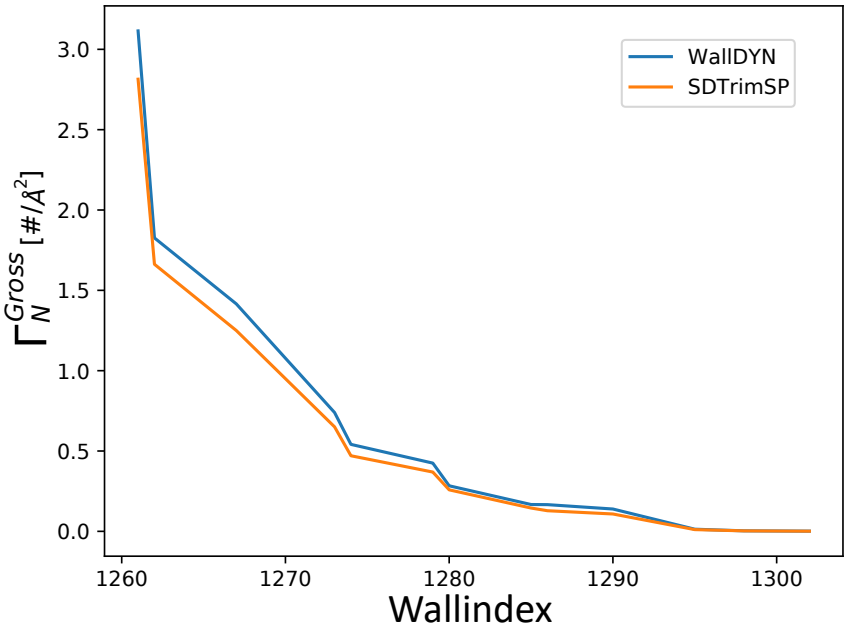

Figure 4.4: Comparison of the gross erosion fluxes of SDTrimSP and WallDYN3D at the mid-plane collector probe from a WallDYN3D simulation of discharge #32024.

As the influx at every wall tile is calculated from the gross erosion fluxes of all other wall tiles multiplied with the redistribution matrix it follows that

WallDYN adequately calculates the incoming fluxes Γ^{in} from equation 4.15. To include the profile effects and hence accurately calculate the areal densities it was decided to augment WallDYN by subsequent SDTrimSP simulations for every wall tile. The SDTrimSP simulations are set up with the converged incoming fluxes as calculated by WallDYN.
To demonstrate this coupling, figure 4.5 shows the surface concentration (SFC) and areal density (ADens) of ^{15}N as calculated by WallDYN compared to the surface concentration and areal density as calculated by a subsequent SDTrimSP run at wall indices associated with the MEM in a WallDYN3D simulation. The surface concentration of the SDTrimSP run is about a factor of two higher than in WallDYN at the higher wall indices, but matches very well at lower wall indices. This was expected due to higher particle impact energies at the higher wall indices and hence a stronger influence of the depth profile effects. The missing depth profile effects in WallDYN lead to a mainly flat areal density profile, because all implanted particles are re-emitted from the reaction zone. With the same particle energies and fluxes, SDTrimSP predicts significant deposition of ^{15}N at the higher wall indices, because the particles are implanted behind the strongly eroding surface layer.

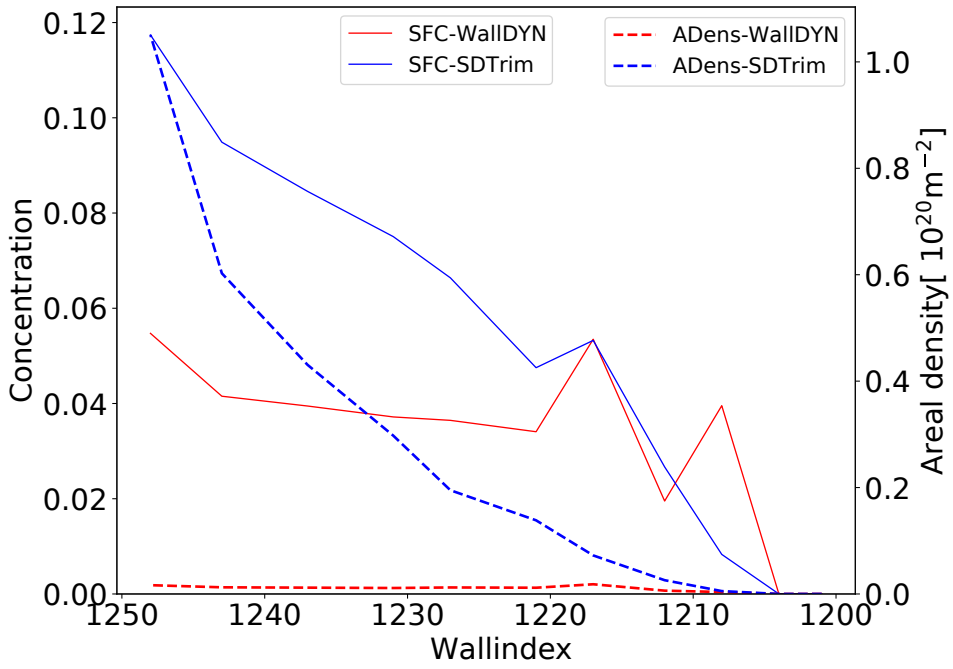

Figure 4.5: Concentration and areal density of ^{15}N calculated by WallDYN for the MEM and by a subsequent SDTrimSP simulation with input parameters calculated by WallDYN.

4.3.4 Normalisation of the 3D redistribution matrix

In 3D geometry the simulation space is not fully enclosed by wall elements and launched particles can leave the plasma simulation domain without intersecting a wall tile. Hence for some wall tiles, the amount of particles launched from the tile is larger than the amount of particles deposited on other wall tiles and the redistribution matrix does not satisfy particle conservation. These lost particles are no longer counted in the material balance and it is effectively assumed that they are deposited at surfaces behind the first wall structure. For non recycling species, like Be, this assumption is justified. However, recycling species like N will not stick to these surfaces indefinitely and will eventually re-enter the simulation domain. To take this into account the redistribution matrix was normalized for recycling species:
If particles are counted as lost because they left the simulation domain close to pumping ducts they are considered to actually be lost. Other particles, however, eventually re-enter the simulation domain at the same or another location and are not lost. This issue occurs predominantly on the LFS in the main chamber, between rib limiters, where the plasma grid ends in vacuum and does no longer cover any plasma facing components, and on the top of the geometry, where the plasma grid does not reach up to the first wall (see figure 4.7). Particles lost in these areas have to be considered in the redistribution scheme and should not be ignored.
For that purpose two different methods for normalising the redistribution matrix were developed: In the default normalisation approach the main chamber part of the redistribution matrix is multiplied with a normalisation factor calculated as

$$\sum_{i,j} M_{ij} = M \leq N, \qquad \text{and} \qquad f_{default} = \frac{N}{M}, \tag{4.19}$$

where N is the number of wall tiles in the main chamber and i, j are indices of these wall tiles. The redistribution matrix is then normalized following

$$M_{ij,default}|_{chamber} = M_{ij,original}|_{chamber} \cdot f_{default}, \tag{4.20}$$

for each wall tile in the main chamber. This approach is based on the launch location of particles, as the normalization of wall tiles determines the factor f. Particles lost from wall tiles in the main chambers are effectively added to the main chamber sources. A visualisation of the default normalisation approach can be seen in figure 4.6. The wall tiles coloured in purple are associated with the main chamber and are normalised with the above mentioned method.
An additional region of interest is the private flux region, where the plasma grid does not intersect with the dome structure, as indicated by the thick line in cyan in figure 4.6. Hence, ionized particles are counted as lost even though they left the grid directly above the dome structure, making the dome a perfect particle sink, which is not physically accurate. This has been corrected by

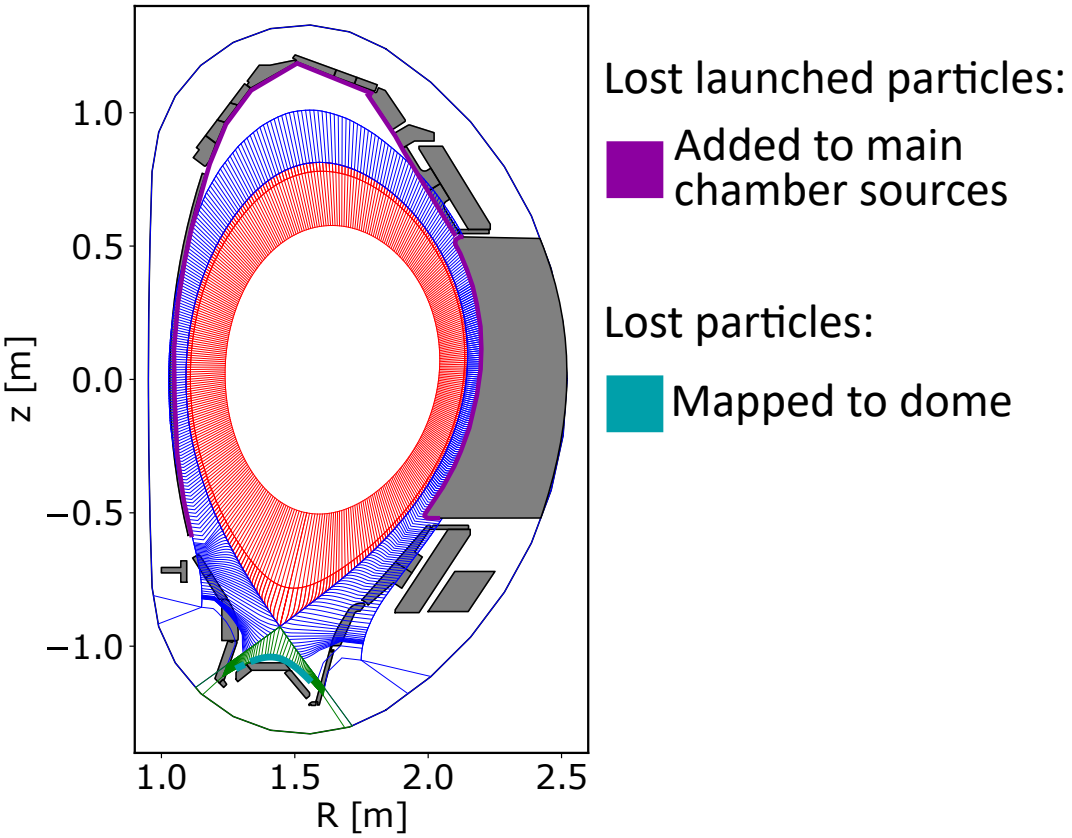

Figure 4.6: Schematics of the matrix normalisation via the default normalisation.

considering particles from every launch tile and mapping particles lost in the cells above the dome directly onto the nearest wall tile. The additional charge state resolved particle flux onto the wall tiles in the dome is then used to recalculate the redistribution matrix. In the actual WallDYN simulation the dome tiles then have a non-zero particle influx and are taken into account as normal wall tiles in the dynamic redistribution scheme.
The second approach is based on the location, where the particle loss occurred and has been named the adapted normalisation. Here, the normalisation factor $f_{adapted}$ is calculated by counting all particles lost in the main chamber and adding them, separated by charge state, to the already deposited particles in the main chamber as

$$f_{adapted} = \frac{\#deposited_{chamber} + \#lost_{chamber}}{\#deposited_{chamber}}. \tag{4.21}$$

Similarly to the default normalisation, the main chamber part of the redistribution matrix is then normalized by

$$M_{ij,adapted}|_{chamber} = M_{ij,original}|_{chamber} \cdot f_{adapted}. \tag{4.22}$$

In figure 4.7, the locations associated with the main chamber are coloured in purple. Particles leaving the grid boundaries indicated by the thick red lines

are assumed to be pumped away and are counted as lost particles. The dome part of the redistribution matrix is normalised identically in both normalisation approaches. The effect of the two different normalization approaches will later be compared in section 5.

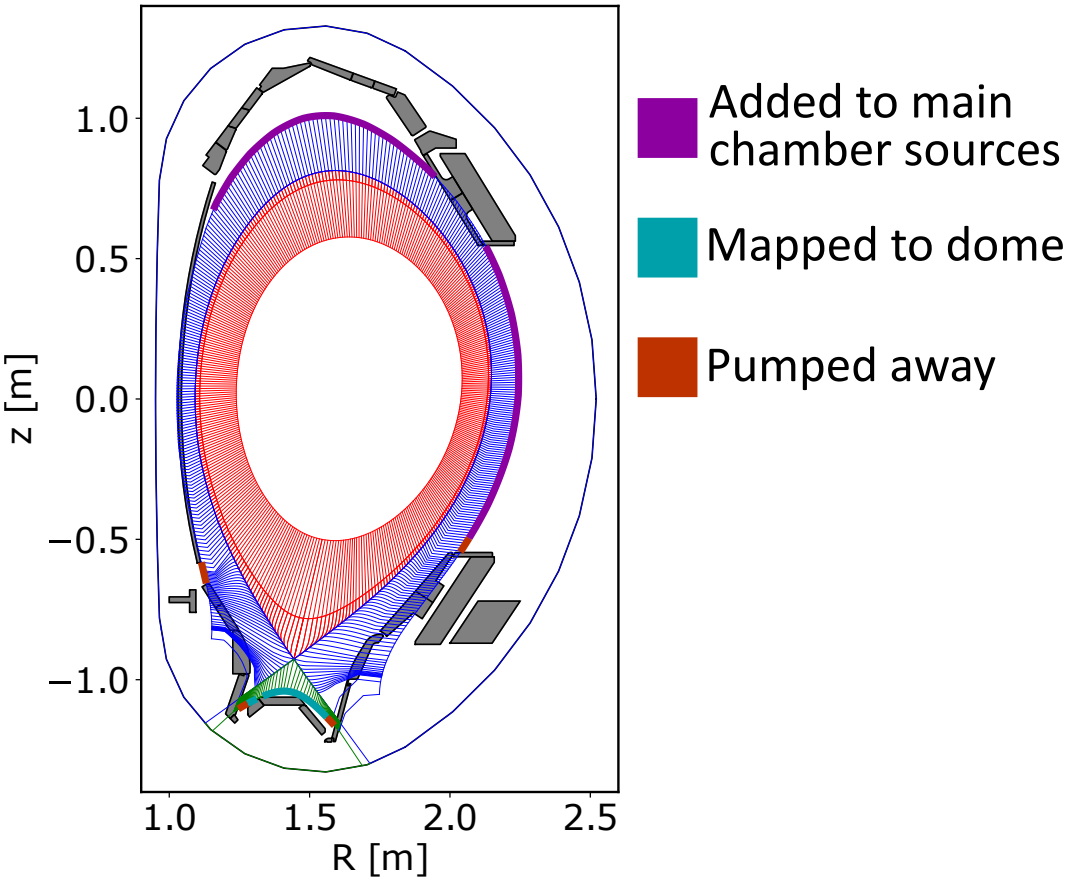

Figure 4.7: Schematics of the matrix normalisation via the adapted normalisation.

Chapter 5

Modeling results

This chapter presents plasma backgrounds that were simulated with EMC3-EIRENE based on the discharges presented in section 3.5 and shows the influence of geometrical features on obtained simulation results. 3D WallDYN calculations based on these plasma backgrounds are then compared to the post discharge surface analysis of the ^{15}N areal densities. The majority of the content of section 5.1 was already published in [69].

5.1 Plasma background simulations of #32024 with EMC3-EIRENE

In section 3.5.1 the ASDEX Upgrade discharge #32024 was described. This section will discuss the simulations conducted to reproduce the plasma background of that discharge and present investigations of geometrical influences on plasma parameters. The simulations aim to reproduce the plasma parameters during the green shaded time span around $t = 3.0\,\mathrm{s}$ in figure 3.5. At that timepoint the discharge is in L-mode and the plasma parameters are very stable.
Input values for the EMC3-EIRENE simulation are taken from the average of the experimental data from $t = 2.95\,\mathrm{s}$ to $3.05\,\mathrm{s}$, resulting in a separatrix density of $n_{e,sep} \approx 0.74 \cdot 10^{19}\mathrm{m}^{-3}$ and electron temperature of $T_{e,sep} \approx 57\,\mathrm{eV}$. The total heating power was $P_{heat,tot} \approx 0.99\,\mathrm{MW}$, consisting of the ECR heating power and the Ohmic heating from the plasma current, while $P_{rad,tot} \approx 0.67\,\mathrm{MW}$ was the radiated power from the plasma at the same time.
The simulations focus on the scrape-off layer and the simulation volume for the plasma is radially limited to a normalized plasma radius of $\rho \geq 0.98$. The effective heating power and radiated power in the simulated volume was estimated by tomographic reconstruction leading to a radiated power of $P_{rad} = 0.4\,\mathrm{MW}$ outside the simulated volume in the region of $\rho < 0.98$. Thus the effective heating power in the simulated region is reduced to $P_{heat,eff} \approx 0.59\,\mathrm{MW}$ and the radiated power reduces to $P_{rad,eff} \approx 0.27\,\mathrm{MW}$. In the simulation this has

to be radiated by the nitrogen impurity and the deuterium.
In presented simulations the nitrogen impurity is seeded from wall tiles proportionally to the main plasma ion influx, mimicking the recycling of ^{15}N at the wall. The seeded amount is then scaled such that the simulated total radiated power matches the bolometric measurements. The simulation volume is radially confined by the plasma core in the center and the vessel wall radially outwards. All plasma facing components are treated equally and impinging plasma ions are re-emitted as fast atoms or thermal molecules (see pages 96 ff. and 149 ff. in [61]), mimicking the recombination of plasma ions at surfaces. The core boundary acts as an energy source and the surface-average flux of impurities reaching the core boundary is set to zero, i.e. the impurities reaching the core are re-emitted from another poloidal position back into the SOL. The energy from the core is equally split between the electron and ion channel and is given by the effective external heating sources. To maintain the particle balance the recycling flux is scaled such that the the separatrix density is equal to the experimentally determined value. An additional particle sink by pumping is accounted for by a surface with an albedo of 0.88 that is located behind the outer divertor.
The impurity distribution is calculated with the force balance from equation 2.16 and then scaled to match the radiated power determined with tomography from the experiment.
The magnetic equilibrium reconstruction was used to generate a 3D field-aligned simulation grid. A poloidal cross section of the grid is shown in figure 5.1. The 3D grid is structured into three zones. The red colored core grid, the blue colored scrape-off-layer and the green private flux region. The region of thinner lines shows the extended grid regions for neutrals, while thick lines represent the plasma grid. Additionally, grey represents heat-shield elements in ASDEX Upgrade and on the low field side the outlines of a poloidal rib limiter is indicated. The oval shaped black line surrounding the grid outlines the vacuum vessel. Two arrows point to the positions of the inner and outer bypass, where neutral particles from behind the divertor structure can enter the plasma.
The equilibrium reconstruction can generate 3D grids with a maximal extend of 30 ° in toroidal direction. To extend the simulation domain to cover 60 ° and hence include the mid-plane collector probe as well as the two nearest rib limiters in the vicinity of the probe, two grid segments with mapping boundary conditions in toroidal direction were used.

5.1.1 The influence of wall geometry on plasma parameters

Simulations of plasma backgrounds for tokamak plasmas generally aim to match experimental data upstream at the mid-plane and downstream at the divertor target plates. For the 2D version of WallDYN the re-distribution matrix

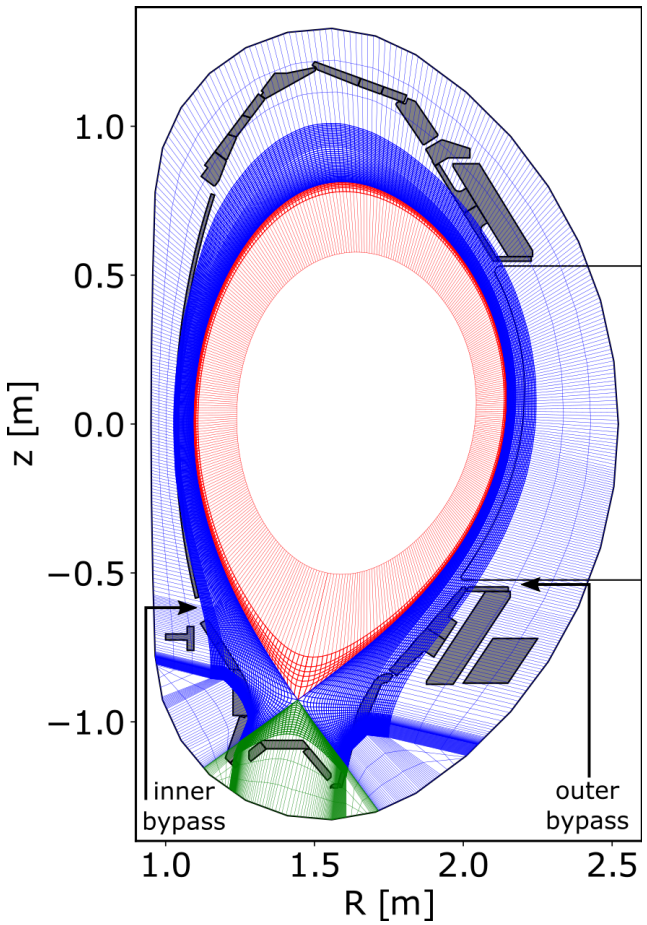

Figure 5.1: Poloidal cross section of the 3D grid based on the magnetic configuration for discharge #32024. The private flux region is colored in green, the core is shown in red and the scrape-off-layer is depicted in blue.

is calculated from a SOLPS [67] background which applies a more elaborate physics model than EMC3, but can only deal with 2D geometries and thus assumes toroidal symmetry. This symmetry is essentially fulfilled in the divertor region of tokamaks, but the main chamber often includes features like poloidal limiters and probes that break the symmetry.
For impurity migration studies it is important to understand the plasma flow pattern at these localized elements, that break the toroidal symmetry upstream, as they can have an influence on the re-distribution of impurities (see friction force in equation 2.16).

5.1.2 Wall geometries

To investigate the influence of the 3D geometry on simulated plasma solutions, two versions of the wall geometry were implemented. One version that includes two rib limiters and the mid-plane collector probe on the LFS, effec-

tively breaking the symmetry on the LFS, while the divertor and HFS geometries are toroidally symmetric. That wall geometry is shown in figure 5.2 and resembles 60 ° of the geometry during the discharge #32024 with a blue line as an indicator for the toroidal angle of 24.5 °, where analysis of plasma parameters was conducted in section 5.1.4. The rib limiters are located at $\phi = 4.5\,^\circ$ and 52.5 ° and the MEM is located at 44.5°. The curly braces indicate areas that were used for recycling analysis in section 5.1.4.
The collector probe in this geometry is protruding about 2.5 cm out of the limiter shadows into the SOL plasma with its tip being at the radius of $R = 2.156\,\mathrm{m}$. The apex of the rib limiters is at $R = 2.181\,\mathrm{m}$ at the median z position of the collector probe of $z = 0.31\,\mathrm{m}$. Because the grid and the geometry are essentially duplicated six times to calculate the full circumference of the torus, the presented geometry is effectively seen by the plasma as consisting of twelve rib limiters and six mid-plane collector probes. The real machine geometry features only a single mid-plane deposition probe and while several rib limiters are installed, they are not placed in the six fold symmetry as in the simulation setup. This geometry and the associated plasma background simulations are referred to as 3D simulations.

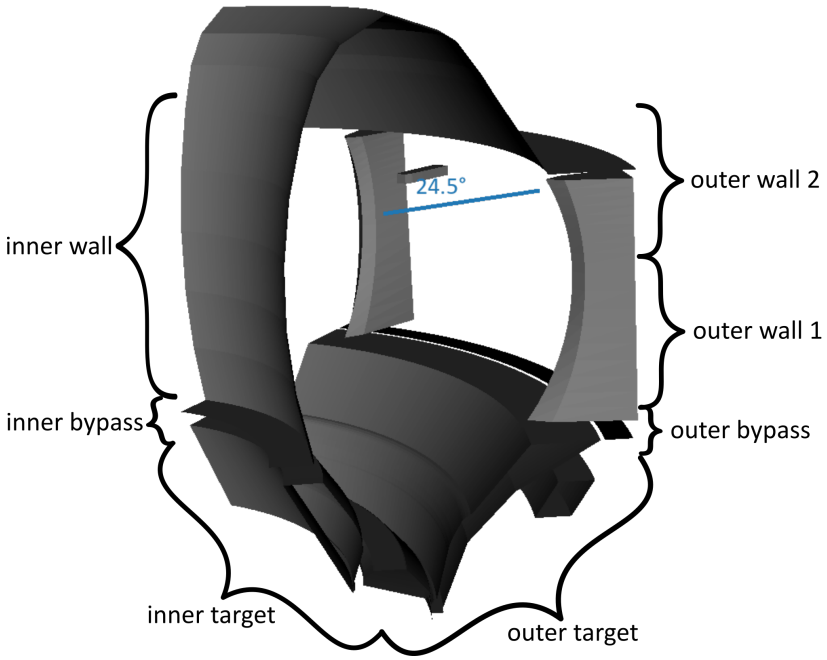

Figure 5.2: 60 ° wall geometry as seen by the neutral particles in the 3D geometry. The blue line indicates the toroidal position $\phi = 24.5\,^\circ$ where analysis of the plasma parameters was conducted. The rib limiters are located at $\phi = 4.5\,^\circ$ and 52.5 °, the MEM is located at 44.5° and the curly braces indicate the regions mentioned in the recycling analysis in section 5.1.4.

The second version of the wall geometry is referred to as 2D geometry and features a closed wall following the apex of the rib limiters in the 3D geometry.

This wall geometry would be seen by charged particles in pure 2D simulations and is shown in figure 5.3. The curly braces indicate areas where recycling was compared in both geometries in section 5.1.3 and the blue line at 24.5° indicates, where plasma parameters were compared in both geometries.

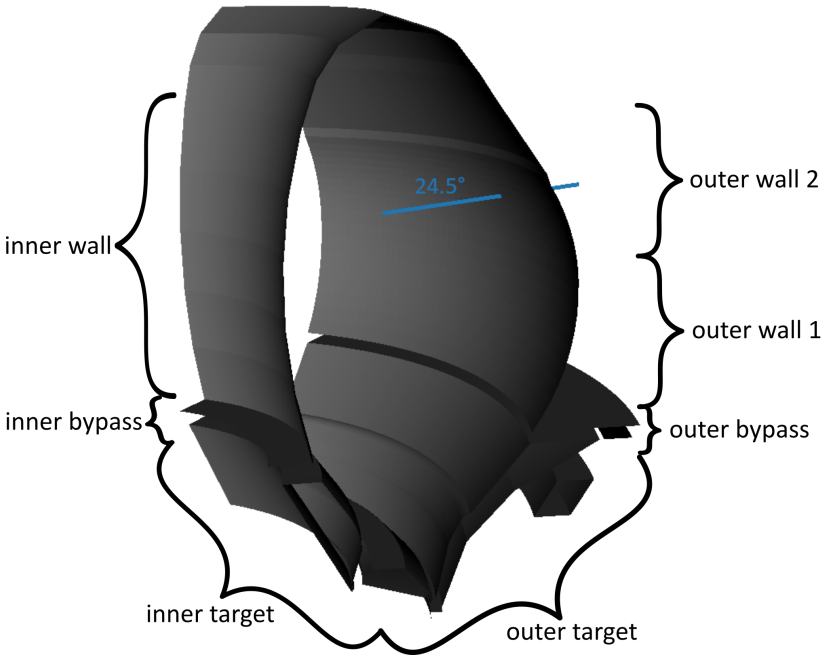

Figure 5.3: 60° wall geometry as seen by the neutral particles in the 2D geometry with the same indicators as in figure 5.2.

5.1.3 Comparison of plasma background solutions

Simulations were conducted with identical input parameters in both geometries. Apart from the experimentally determined input parameters, the perpendicular transport coefficients $\eta_\perp$ and $D_\perp$ in equations 4.1 and 4.2 have to be set. These transport coefficients are varied until a reasonable agreement between simulated profiles and experimental profiles is achieved, while experimentally given input parameters are usually only slightly varied or kept constant in-between iterations.
The simulated profiles for both geometries are compared to experimental data upstream at the outer mid-plane in figure 5.4. The solid green and blue dashed lines represent the simulated profiles from the 3D and 2D simulations, respectively.
The electron temperature T_e was measured with the lithium-beam and the edge Thomson scattering diagnostics, which provides additional data for the electron density n_e. Edge profiles in ASDEX Upgrade are routinely shifted to match characteristic values at the separatrix, as both the magnetic equilibrium reconstruction and the Thomson diagnostic have radial uncertainties that can

sum up to 1.5 cm in some cases [42].
For this analysis, the data from the Thomson scattering diagnostics is shifted by 9 mm to match a separatrix temperature of $T_e = 50 - 60$ eV, which is characteristic for L-mode discharges in ASDEX Upgrade [70, 71]. The same shift was applied to the Thomson density data. The data obtained from the lithium-beam diagnostic was shifted by -3 mm to match the Thomson data at the separatrix.
In figure 5.4 a) the simulated electron densities are compared to experimental data. Additionally the perpendicular transport coefficient is plotted with a dotted blue line. Both simulated profiles agree reasonably well with the experimental data from the lithium beam and only show a slight difference around $\rho = 1.01$. For the electron temperature in figure 5.4 b) and the ion temperature in c) the simulated profiles again overlap almost completely over the whole radial domain. While the match to the experimental electron temperature could be verified, the CXRS measurements did not provide reliable ion temperatures at the simulated radial positions.

Downstream at the divertor target plates the simulated profiles of both simulations were compared to electron temperature and ion saturation current obtained from Langmuir probes and the simulated heat flux to the target is plotted against the heat flux as obtained from infrared thermography, which is depicted in figure 5.5. The 3D simulation data is plotted with solid lines and the 2D case with dashed lines. Simulated as well as experimental data at the inner and outer target is colored in red blue, respectively.
Figure 5.5 a) shows a good agreement between experimental and simulated values for the ion saturation current. Small discrepancies between the simulation cases are present around $\rho = 1.01$ for the outer target, where the simulated profiles underestimate the profile width suggested by experimental data. At the inner target the experimental data even suggest a different profile shape, which is also visible in the comparison of electron temperatures at the inner target in 5.5 b).
The electron temperatures at the target are slightly smaller (about 3 eV) in the 2D case at both target plates radially outwards, even though the peak temperature at the inner target is about 1 eV higher than in the 3D case. The profile shapes are very similar for both simulation cases with the 2D simulated profile being slightly more peaked at the inner target. While both simulation profiles agree reasonably well with the shape of the experimental data at the outer divertor, the profiles at the inner target are far off and the experiment suggests a far larger asymmetry, which is only visible in the simulated heat flux for inner and outer target. The outer divertor target in ASDEX Upgrade usually experiences higher heat fluxes and hence has a larger influence on the profiles at the outer mid-plane.

Matching simulation profiles with experimental data at the inner and the outer divertor proves very difficult even in simulations that include plasma drifts and currents in the divertor plasma [72, 73], which drive these experimentally

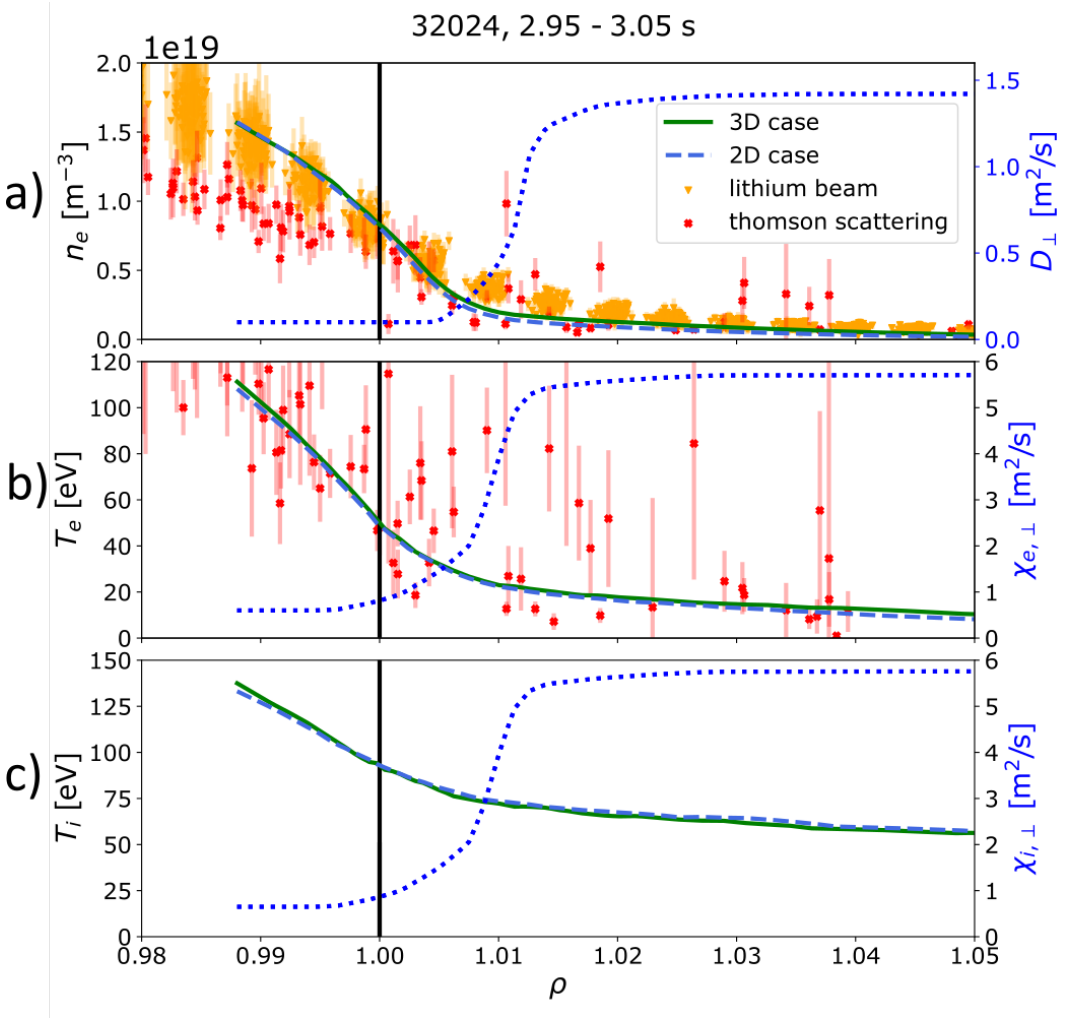

Figure 5.4: Comparison of 3D and 2D simulation results with experimental data upstream at the outer mid-plane. a) electron density, b) electron temperature, c) ion temperature.

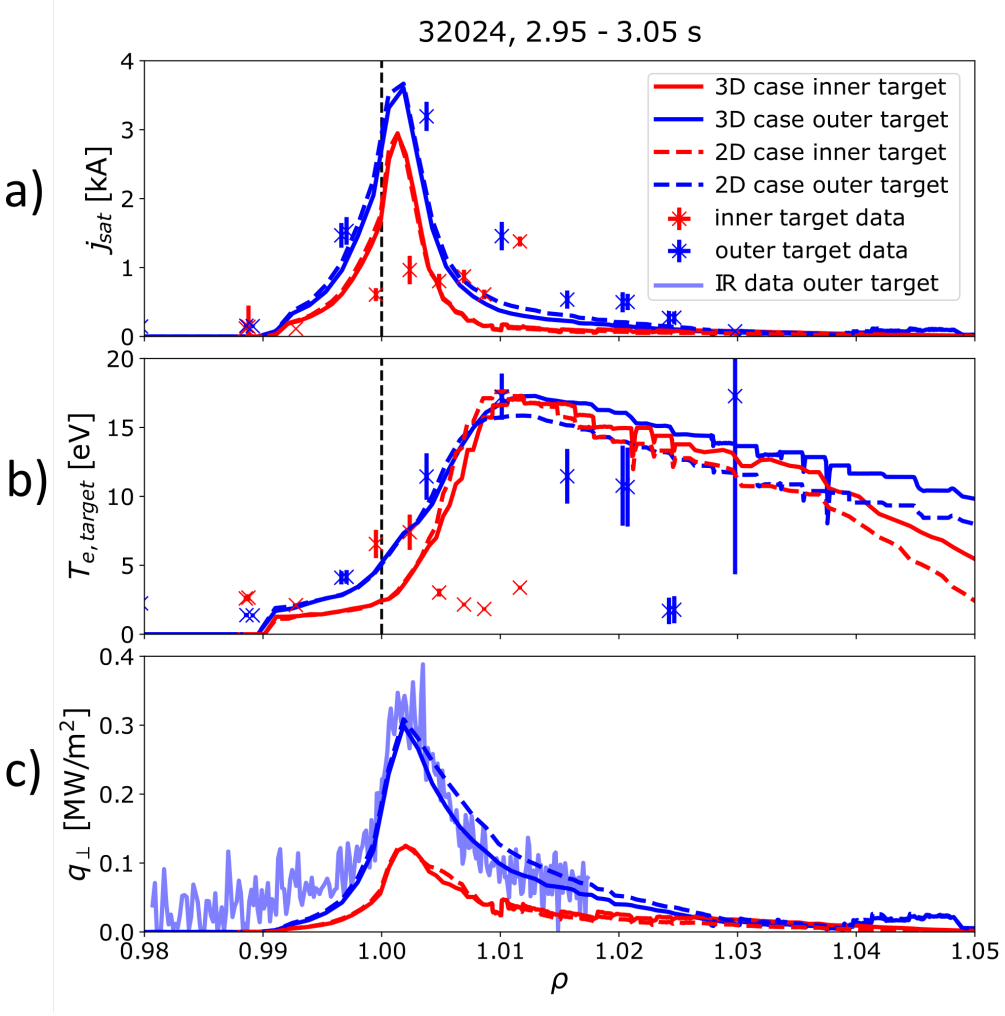

Figure 5.5: Comparison of both 3D and 2D simulation results with experimental data downstream at the divertor target. a) Ion saturation current : experimental data from Langmuir probes. b) Plasma temperature at the divertor target, c) Heat flux perpendicular to the divertor target : experimental data from an infrared camera.

observed asymmetries. Because EMC3-EIRENE does not yet include these effects and the research interest mainly focuses on properties at the outer divertor and the outer mid-plane, the match of experimental and simulated data at the outer target was prioritized and the missing asymmetry, i.e. the missing match at the inner target, in ion saturation current and electron temperature is accepted.

In the comparison of experimental and simulated heat flux density profiles in figure 5.5 c) the 2D and 3D simulated data have slightly different shapes, but agree well with the experimental data, that was shifted by $-0.05\,\mathrm{MW/m^2}$ due to a strong background.

The comparison of simulated upstream and downstream profiles yields only minor differences in the plasma parameters between the 3D and 2D simulation setups.

5.1.4 Comparison of background flows and particle sources

With the focus of this thesis being on impurity migration, plasma flows were analysed in poloidal cross sections at several toroidal angles. Plasma flows are given in terms of the Mach number

$$M = \frac{v_i}{c_s} = \frac{v_i}{\sqrt{\frac{T_e+T_i}{m_i}}}, \tag{5.1}$$

which is the ratio of the ion fluid velocity and the plasma sound speed. Large differences in the Mach patterns between the 3D and the 2D geometries were observed.
A poloidal cross section of the plasma flow at the toroidal angle of $\phi = 24.5\,^\circ$, which is indicated in figures 5.2 and 5.3, can be seen in figure 5.6 a). The sign of the Mach number indicates whether particles flow in toroidal direction or against the toroidal direction. With the field line angle this direction indicates whether the plasma flows towards the inner or outer target plate. The flow patterns in 2D and 3D geometries differ at $\phi = 24.5\,^\circ$, far away from the local influence of the rib limiters or the mid-plane collector probe. A pronounced plasma flow in toroidal direction can be directly associated with the mid-plane collector probe that is located at a toroidal angle of $44.5\,^\circ$, $20\,^\circ$ away from the plotted cross-section. The stream is highlighted by the black arrow in the right hand side picture.
In 2D geometry the area of flow reversal, i.e. the read area with $M < 0$, where the flow is directed towards the inner target instead of the outer one, is very symmetric at the top of the chamber, while in 3D geometry this area is located at the outer mid-plane. The areas are indicated by the black dashed line.
As the plasma flow is governed by particle sources, the ionisation sources were compared in both geometries in figure 5.6 b). While the ionisation source distribution is very similar on the HFS, large differences are visible at the LFS. Compared to the results in 2D geometry, the region of strong ionisation sources reaches far more poloidally upwards in 3D geometry. The distribution in 2D geometry, however, exhibits a strong ionisation source close to the outer bypass (see figures 5.2 and 5.3), that is not visible in the distribution in 3D geometry. To understand the distribution of ionisation sources it is necessary to have a look at the neutral particle distribution, depicted in figure 5.6 c). While the distribution on the HFS is essentially identical there are notable differences on the LFS, similarly as already observed for the distribution of ionisation sources. The pronounced region of a higher ionisation source at the outer bypass correlates with a region of higher neutral density in the 2D case, again indicated by a rectangle. This can be explained by neutral particles from behind the divertor structure, that enter the plasma through the outer bypass. They cannot move further upwards outside the plasma because of the fully

closed wall in the 2D geometry. In the 3D geometry, this hindrance only occurs at toroidal positions where rib limiters are present. Between the limiters, however, particles can move poloidally upwards, resulting in a reservoir of neutral particles as visible on the LFS in figure 5.6 c). Particles from this reservoir can enter the plasma at much larger poloidal angles compared to the 2D geometry, explaining both the differences in neutral density and ionisation source distribution, that drives the plasma flow.

The differences in ionisation source and neutral density become even more evident when the quantities are integrated over the toroidal and the radial indices in the SOL and at identical poloidal indices. The resulting curves are plotted for the toroidal angle from 30 to 60 ° in figure 5.7 for both geometries. Comparing the ionisation sources shows the peak at the poloidal indices around the outer bypass in 2D geometry, where in 3D geometry a local minimum is located. In 3D geometry the ionisation sources then increase quickly and slowly decrease again up to the position of the mid-plane collector probe, where another clear peak can be identified. This behaviour can be explained after looking at the implemented 3D wall geometry in figure 5.2.

Particles that enter the outer bypass region from behind the divertor structure must pass through a small gap that acts like a line source for neutral particles. Particles that went through the gap, must have a certain momentum poloidally upwards, resulting in less ionisation sources directly at the bypass position and larger contribution poloidally upwards up to the poloidal position of the MEM, where neutral particles are scattered or recycled. On the HFS, where the heat shield geometry is identical in both geometries, the integrated ionisation sources are very similar.

Similarly, the integrated curves of the neutral density differ much more on the LFS than on the HFS. Around the outer bypass a local maximum can be seen in both geometries. While in the 2D geometry these particles can only enter the plasma around these indices, resulting in the peak in ionisation sources, the reservoir of neutral particles can clearly be seen in poloidal indices from 150 to 250 in the 3D geometry. The slight peak around the MEM position can be attributed to neutral particles that are scattered and recycled at the probe. These recycled particles and particles recycled at the rib limiters contribute to the accumulation of neutral particles between the limiters and can have an influence on the observed neutral particle distributions and ionisation sources. To clarify these contributions, the recycling sources in both geometries were investigated in more detail.

To that end the poloidal distribution of recycling sources in both simulations was analysed in figure 5.8. The area labels on the x-axis are indicated in figures 5.2 and 5.3 and the total number of recycled particles is indicated in the top right corner. In both geometries the majority of particles are recycled in the divertor. Outside the divertor more particles are recycled in the region around the outer bypass in 2D geometry, while in all other areas the recycling sources are slightly larger in 3D geometry.

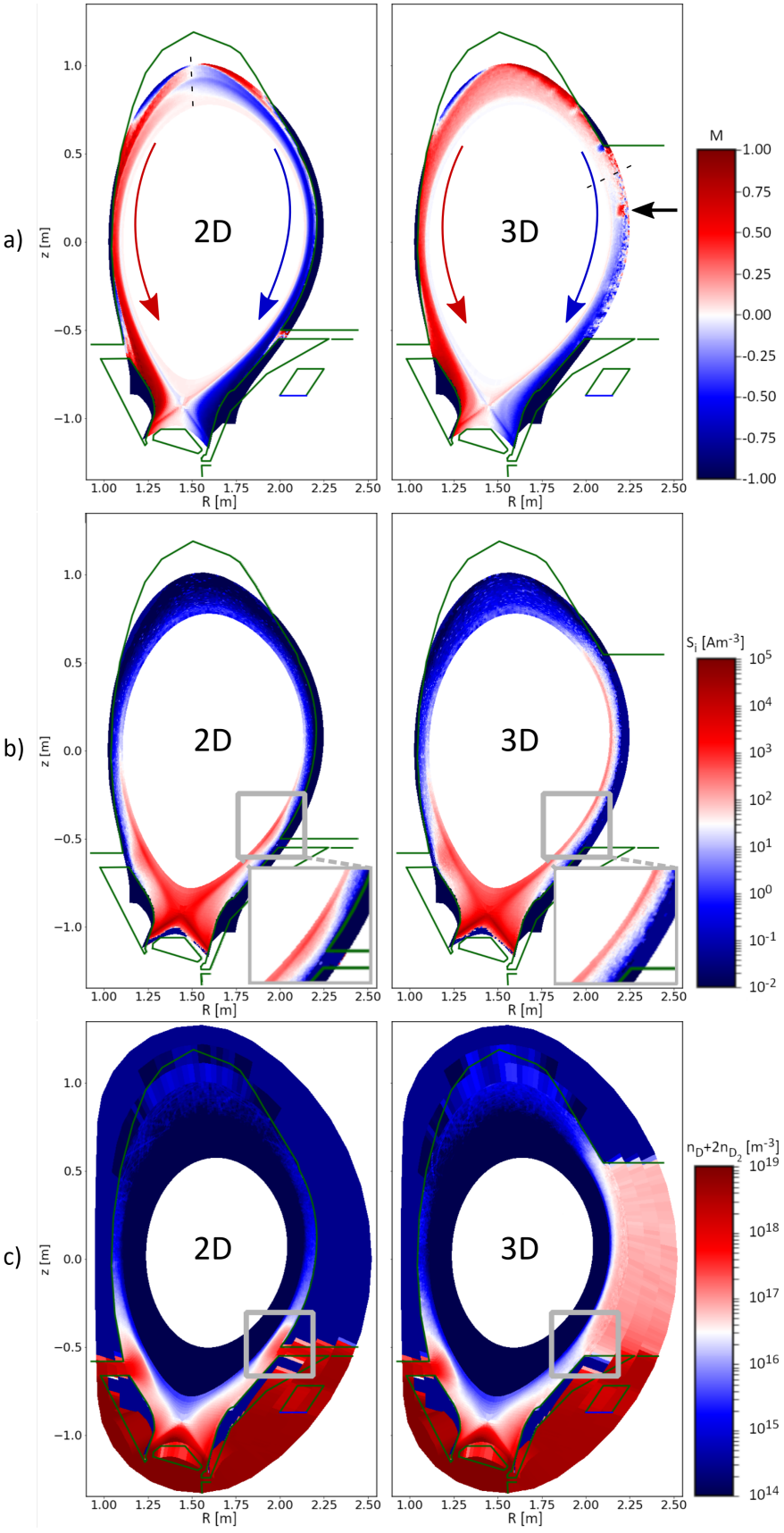

Figure 5.6: Comparison of data in the poloidal cross sections from simulations in 2D (left) and 3D (right) geometry at $\varphi = 24.5\,°$. a) Plasma flow pattern as indicated by the Mach number. b) Ionization source distribution. Indicated and enlarged by the grey rectangles is the outer bypass region. c) Distribution of the neutral density. The same region as in b) is indicated by the grey rectangle.

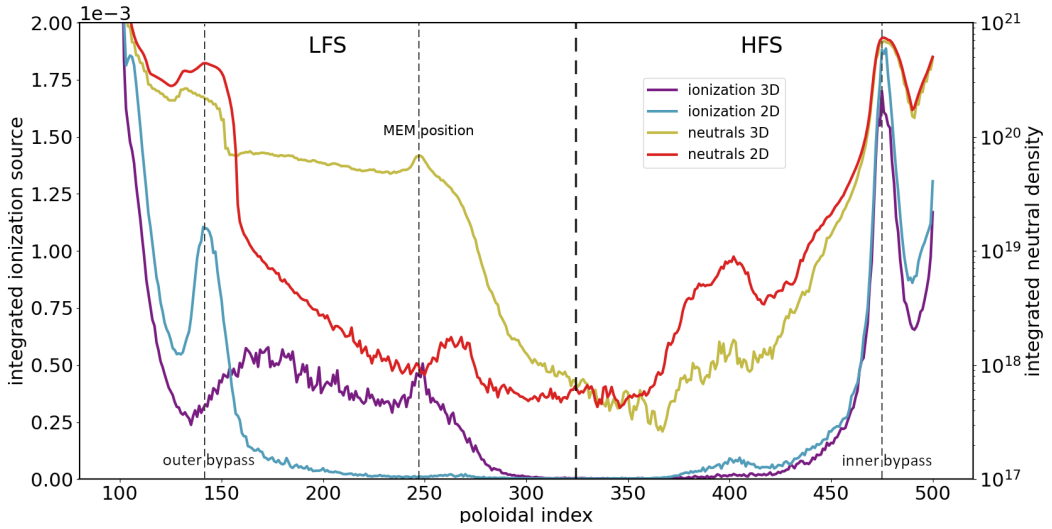

Figure 5.7: Integrated 2D and 3D ionization source and neutral density distributions along the poloidal index outside of the divertor, region from 30° to 60°. Note that the ionization is plotted linearly, while the neutral density is plotted logarithmically.

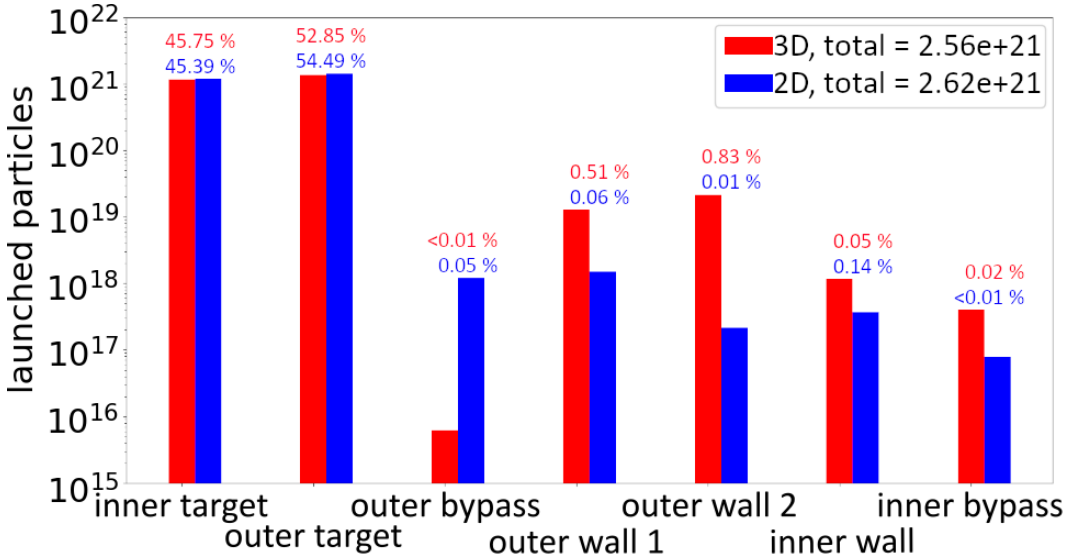

Figure 5.8: Neutral particles launched from different areas as a result of recycling in 2D and in 3D geometry. The fractions indicate the launched particles of an area divided by the total number of launched neutral particles from recycling. Wall areas are indicated in figures 5.2 and 5.3.

In a next step the simulations were conducted again with modified recycling sources. To investigate the influence of main chamber sources on the observed distributions, the launch of recycled particles was limited to the regions inner and outer target, i.e. the divertor. The then obtained distributions were again integrated radially and toroidally and compared to the curves from the previous simulations, where all recycling sources were allowed. Figure 5.9 shows the comparison of the neutral density. In 3D geometry the curves are very similar in the whole main chamber, revealing that even the peak around the MEM position mainly stems from neutral particles from the divertor that moved poloidally upwards and were scattered at the probe. Even though the curves in 2D geometry are also quite close, pronounced areas around the poloidal indices of 260 and 400 disappeared, when the main chamber recycling sources are switched off. Thus those peaks were contributed by recycling at leading edges in the main chamber geometry.

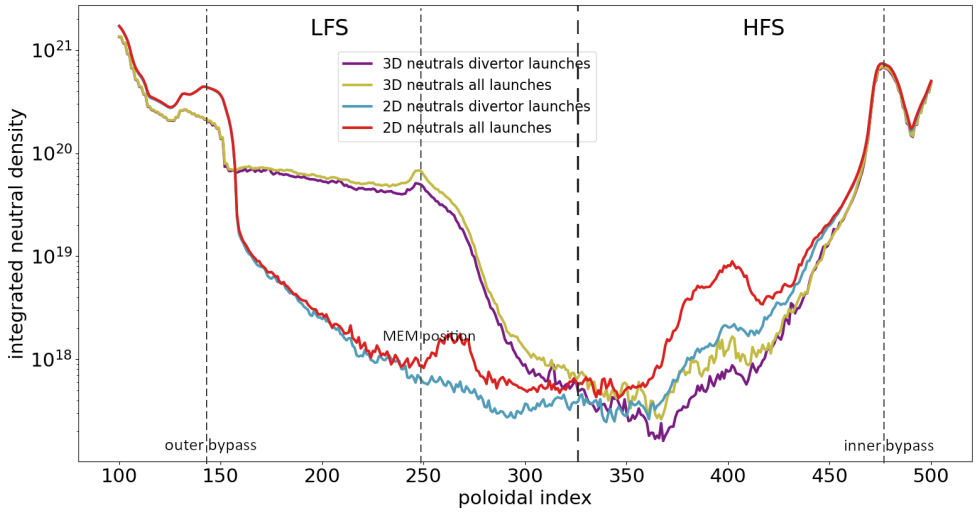

Figure 5.9: 2D and 3D neutral density (sum of atom and molecular neutral density) distribution along the poloidal index, integrated over the radial and toroidal indices in the SOL, outside of the divertor region, from 30° to 60°.

Looking at the distribution of ionisation sources in figure 5.10 reveals that also the ionisation sources in the main chamber are predominantly fueled by neutral particles that were recycled in the divertor. In 2D geometry the small bump around the poloidal index of 400 disappeared, which can be related to the missing peak in neutral particles when main chamber recycling sources are switched off.
Thus the recycling analysis reveals that the differences in neutral density, ionisation source distribution and plasma flow are driven by the differences in neutral particle transport paths from the divertor to the main chamber and not by differences in recycling in the main chamber due to different geometries at the LFS. To accurately interpret impurity migration experiments with 3D codes it is therefore required to implemented an appropriate 3D geometry for

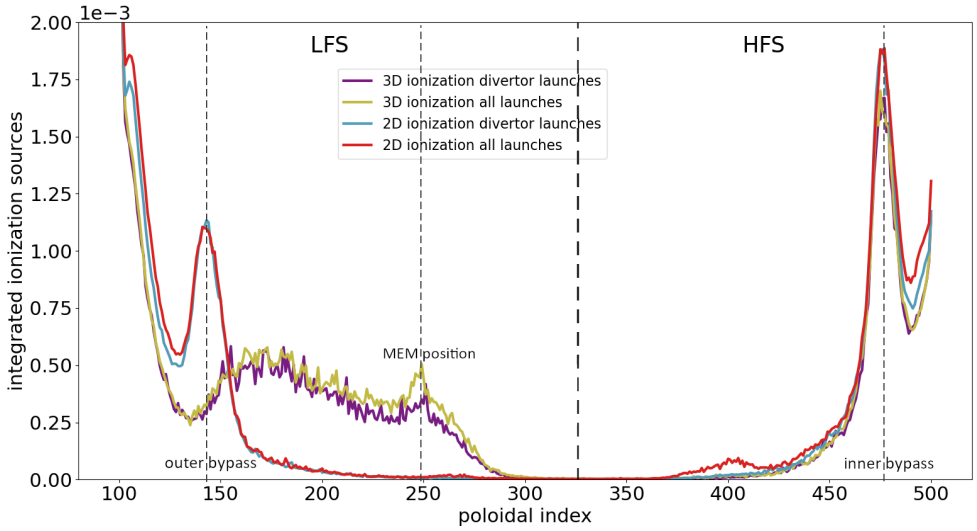

Figure 5.10: 2D and 3D ionization source distributions along the poloidal index, integrated over the radial and toroidal indices in the SOL from 30° to 60°.

the neutrals. The good match of the plasma data for both geometries in contrast to the poor match of the neutral distribution suggests that commonly used plasma parameters like T_e, T_i and n_e can accurately be obtained with a 2D symmetric wall following the apex of the limiters, whereas the neutral distribution and hence the resulting plasma flows in the SOL are depended on the full 3D geometry.

5.2 3D WallDYN simulations for #32024

The main motivation to investigate impurity migration with 3D codes is linked to observed mismatches between experimentally obtained values of ^{15}N deposition at the mid-plane and predicted values from 2D simulations in [12], where the deposition was calculated assuming an effective deposition based on a particle flux extrapolated from background plasma parameters, an effective net deposition factor based on SDTrimSP calculations and the exposure time. These assumption could not cover the dynamic interaction of fluxes from the deposition probe with other wall elements in 3D, even if the extrapolated ^{15}N flux to the mid-plane collector probe is in the right order of magnitude [69].
To setup the 3D WallDYN simulation, the geometry in figure 5.2 was discretised into 1312 wall tiles. The area on top of the chamber, that does not intersect the plasma grid, has been omitted and particles leaving the grid at that position are taken into account by the normalisation of the re-distribution matrix (see section 4.3.4).
The re-distribution matrix was calculated with the kinetic impurity model (see equation 4.10) based on the plasma background in 3D geometry from section 5.1 and consisted of 1312 reduced EMC3-EIRENE simulations for each im-

purity. In contrast to plasma background simulations with EMC3-EIRENE these reduced simulations consist only of running the impurity and the post-processing module. They were used to simulate the deposition of impurities launched from a point source at each wall tile. For each of these source tiles, the deposition on every destination wall tile is expressed by the fraction of deposited particles by launched particles in the re-distribution matrix.
To compare the migration in 3D to previous 2D migration results, the obtained 3D re-distribution matrix for ^{15}N was mapped to the 2D geometry that was used in [12] for 2D WallDYN simulations, by projecting the 3D geometry into 2D and finding the closest wall tile in the 2D geometry.
In figure 5.11 the closed 2D wall geometry is colored in red and the wall tile number is indicated. In blue the projected 3D geometry is indicated. The wall tiles in 2D are associated to the following labels:

- HFS wall: tiles 0–8
- top section of the wall: tiles 8–11
- LFS wall (rib limiters and collector probe in 3D): tiles 11–18
- outer target: tiles 18–39
- dome structure: tiles 39–48
- inner target: tiles 48–59.

Figure 5.12 compares the re-distribution matrix for ^{15}N from an EMC3 simulation, projected into the 2D geometry, with the 2D re-distribution matrix calculated with the impurity transport code DIVIMP [68] on a SOLPS background, showing that the re-distribution follows a similar pattern in both geometries. The white horizontal and vertical bars in the re-distribution matrices correspond to gaps in the 3D geometry: The top of the chamber at tiles 8 to 10 and the pumping ducts in the divertor around the tiles 40 and 48.
In the 3D matrix, more particles are transported from source tiles 0 to 25 to the destination tiles 24 to 30 in comparison to the 2D matrix. This means that more particles from the main chamber and parts of the outer target end up at the outer target in the 3D geometry. In the 2D re-distribution matrix more particles from tiles 0 to 10 end up at tiles 10 to 20, meaning that more particles from the HFS wall and the chambers top are transported to the LFS wall. Still, both matrices exhibit quite similar features and observed differences can be attributed to differences in the simulated geometry and especially the different plasma backgrounds.
A suspected reason for the mismatch between experimentally obtained ^{15}N deposition data at the mid-plane collection probe and predicted results by 2D WallDYN simulations in [12] is the neglected influence of the 3D geometry. In [69] it was demonstrated that the 3D geometry on the LFS yields

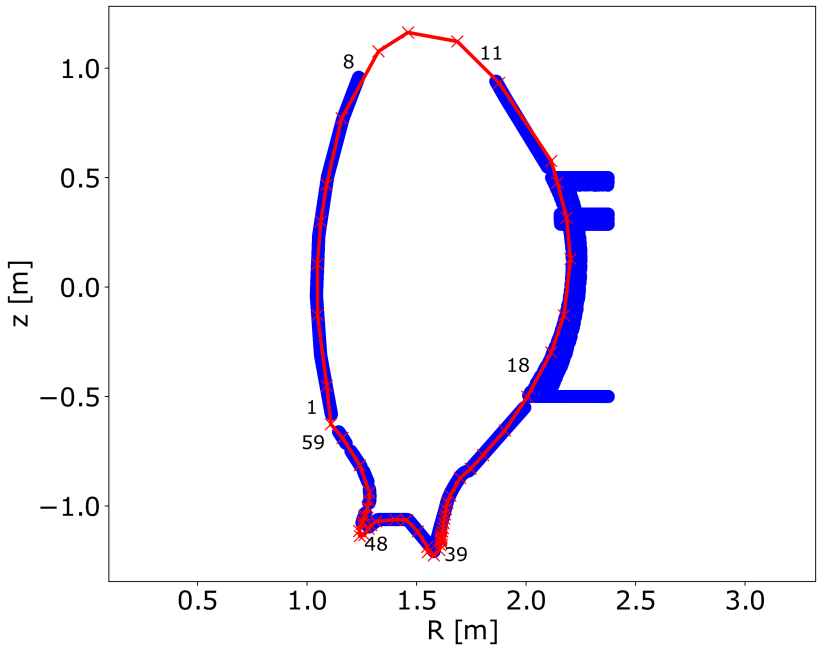

Figure 5.11: Discretised wall in 2D WallDYN simulations in [12] depicted in red with annotations for the index of some discretised wall tiles. The projection of the 3D geometry from figure 5.2 is depicted in blue.

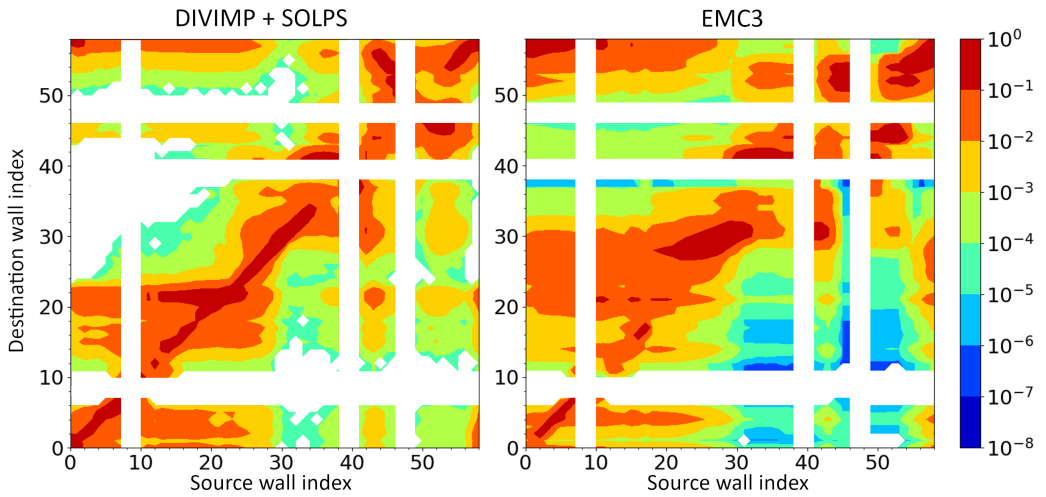

Figure 5.12: Comparison of 2D re-distribution matrix for ^{15}N as calculated by DIVIMP on a SOLPS background and the 3D re-distribution from EMC3 projected onto the same 2D geometry (see figure 5.11).

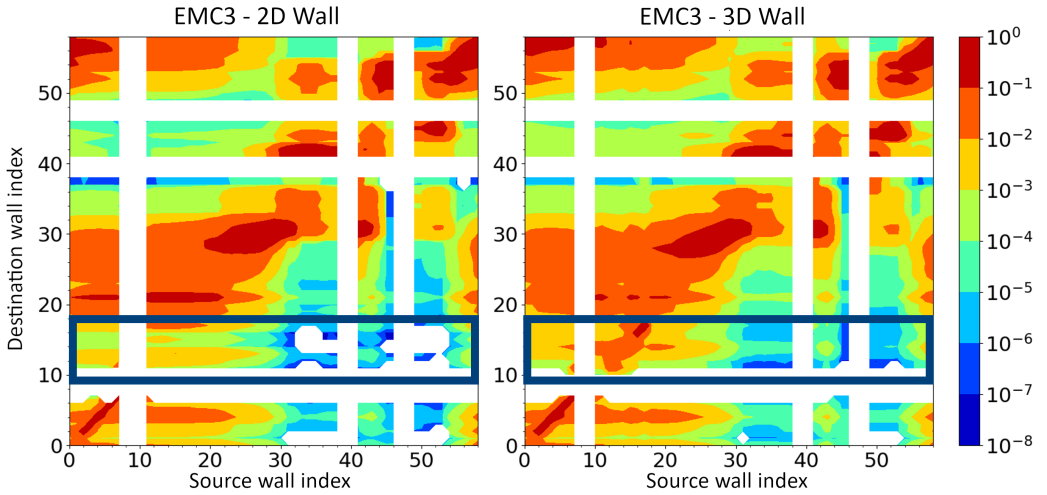

Figure 5.13: Comparison of 3D re-distribution matrices for ^{15}N from EMC3 with toroidally symmetric wall (see figure 5.3) and 3D wall (see figure 5.2) projected onto the 2D geometry from [12]. The rectangle highlights the most important difference.

different plasma flow patterns than a closed, toroidally symmetric wall geometry, when simulating plasma backgrounds with EMC3-EIRENE. On the other hand, plasma density and temperature do not change significantly at the simulated LFS mid-plane collector probe. To investigate whether the observed changes in plasma flow patterns are strongly pronounced in the re-distribution matrices, a 3D WallDYN simulation was set up in the toroidally symmetric wall of figure 5.3 including 1342 wall tiles. For consistency, the then calculated re-distribution matrix of ^{15}N is also projected onto the 2D geometry (figure 5.11), and is compared to the projected re-distribution matrix of the full 3D geometry in figure 5.13. While both matrices are very similar, a closer look at the destination tiles 10 to 18, highlighted by the rectangle, reveals that significantly more particles are deposited at the LFS wall elements in 3D geometry than in 2D geometry, when the re-distribution of ^{15}N is calculated in the respective background plasmas.

To include the mid-plane collector probe in the re-distribution calculations, the actual 3D WallDYN run was set up in the 3D geometry and the re-distribution matrices for ^{15}N and ^{184}W were calculated with the plasma background from the 3D geometry. The impact angle of incoming particles was set to 48° at every of the 1312 wall tiles, which has been shown to be the average impact angles for a rough surface [74]. The reaction zone width was fixed at $dx = 10\,\text{Å}$, where the WallDYN surface model agreed best with SDTrimSP simulations.

To have temperature values at the dome, which is not intersecting with the plasma grid, values of the closest plasma grid cell are taken, similarly to the method that takes particles lost above the dome into account as briefly described in section 4.3.4. To save computational resources the maximal charge state of tungsten was limited to 20, while for nitrogen all 7 charge states were

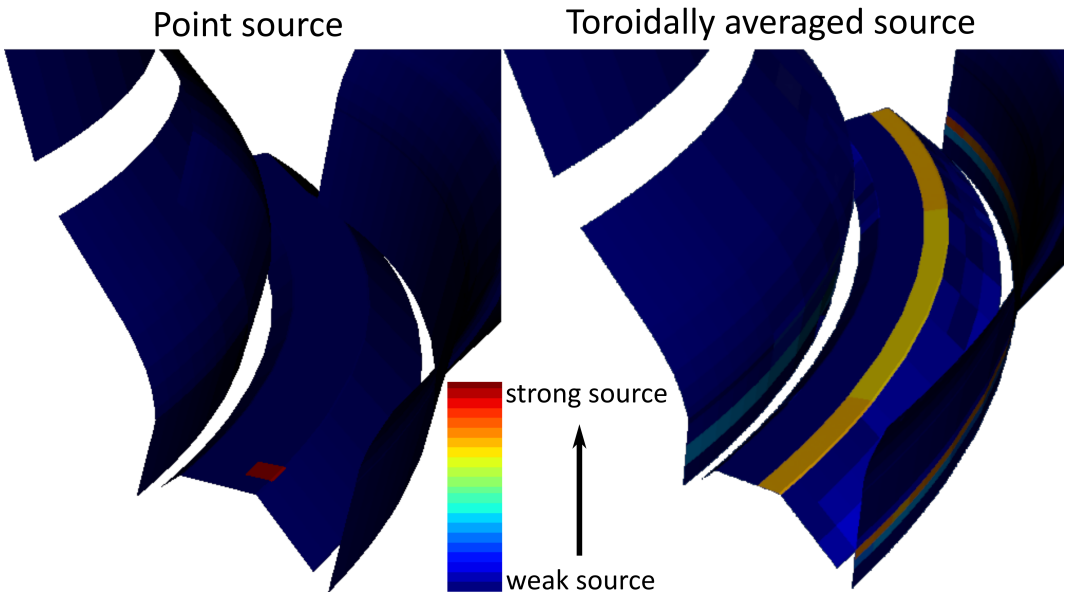

Figure 5.14: Calculated ^{15}N sources from WallDYN in units of flux density at the first time step. The point source is represented by a single wall tile that seeds all ^{15}N, while in the toroidally averaged source, the total seeding is averaged over tiles in the toroidal direction.

allowed. The maximum concentration of ^{15}N in the reaction zone is capped at $c_{\max} = 0.3$ resulting in a reflection yield of 1 for concentrations above $c = 0.3$ (see section 4.3.2).
In the experiment, the average seeding rate in the discharge #32024 was $\Gamma_{\text{seed,total}} = 2.9 \cdot 10^{20}$ ^{15}N/s, seeded from two valves in the divertor. In WallDYN only 60 ° of the geometry is simulated and setting the seeding strength of a point source in this segment to $\Gamma_{\text{seed,tile}} = \Gamma_{\text{seed,total}}/2$ could lead to an overestimation of the deposited ^{15}N, because the actual geometry would then consist of 6 sources and hence to 3 times more seeding than in the experiment. Therefore different seeding configurations were compared in the simulation:
In one variation the point source, represented by a single wall tile, has a seeding rate of $\Gamma_{\text{seed,tile}} = \Gamma_{\text{seed,total}}/2$ and another variation was set up with a point source having a seeding strength of $\Gamma_{\text{seed,tile}} = \Gamma_{\text{seed,total}}/6$. The point source in WallDYN is simulated by setting only a single wall tile as seeding source and the seeding position was chosen to reflect the same poloidal position as in the experiment.

In 2D WallDYN simulations the seeding source is a single tile in the 2D wall. For 3D simulations this means a toroidally averaged source and hence an additional variation with a toroidally averaged source was set up with $\Gamma_{\text{seed,tile}} = \Gamma_{\text{seed,total}}/6 \cdot A_{\text{tile}}/A_{\text{segment}}$, where A_{tile} is the area of a seeding tile and A_{segment} the sum of the area of all seeding tiles in the segment. The seeding positions of the point source and the toroidally averaged source are shown in figure 5.14, where the initial ^{15}N sources from all tiles are depicted as calculated by WallDYN at $t = 0$ s.

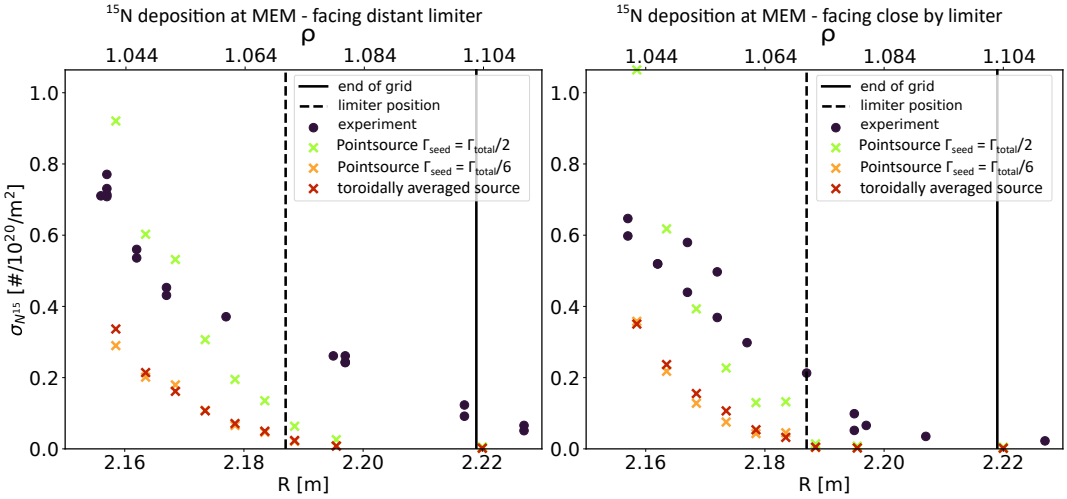

Figure 5.15: ^{15}N deposition at the sides of the mid-plane collector probe for $D_{\perp,^{15}\mathrm{N}} = 0.5\,\mathrm{m}^2/\mathrm{s}$.

Apart from the seeding location and the source strength, also the perpendicular transport coefficient for impurities was varied. Following the closest match between experimental data and simulation from Fig. 9 in [12] a constant perpendicular transport coefficient was chosen for some variations. In figure 5.15 the re-distribution matrix with $D_{\perp,^{15}\mathrm{N}} = 0.5\,\mathrm{m}^2/s$ was used in WallDYN and calculated ^{15}N influxes were use in SDTrimSP to calculate the areal density of ^{15}N. In figure 5.15, the results are compared to experimental data which has already been introduced in section 3.5.
All re-distribution matrices utilised for the 3D WallDYN simulations were normalised with the adapted norm method (see section 4.3.4, figure 4.7). A comparison to the default norm method can be found in the appendix in figure A.4, demonstrating that the chosen norm has only little influence on the final results.
The experimental data on the left picture in figure 5.15 is from the side of the mid-plane collector probe that is facing the distant limiter (blue data point in figure 3.9), while the experimental data on the right picture corresponds to the data facing the close by limiter (red data point in figure 3.9). While the experimental data shows significant deposition in the limiter shadow on the side facing the distant limiter, the simulation results assuming a constant perpendicular transport coefficient of $D_{\perp,^{15}\mathrm{N}} = 0.5\,\mathrm{m}^2/s$ drop close to no deposition in the limiter shadow on both sides of the probe.
In absolute terms the simulation results of the point source with a seeding strength of $\Gamma_{seed} = \Gamma_{total}/2$ matches the experimental data best along these variations. However, the simulations do not accurately reproduce the deposition of ^{15}N in the limiter shadow and the profile shape does not match the experimental profile shape. Also the exponential fall-off lengths, listed in table 5.1, are more than a factor 2 shorter on the probe side facing the distant limiter and almost a factor of 3 on the probe side facing the close by limiter,

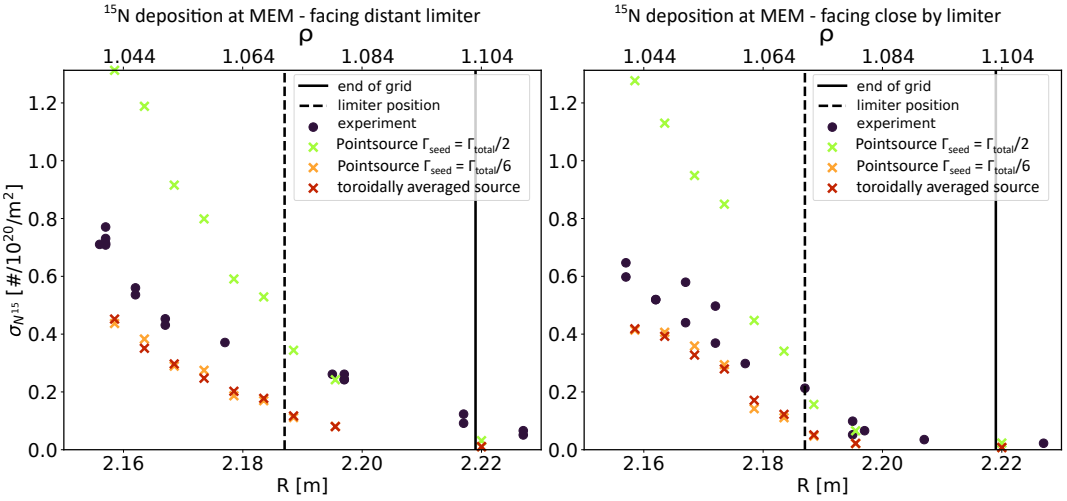

Figure 5.16: ^{15}N deposition at the sides of mid-plane collector probe for $D_{\perp,^{15}\mathrm{N}} = D_{\perp,\mathrm{D}}$

when the data in the limiter shadow is included in the fits.

Table 5.1: Fall-off length of an exponential fit to the data including the limiter shadow for different seeding variations with $D_{\perp,^{15}\mathrm{N}} = 0.5\,\mathrm{m}^2/\mathrm{s}$ and $D_{\perp,^{15}\mathrm{N}} = D_{\perp,\mathrm{D}}$.

seeding variation	distant limiter	close by limiter
point $\Gamma_{seed} = \Gamma_{total}/2$, $0.5\,\mathrm{m}^2/\mathrm{s}$	0.98 cm	1.35 cm
point $\Gamma_{seed} = \Gamma_{total}/6$, $0.5\,\mathrm{m}^2/\mathrm{s}$	0.98 cm	1.43 cm
toroidally averaged, $0.5\,\mathrm{m}^2/\mathrm{s}$	1.13 cm	1.27 cm
point $\Gamma_{seed} = \Gamma_{total}/2$, $D_{\perp,\mathrm{D}}$	1.92 cm	2.37 cm
point $\Gamma_{seed} = \Gamma_{total}/6$, $D_{\perp,\mathrm{D}}$	1.95 cm	2.34 cm
toroidally averaged, $D_{\perp,\mathrm{D}}$	1.99 cm	2.35 cm
experiment	2.47 cm	3.30 cm

Since in the $D_\perp = 0.5\,\mathrm{m}^2/\mathrm{s}$ variation no ^{15}N was deposited in the limiter, new re-distribution matrices were calculated with $D_{\perp,^{15}\mathrm{N}} = D_{\perp,\mathrm{D}}$, assuming that impurities follow the same poloidally varying perpendicular transport coefficient profile as the main plasma species. In the far SOL $D_{\perp,\mathrm{D}}$ has a value of about $1.5\,\mathrm{m}^2/\mathrm{s}$. The profile of the perpendicular transport coefficient has been shown in figure 5.4.
In figure 5.16 the simulated deposition of ^{15}N for $D_{\perp,^{15}\mathrm{N}} = D_{\perp,\mathrm{D}}$ is again compared to the experimental data at the two sides of the MEM. With the higher transport coefficients in the far SOL, the simulations show ^{15}N deposition in the limiter shadows. As in the experiment all seeding variations show more deposition in the limiter shadow on the probe side facing the distant limiter, compared to the side facing the nearby limiter. When focusing on the limiter shadow the best match between simulations and experimental data is achieved with the point source having a seeding strength of $\Gamma_{seed} = \Gamma_{total}/2$.
This seeding variation, however, does overestimate the deposition on probe tiles in the plasma by roughly a factor of 2. Both the toroidally averaged

source and the point source with $\Gamma_{seed} = \Gamma_{total}/6$ underestimate the deposition along the whole profile slightly but do agree well with the profile shape. The calculated exponential fall-off lengths in table 5.1 are still shorter than the experimental one, but are much closer than in the case with $D_{\perp,^{15}\mathrm{N}} = 0.5\,\mathrm{m}^2/\mathrm{s}$. It can hence be concluded that 3D WallDYN simulations can reproduce the experimentally observed deposition of ^{15}N on the mid-plane collector probe, including deposition in the limiter shadows if the perpendicular transport coefficients are chosen appropriately, significantly better than previous 2D WallDYN simulations (compare to 2D WallDYN results in [12]).
In the cases of the toroidally averaged source with $\Gamma_{seed,total} = \Gamma_{total}/6$ and the point source with a seeding strength of $\Gamma_{seed} = \Gamma_{total}/6$ only minor differences can be seen in the simulated ^{15}N deposition on the mid-plane collector probe. This demonstrates, that averaging the source toroidally has only a small effect. Along the conducted variations the simulations with the toroidally averaged source and the point source with $\Gamma_{seed} = \Gamma_{total}/6$ match the experimental data at the mid-plane collector probe best, when the perpendicular transport coefficient of ^{15}N is identical to the main plasma transport coefficient, $D_{\perp,^{15}\mathrm{N}} = D_{\perp,\mathrm{D}}$, while the point source with $\Gamma_{seed} = \Gamma_{total}/2$ matches the deposition in the limiter shadow best.

Apart from deposition data at the outer mid-plane, the divertor manipulator system provided experimental deposition data at the outer divertor for the discharge series around #32024. A comparison of simulated data with experimentally obtained values at the outer divertor is shown in figure 5.17. On the left hand side, the simulated ^{15}N deposition is depicted with variations of the seeding source for $D_{\perp,^{15}\mathrm{N}} = 0.5\,\mathrm{m}^2/\mathrm{s}$ and on the right hand side the results obtained for $D_{\perp,^{15}\mathrm{N}} = D_{\perp,\mathrm{D}}$ can be seen.
Simulated deposition profiles were toroidally averaged over a length corresponding to the actual size of the divertor manipulator system, even though the simulated profiles are mostly toroidally symmetric in the divertor. The seeding variations of the toroidally averaged source and the point source with $\Gamma_{seed} = \Gamma_{total}/6$ result in almost identical deposition results in the divertor, independently of the chosen perpendicular transport coefficients.
The simulated ^{15}N deposition in the private flux region, to the left of the strike line, is underestimated in all cases and does not show a strong peak. As the transport in the private flux region is strongly governed by drifts, which are not included in EMC3-EIRENE, this mismatch is not surprising.
For the variations with $D_{\perp,^{15}\mathrm{N}} = 0.5\,\mathrm{m}^2/\mathrm{s}$, the experimental deposition data outside the private flux region in the divertor is matched well by the point source with $\Gamma_{seed} = \Gamma_{total}/2$, while the deposition in the private flux region is underestimated. The simulations with a point source having $\Gamma_{seed} = \Gamma_{total}/6$ and the toroidally averaged source result in simulated deposition profiles that agree with the trend of the experimental data in the SOL, with a less pronounced peak close to the strike line. The results of the variation with $\Gamma_{seed} = \Gamma_{total}/6$ are not visible in figure 5.17, because they are almost identical with

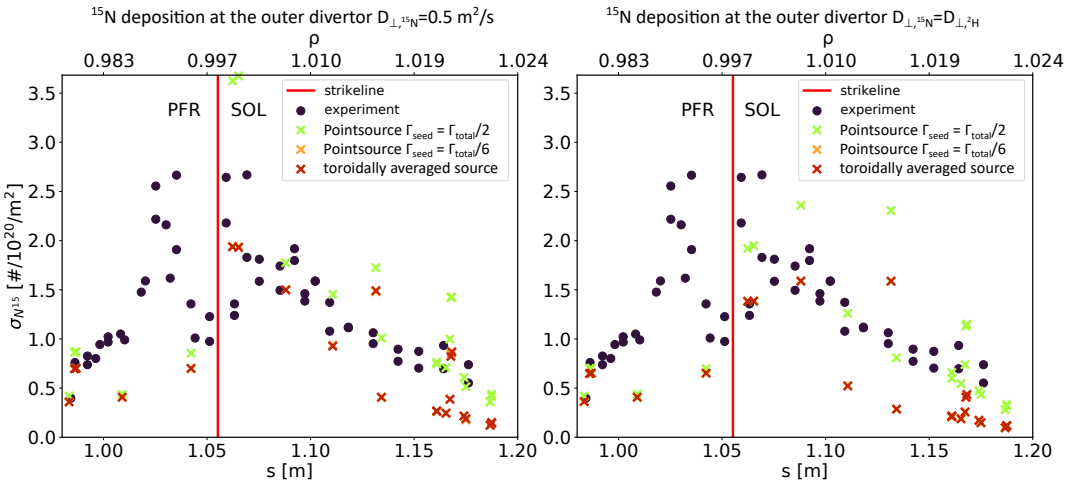

Figure 5.17: Comparison of simulated ^{15}N deposition and experimentally obtained data in the outer divertor for discharge #32024 for different seeding rates and different perpendicular transport coefficients for simulated impurities.

the results of the toroidally averaged source.
Utilising the re-distribution matrix of $D_{\perp,^{15}\mathrm{N}} = D_{\perp,\mathrm{D}}$ results in the simulated deposition profiles in the right picture of figure 5.17. The simulated deposition profile using a point source with $\Gamma_{seed} = \Gamma_{total}/2$ agrees rather well with the experimental data, but is not as peaked close to the strike line and features an additional peak at $s \approx 1.13\,\mathrm{m}$. Reducing the seeding to $\Gamma_{seed} = \Gamma_{total}/6$ with the point source or averaging the point source toroidally results in an underestimation along the whole divertor.
For both variations of perpendicular transport coefficients ($D_{\perp,^{15}\mathrm{N}} = 0.5\,\mathrm{m}^2/\mathrm{s}$ and $D_{\perp,^{15}\mathrm{N}} = D_{\perp,\mathrm{D}}$), the best match between simulated ^{15}N deposition and experimental results is achieved with the point source having a seeding strength of $\Gamma_{seed} = \Gamma_{total}/2$.
The best overall matching variation was achieved with the point source with $\Gamma_{seed} = \Gamma_{total}/2$ and a perpendicular transport coefficient of $D_{\perp,^{15}\mathrm{N}} = D_{\perp,\mathrm{D}}$. In this variation the simulated ^{15}N deposition in the limiter shadows upstream agreed well with the experimental data, while the simulated ^{15}N deposition at the plasma exposed area of the probe is overestimated by a factor of $1.5 - 2.0$. At the same time the simulated ^{15}N deposition outside the PFR in the divertor agrees reasonably well with the experimental results.
The achieved match between the simulated and the experimentally measured ^{15}N deposition for a seeding source with $\Gamma_{seed} = \Gamma_{total}/2$ and a perpendicular transport coefficient of $D_{\perp,^{15}\mathrm{N}} = D_{\perp,\mathrm{D}}$ suggests that the ^{15}N concentration in the plasma is not completely toroidally symmetric, because the simulated geometry represents only 1/6 of the full torus. It suggests that ^{15}N from a seeding source in the divertor close to observed probes is preferably deposited close to seeding valves before being recycled and distributed toroidally. The obtained simulations results suggest that the effective seeding strength in the

experiment is in between $\Gamma_{seed} = \Gamma_{total}/2$, which overestimates the deposition slightly, and $\Gamma_{seed} = \Gamma_{total}/6$, which underestimates the deposition.

5.3 Background simulations of #35616 with EMC3-EIRENE

To interpret the ^{15}N deposition measured at the outer mid-plane probe and in the divertor after the discharge series around discharge #35616, a plasma background was simulated with EMC3 as a basis to calculate a 3D re-distribution matrix for WallDYN. The discharge #35616 was chosen because it had the most stable divertor conditions of the series from #35610 to #35617.
The magnetic configuration was the same as in discharge #32024. The seeding location for ^{15}N was changed to a single valve at the top of the tokamak, which can maintain a small seeding flux without modulation. The experiment allows to investigate the ^{15}N deposition with seeding from a different poloidal position than during #32024. The deuterium fueling in the divertor and at the outer mid-plane remained the same. It was coupled to a feedback loop to control the divertor temperature, resulting in two periods of increased seeding for D_2 in the timetrace in figure 3.11, presented in section 3.5. The simulations aim to reproduce the plasma background at $t = 3.0\,\mathrm{s}$, in the middle of the flat top phase and in-between NBI blips.
The input values for the EMC3-EIRENE simulations were determined from the averaged experimental data from $t = 2.95\,\mathrm{s}$ to $3.05\,\mathrm{s}$, where the physical quantities were in a flattop phase. A more detailed investigation revealed that the divertor quantities show fast oscillation which can be attributed to I-phase oscillations as shown in figure 3.10, in section 3.5.
Contrary to the goal of having a set of L-mode discharges, detailed investigations have shown that all discharges in the series around discharge #35616 were in I-phase. The integrated data analysis for $t = 2.95$ to $3.05\,\mathrm{s}$ results in a separatrix temperature of $T_{e,sep} \approx 91\,\mathrm{eV}$, a separatrix density of $n_{e,sep} \approx 0.96 \cdot 10^{19}\mathrm{m}^{-3}$, a total heating power of $P_{heat,tot} \approx 1.30\,\mathrm{MW}$ and a total radiated power of $P_{rad,tot} \approx 0.86\,\mathrm{MW}$. The total heating power consists of Ohmic heating and electron cyclotron resonance heating. The simulation volume was radially confined to a normalised plasma radius of $\rho \geq 0.98$, reducing the effective heating power to $P_{heat,eff} \approx 0.80\,\mathrm{MW}$ and the effective radiated power to $P_{rad,eff} \approx 0.36\,\mathrm{MW}$ as estimated by tomographic reconstruction, which suggests $P_{rad} = 0.5\,\mathrm{MW}$ inside the region of $\rho < 0.98$.
The radiated power in the simulation volume has to be radiated by the nitrogen impurity. To calculate the plasma background the nitrogen is seeded into the plasma from all wall tiles to mimic the recycling of ^{15}N at the wall. The impurity distribution is calculated applying the fluid model from equation 2.16 and the total ^{15}N density is scaled to match the given radiated power.
Deuterium is seeded from a point source in the divertor baffle and the particle

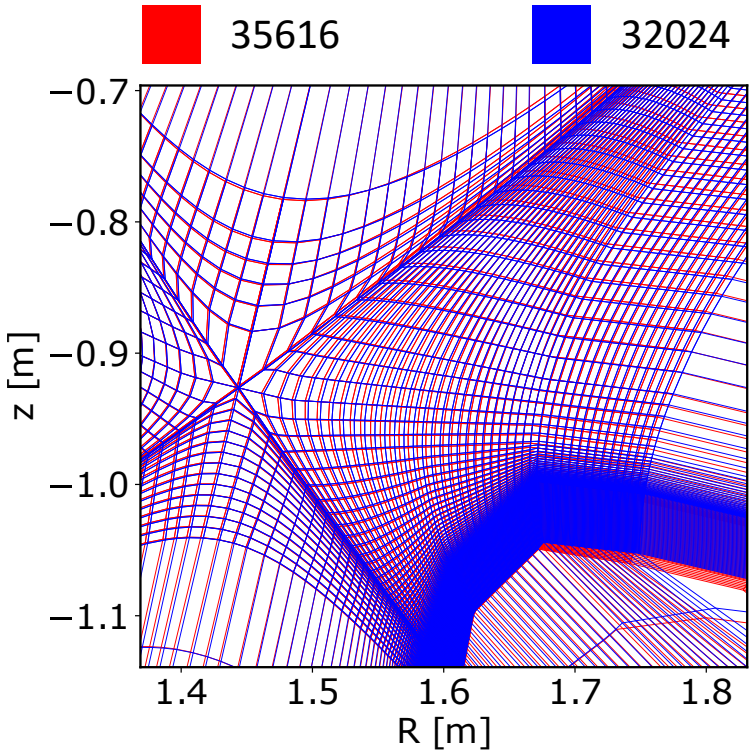

Figure 5.18: Enlarged detail of an overlap of simulations grids for discharge #35616 in red and discharge #32024 in blue. It shows the X-point and the outer divertor region of the grids.

balance is achieved by balancing the recycling flux to achieve a separatrix density equal to the measured value of $n_{e,sep}$. To account for pumping, a surface with an albedo of 0.88 is located behind the outer divertor target plates.
The boundary conditions for the simulation volume are identical to the previously used ones in section 5.1.

A field aligned grid was constructed with magnetic equilibrium reconstruction. In the experiment, the magnetic field configuration was set to be identical to the configuration of discharge #32024 and hence the constructed grid is almost identical for both simulated backgrounds. Differences can only be seen in an enlarged detail of an overlap of both grids in figure 5.18, where the grid of discharge #35616 is shown in red and the grid calculated for discharge #32024 in blue. The detail shows the X-point region with the separatrix of both grids, as well as the outer divertor region.

Identical to the previous background simulation for discharge #32024 in section 5.1, the full grid consists of two grid with 30° toroidal extent. The simulations for discharge #35616 were conducted in the 3D geometry shown in figure 5.2. Matching a plasma background in this 3D geometry to experimental data has proven quite difficult due to fast oscillations in the divertor data and a time dependency of the divertor heat flux and hence the effective heating power due to nitrogen build up in the plasma.

In figure 5.19 a) the simulated electron density profile is compared to the experimental data obtained from the lithium beam and the Thomson scattering diagnostic. The right hand side axis indicates the perpendicular transport coefficient for the deuterium ions. The Thomson data varies close to the separatrix, indicating a steep density profile, while the lithium beam data is much smoother. The simulated profile is a compromise aiming to reproduce a steeper profile around the separatrix while still matching the density data obtained from the lithium beam. Note, that the Thomson profiles are shifted by 3 mm radially outwards to match a separatrix temperature between 50 and 60 eV, characteristic for L-mode discharges. Similarly to the previous simulations, the lithium beam profile was shifted by 7 mm radially inwards to match the Thomson profile. The shifts are well within radial uncertainties from the magnetic equilibrium reconstruction and the Thomson diagnostic of up to 1.5 cm for edge profiles in ASDEX Upgrade [42].
The mismatch between the average separatrix temperature of $T_{e,sep} \approx 91$ eV as predicted by the integrated data analysis and the typical L-mode temperatures is linked to the I-phase oscillations and an oscillating separatrix position. In figure 5.19 b) the simulated electron temperature is compared to the electron temperature obtained from the Thomson diagnostic with the blue dotted line showing the perpendicular heat transport coefficient. The simulated electron temperature lies well within the experimental scatter.
The simulated ion temperature profile in figure 5.19 c) matches the experimental data obtained from CXRS well at the separatrix and in the SOL, while the experimental data suggest a higher temperature in the confined region.

In figure 5.20 a) the simulated ion saturation current is plotted together with the values obtained from Langmuir probes. Data at the inner target is shown in red and results for the outer divertor are indicated in blue. The I-phase oscillations at around 4 kHz result in a broad scatter of experimental data at the inner divertor. In comparison to the simulated results the experimental data indicate slightly broader profiles outside the confined region and a faster drop inside the confined region.
In figure 5.20 b) the electron temperature at the target obtained from simulations is compared to Langmuir probe data, that indicate a strong asymmetry between inner and outer divertor. This asymmetry is not reproduced by the EMC3-EIRENE simulations. The missing asymmetry in EMC3-EIRENE simulations has already been explained in section 5.1.3 for the simulated plasma backgrounds for discharge #32024.
The experimental data at the outer target indicates a slightly higher peak temperature than obtained from the simulations, but in figure 5.20 c) the maximum of the simulated heat flux is very close to the peak obtained from IR thermography, which additionally indicates a more narrow profile than calculated with EMC3-EIRENE.

In summary, the simulated plasma background mostly agrees with the experimental data within uncertainties, but does not reproduce all profiles at the

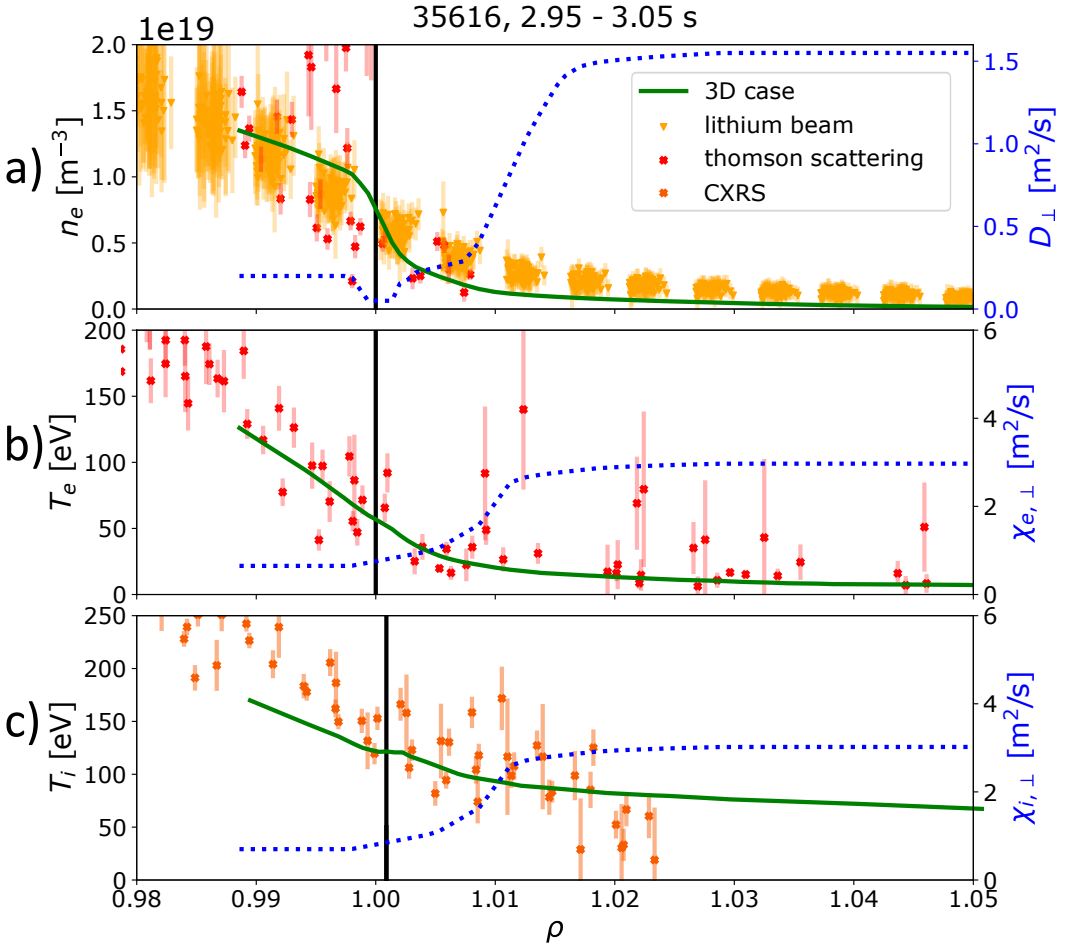

Figure 5.19: Comparison of 3D EMC3-EIRENE simulation results with experimental data upstream at the outer mid-plane for discharge #35616. a) electron density, b) electron temperature, c) ion temperature.

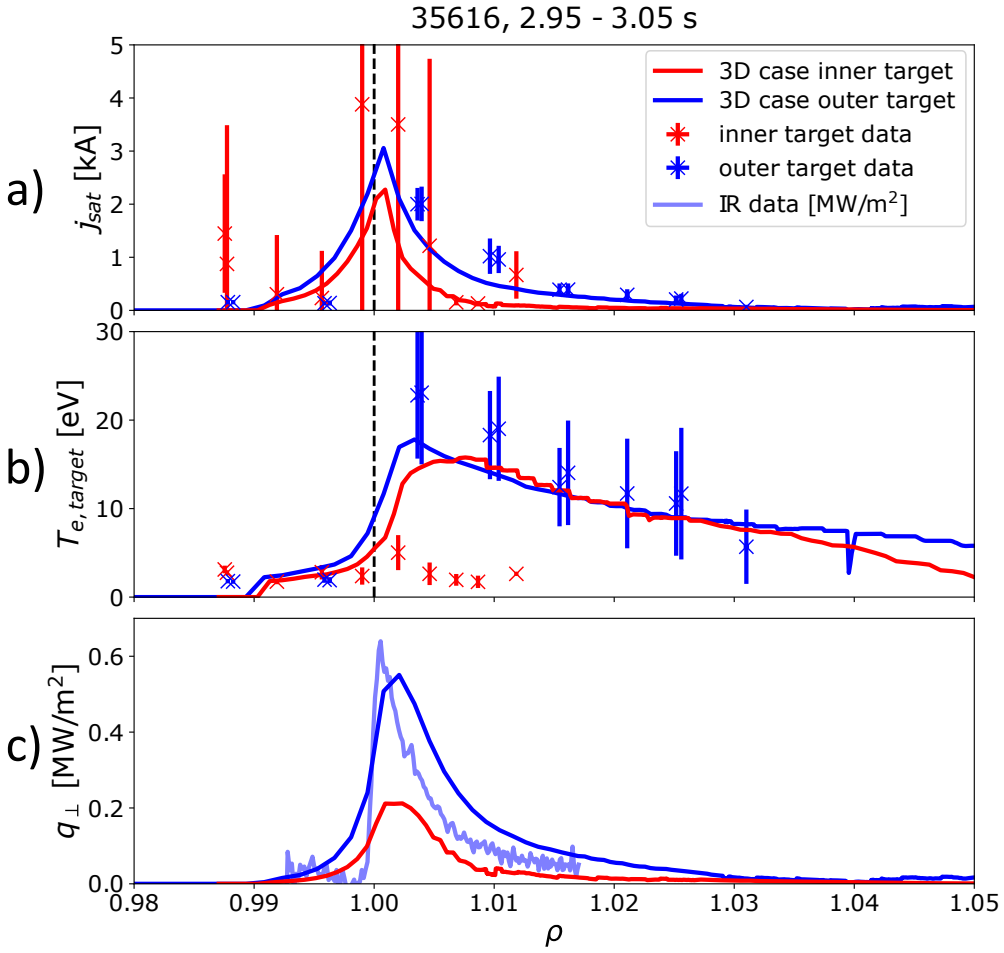

Figure 5.20: Comparison of 3D EMC3-EIRENE simulation results with experimental data downstream at the divertor target for discharge #35616. a) Ion saturation current : experimental data from Langmuir probes. b) Plasma temperature at the divertor target, c) Heat flux perpendicular to the divertor target : experimental data from an infrared camera.

same time. Variations of input parameters and perpendicular transport parameters resulted in a better agreement of upstream profiles, but were never able to match experimental downstream data sufficiently at the same time.

5.4 3D WallDYN simulations for #35616

Based on the EMC3-EIRENE plasma background for #35616 re-distribution matrices for ^{184}W and ^{15}N were calculated in the 3D geometry shown in figure 5.2 for a total of 1367 wall elements. In contrast to the re-distribution matrices for #32024, the top of the chamber was included in the re-distribution to setup a point seeding source from the top in WallDYN simulations. All matrices were normalised with the adapted norm (see section 4.3.4). ^{15}N was seeded from a single valve in sector 2, while the simulated geometry corresponds to the mid of sector 6 to sector 9 (see figure 3.6). The seeding location in the WallDYN simulation was chosen such that it overlaps with the experimental seeding location when the simulation geometry is re-produced in toroidal direction. In figure 5.21 the seeding location is indicated by the red tile at the top of the chamber. On the right hand side the limiters and the mid-plane collector probe are visible.
As in section 5.2 only minor differences between the toroidally averaged source and the point source were observed, the WallDYN simulations for #35616 were only carried out for point sources with varying seeding strengths.

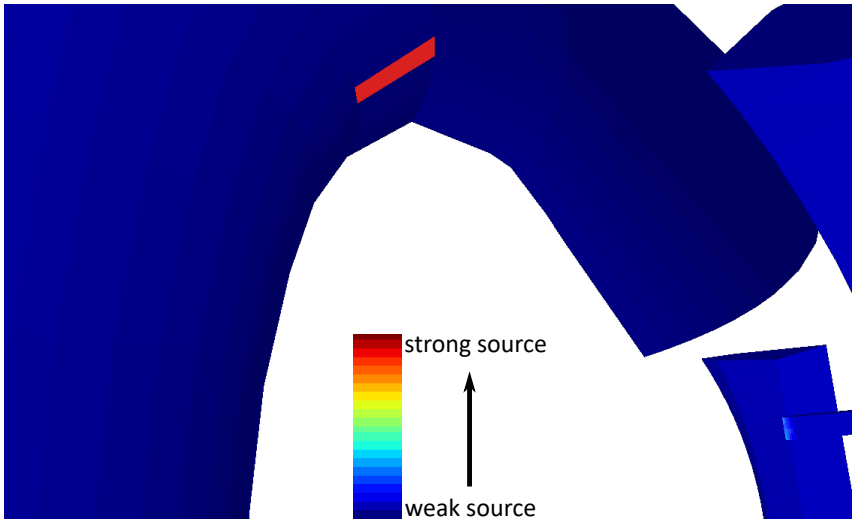

Figure 5.21: Particle sources calculated by WallDYN before the first time step at the top of the chamber. The seeding tile at the top of the chamber is colored in red and parts of the limiters and the mid-plane collector probe are visible on the right hand side.

In the experiment, all ^{15}N atoms were seeded from a single point source. This is represented in a simulation with a point source with $\Gamma_{seed} = \Gamma_{total}$. As the geometry is essentially multiplied six times in toroidal direction due to the mapping boundary condition, this variation leads to a higher ^{15}N content in the

plasma than in the experiment. Due to the fact that the seeding valve in the experiment was in a different sector than the MEM, the effective ^{15}N seeding strength in the simulated segment was estimated to be between $\Gamma_{total}/6 \leq \Gamma_{seed,eff} \leq \Gamma_{total}$. Therefore, further simulations were conducted with seeding rates of $\Gamma_{seed} = \Gamma_{total}/2$ and $\Gamma_{seed} = \Gamma_{total}/6$, from the same position.
Additionally, simulations at two values of the perpendicular transport coefficients for ^{184}W and ^{15}N were carried out. As before, one variation with constant perpendicular transport coefficients of $D_{\perp,^{15}\mathrm{N}} = D_{\perp,^{185}\mathrm{W}} = 0.5\,\mathrm{m}^2/\mathrm{s}$ and one with $D_{\perp,^{15}\mathrm{N}} = D_{\perp,^{185}\mathrm{W}} = D_{\perp,\mathrm{D}}$. The profile of $D_{\perp,\mathrm{D}}$ is indicated in figure 5.19 a) in section 3.5.
WallDYN was again coupled to SDTrimSP to include the profile depth effects of ^{15}N deposition (see section 4.3.3). Simulation results using a re-distribution matrix following $D_{\perp,^{15}\mathrm{N}} = 0.5\,\mathrm{m}^2/\mathrm{s}$ are compared to experimentally obtain values at the mid-plane collector probe in figure 5.22. As introduced in section 3.5.2, four different deposition profiles were analysed experimentally (see figure 3.12).
Two profiles accumulated over several discharges, plotted in the left of figure 5.22, and two profile accumulated during a single discharge, shown in the right picture.

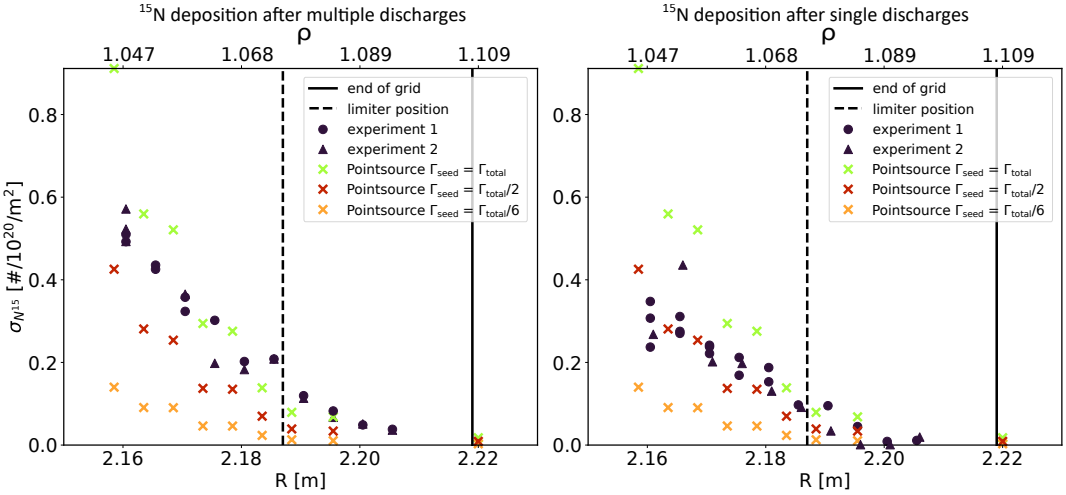

Figure 5.22: Simulated deposition profiles at the mid-plane collector probe as calculated by coupling WallDYN to SDTrimSP for $D_{\perp,^{15}\mathrm{N}} = 0.5\,\mathrm{m}^2/\mathrm{s}$. The left hand side picture shows the deposited ^{15}N during single discharge experiments and on the right hand side the deposition after multiple discharges.

Experiment 1 and 2 refer to the different exposure positions on the mid-plane collector probe with cap that was rotated in between discharges and hence correspond to different discharges.
In the left picture, experiment 1 and 2 correspond to the ^{15}N deposition accumulated after discharges #35610 to #35612 and discharges #35615, #35616, respectively (position 1 and 3 in figure 3.12 in section 3.5).
In the right picture, experiment 1 and 2 refer to the measured ^{15}N deposition

from discharges #35613 and #35617, respectively (position 2 and 4 in figure 3.12 in section 3.5).
The simulated data is identical in both pictures. The comparison shows that the simulation with a point source having $\Gamma_{seed} = \Gamma_{total}/6$ underestimates the deposition by a factor of 2 to 3 along the radial extent, while a point source with $\Gamma_{seed} = \Gamma_{total}$ overestimates the peak value by roughly a factor of 1.5. The simulation results with $\Gamma_{seed} = \Gamma_{total}/2$ agrees very well with the experimental data at the mid-plane collector probe.

Table 5.2: Fall-off length of an exponential fit to the data including the limiter shadow for $D_{\perp,^{15}\mathrm{N}} = 0.5\,\mathrm{m}^2/\mathrm{s}$.

seeding variation	fall-off length
pointsource $\Gamma_{seed} = \Gamma_{total}$	1.45 cm
pointsource $\Gamma_{seed} = \Gamma_{total}/2$	1.55 cm
pointsource $\Gamma_{seed} = \Gamma_{total}/6$	1.50 cm
experiment 1 single discharge	2.47 cm
experiment 2 single discharge	2.22 cm
experiment 1 multiple discharges	2.08 cm
experiment 2 multiple discharges	1.95 cm

The comparison in table 5.2 shows that the simulated profiles have a shorter fall-off lengths than the experimental profiles. As in the simulations for discharge #32024 the fall-off length is mainly independent of the seeding strength. Even though, the run with $\Gamma_{seed} = \Gamma_{total}/2$ is closest to the experimental fall-off lengths.

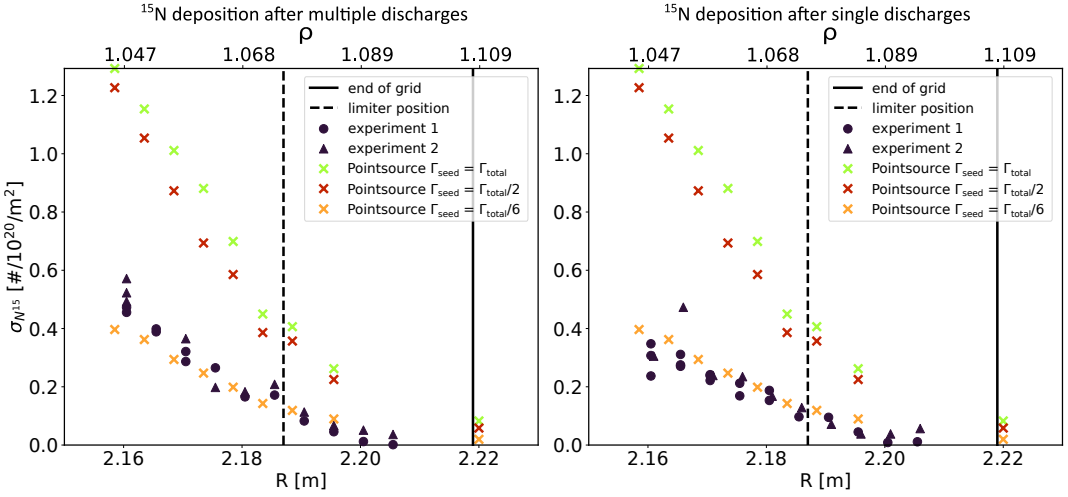

Figure 5.23: The same deposition profiles as in figure 5.22 but with perpendicular transport coefficient $D_{\perp,^{15}\mathrm{N}} = D_{\perp,\mathrm{D}}$.

Simulation results using the re-distribution matrix with $D_{\perp,^{15}\mathrm{N}} = D_{\perp,\mathrm{D}}$ are compared to data from the mid-plane collector probe in figure 5.23. The

experimentally obtained deposition data in the left picture again corresponds to profiles accumulated over several discharges and the right picture shows the data obtained by NRA for the accumulation during a single discharge.
Assuming the same transport coefficient for main plasma ions and impurities in WallDYN results in an overestimation of the deposition by a factor of at least 2 and even more in the limiter shadow for point sources with seeding strengths of $\Gamma_{seed} = \Gamma_{total}$ and $\Gamma_{total}/2$. A point source having $\Gamma_{seed} = \Gamma_{total}/6$ on the other hand results in deposition profiles that agree rather well with the data obtained from NRA both in the limiter shadow and in the plasma.
The fall-off lengths of simulated deposition profiles with $D_{\perp,^{15}\mathrm{N}} = D_{\perp,\mathrm{D}}$ are only slightly larger than in the experiment for point sources with $\Gamma_{seed} = \Gamma_{total}$ and $\Gamma_{total}/2$ as shown in table 5.3. The fall-off length obtained from a point source with $\Gamma_{seed} = \Gamma_{total}/6$ even lies in the range of experimentally obtained fall-off lengths.

Table 5.3: Fall-off length of an exponential fit to the data including the limiter shadow for $D_{\perp,^{15}\mathrm{N}} = D_{\perp,\mathrm{D}}$.

seeding variation	**fall-off length**
pointsource $\Gamma_{seed} = \Gamma_{total}$	2.60 cm
pointsource $\Gamma_{seed} = \Gamma_{total}/2$	2.51 cm
pointsource $\Gamma_{seed} = \Gamma_{total}/6$	2.34 cm
experiment 1 single discharge	2.47 cm
experiment 2 single discharge	2.22 cm
experiment 1 multiple discharges	2.08 cm
experiment 2 multiple discharges	1.95 cm

Since for both values of the perpendicular transport coefficients, the best match with the experimental data is found for different seeding strengths, a comparison to experimental data in the divertor is necessary. In the discharge series around #35616, the DIM samples are made of molybdenum with varying roughness and markers (see figure 3.13). Because all other tiles in the divertor during that discharge series are tungsten tiles and expected ^{15}N deposition is very similar between molybdenum and tungsten (see figure 3.8), a pure tungsten divertor was simulated in WallDYN.
The left side of figure 5.24 compares the simulated ^{15}N deposition profiles in the divertor for $D_{\perp,^{15}\mathrm{N}} = 0.5\,\mathrm{m}^2/\mathrm{s}$ with experimental data obtained from nuclear reaction analysis (NRA) of samples exposed on the divertor manipulator. The y-axis is limited to 5 for better comparison with the picture on the right hand side, where the results with $D_{\perp,^{15}\mathrm{N}} = D_{\perp,\mathrm{D}}$ are presented. A full range version can be found in the appendix in figure A.5.
The simulation results show a slight overestimation of ^{15}N deposition left of the strike line in the private flux region for $\Gamma_{seed} = \Gamma_{total}/6$ and a large overestimation for $\Gamma_{seed} = \Gamma_{total}/2$. The deposition in the case $\Gamma_{seed} = \Gamma_{total}$ is even larger, does not match the experimental data left of strike line and also

overestimates the deposition to the right of the strike line.
For $\Gamma_{seed} = \Gamma_{total}/6$ the deposition profile is peaked slightly to the right of the strike line, not matching the peak position of the experimental data. However, shifting experimental data or simulated data horizontally would result in rather good agreement.
The peak of the ^{15}N deposition profile of the variation with $\Gamma_{seed} = \Gamma_{total}/2$ is out of the scale and in combination with the overestimation in the private flux region, the experimental data cannot be matched in the divertor. This variation matches the experimental data at the mid-place collector probe best, but as it does not match the experimental results in the divertor, the simulation case is not considered representative for the experiment.
The seeding level $\Gamma_{seed} = \Gamma_{total}/6$ more or less matches the divertor data but underestimates the deposition at the mid-plane and the variation with $\Gamma_{seed} = \Gamma_{total}$ largely overestimates the deposition of ^{15}N in the divertor. Therefore, for all seeding levels the simulated deposition does not agree with experimental data when a constant perpendicular transport coefficient of $D_{\perp,^{15}\mathrm{N}} = 0.5\,\mathrm{m}^2/\mathrm{s}$ is chosen.

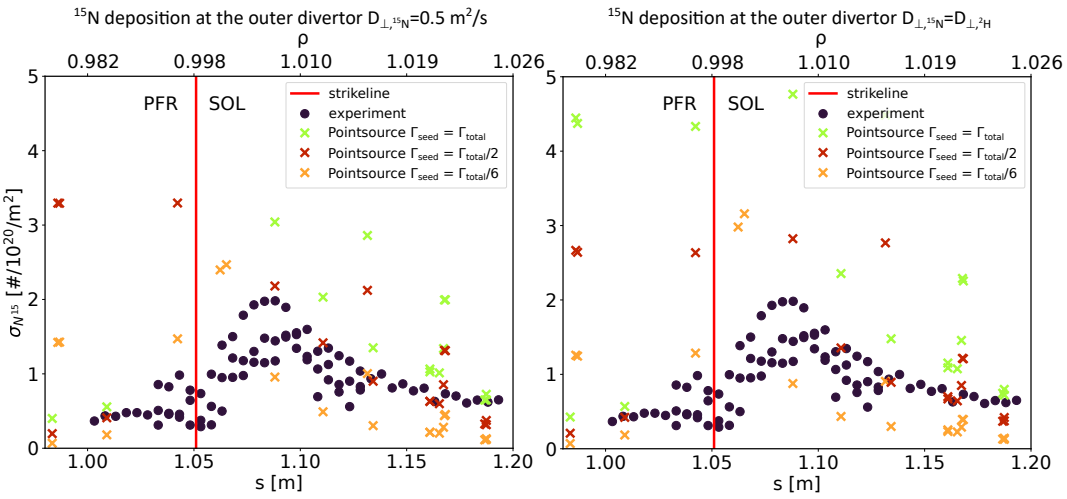

Figure 5.24: Comparison of simulated ^{15}N deposition and experimentally obtained data in the outer divertor for the discharge series around #35616 for different seeding variations and different perpendicular transport coefficients for simulated impurities.

For $D_{\perp,^{15}\mathrm{N}} = D_{\perp,\mathrm{D}}$, on the right hand side of figure 5.24, the seeding cases $\Gamma_{seed} = \Gamma_{total}$ and $\Gamma_{total}/2$ both overestimate the deposition along the whole divertor, which was already observed at the mid-plane. For the case $\Gamma_{seed} = \Gamma_{total}/6$ the deposition in the private flux region is slightly smaller than in the same seeding case with $D_{\perp,^{15}\mathrm{N}} = 0.5\,\mathrm{m}^2/\mathrm{s}$, but has a slightly larger peak close to the strike line.
In summary, the seeding variation $\Gamma_{seed} = \Gamma_{total}/6$ with the perpendicular transport parameter $D_{\perp,^{15}\mathrm{N}} = D_{\perp,\mathrm{D}}$ matches the experimental data best. The simulation is in very good agreement with experimental data at the mid-plane and shows reasonable agreement in the divertor.

As during the experiment the seeding source was located at a different toroidal position than in the simulation setup, the majority of ^{15}N reaching the simulated segment, which represents only 1/6 of the full geometry, during the experiment has been recycled multiple times before reaching the mid-plane probe. The reasonable match between the simulated and experimentally measured ^{15}N deposition with $\Gamma_{seed} = \Gamma_{total}/6$ suggests that the ^{15}N concentration during the experiment was mostly toroidally symmetric. It also indicates that the poloidal position of the seeding source does not have a strong influence on the ^{15}N deposition at the MEM and at the analysed positions in the divertor.

Chapter 6

Summary and conclusion

The presented work contributes to the understanding of impurity migration in tokamaks, which is relevant to optimise radiative cooling of the plasma edge and governs the formation of mixed material layers at the first wall. In previous work the nitrogen areal densities as determined by nuclear reaction analysis could be reproduced by 2D simulations in the divertor of ASDEX Upgrade, but not at the outer mid-plane. Therefore, it was suggested that the influence of 3D geometry is crucial for a comprehensive understanding of impurity migration in magnetic confinement fusion devices.
The 3D extension of WallDYN utilizing EMC3-EIRENE enables the investigation of impurity migration in 3D geometry, including features like poloidal rib limiters and probes.

In this thesis, the influence of the 3D geometry on plasma parameters was investigated by simulating plasma backgrounds for ASDEX Upgrade discharge #32024, a flat top L-mode discharge with nitrogen seeding from the divertor, in 2D and 3D geometry with the scrape-off layer transport code EMC3-EIRENE (section 5.1). To match available experimental data with the simulated plasma background, the perpendicular transport coefficients were adapted in the 3D simulation and were kept identical for the simulation in 2D geometry.
The differences between 2D and 3D simulation results with respect to commonly used plasma parameters at the low field side, such as the electron temperature T_e, the electron density n_e, and the ion temperature T_i, and plasma parameters at the divertor targets plates, such as the saturation current j_{sat}, the electron temperature $T_{e,target}$, and the heat flux perpendicular to the target plate $q_\perp$, were found to be negligible.
However, the plasma flow, which strongly influences the transport of impurities, is significantly different in 2D and 3D simulations. Through analyses of recycling sources these differences could be attributed to different transport paths for neutral particles from the divertor structure to the LFS main chamber. These lead to differences in the distribution of ionisation sources at the LFS, which drive the plasma flow.

The deposition is accounted for by the WallDYN surface model, which assumes

a constant concentration of deposited material in a reaction zone and thereby cannot handle depth profile dependent effects, where erosion of particles occurs at the top surface layer of a material, while particles are potentially deposited behind that layer. To cover these effects and ensure that deposited nitrogen is not directly re-eroded in the simulations, the equilibrium particles fluxes as calculated by WallDYN are fed into the monte-carlo code SDTrimSP, that can dynamically calculate the surface composition of a material and computes the areal density of nitrogen including the depth profile effects. To ensure that the particle fluxes calculated by WallDYN are reliabe the predicted gross erosion flux from every tile into the plasma was successfully benchmarked to the predicted gross erosion flux as calculated by SDTrimSP with the same input parameters.

The redistribution of nitrogen during the discharge #32024 was computed in 3D geometry with EMC3-EIRENE and the resulting redistribution matrix was used in the combination WallDYN and SDTrimSP. By adapting the nitrogen seeding strength to the simulated geometry and varying the perpendicular transport coefficients it was possible to match simulated nitrogen areal densities with experimental results from nuclear reaction analysis (section 3.5.1), both upstream at a mid-plane deposition probe and downstream in the divertor as described in section 5.2. This confirms the hypothesis that the overestimation of deposited N at the mid-plane collector probe (MEM) in previous work was a result of using 2D codes to model a 3D geometry.

The deposition as simulated by the combination of WallDYN and SDTrimSP depends strongly on the amount of seeded nitrogen, but was not very sensitive to whether the nitrogen was seeded from only a single wall tile or from a toroidally averaged source. Additionally, the simulated nitrogen deposition profiles were shown to be strongly dependent on the chosen perpendicular transport coefficient. Better agreement between simulated deposition profiles and experimental deposition data was achieved by assuming that nitrogen impurities follow the same transport coefficient as the main plasma species, instead of assuming a constant transport coefficient.

In order to investigate the influence of the poloidal position of the nitrogen seeding on nitrogen deposition at the mid-plane deposition probe, ASDEX Upgrade discharges #35610 to #35617 were performed with nitrogen seeding from the top of the chamber. Additionally, during these discharges the fluence dependence of nitrogen accumulation at the mid-plane deposition probe was investigated by exposing different areas of the probe to different numbers of discharges. To that end, the rotating deposition probe was covered by a cap with a slit and the probe was rotated in-between discharges.
The deposited nitrogen at different positions was determined ex-situ via NRA (section 3.5.2) and it was found that the areal density of nitrogen did saturate with exposure times, confirming results from a previous work, where no dependency of deposited nitrogen on the fluence was found.
Both the fall-off length as well as the peak values of the nitrogen deposition

profiles at the mid-plane collector probe were very similar for the discharge series where it was seeded from the divertor and the series, where nitrogen was seeded from the top of the plasma chamber.
The nitrogen deposition after this set of discharges was also successfully modelled with the combination of WallDYN and SDTrimSP, again using the same perpendicular transport coefficient for nitrogen and the main plasma species. With this input choice it was possible to model the nitrogen deposition at the mid-plane collector probe in the limiter shadow for the discharge series around #32024 and #35616.

The presented results highlight the importance of taking 3D geometry into account, when one is interested in plasma flow patterns and impurity migration. The results from WallDYN simulations in 3D geometries coupled to SDTrimSP resolve the discrepancies of simulated and observed nitrogen deposition at the outer mid-plane of ASDEX Upgrade and demonstrate the applicability of WallDYN to 3D geometries. Furthermore, the ability of WallDYN to compute nitrogen deposition in 3D geometries is reassuring for the understanding of plasma-wall interaction and optimisation of power exhaust in future fusion reactors.

Appendix A

Additional figures

Figure A.1 shows a single tile from the divertor manipualtor that was equipped during the discharges series from #35610 to #35617. The six samples are light grey and six dummy samples are visible in dark grey.

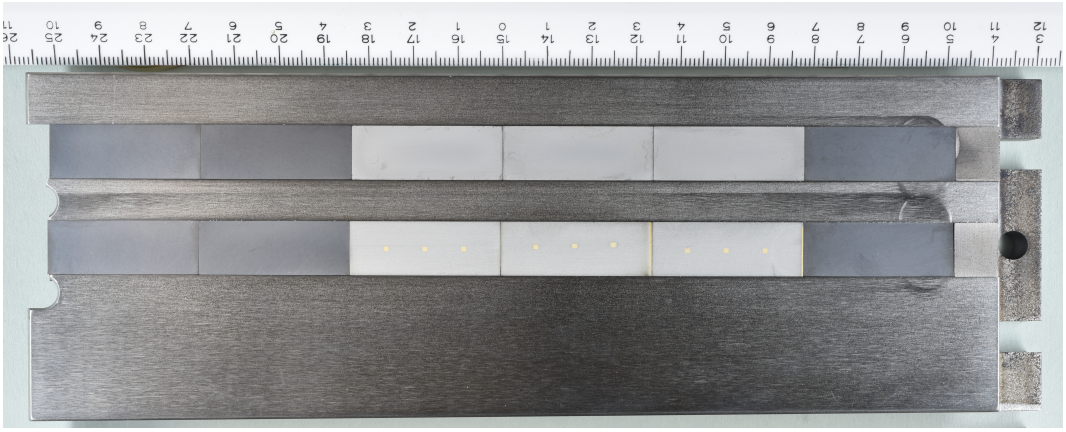

Figure A.1: A single tile of the DIM with inserted deposition samples used in the discharge series from #35610 to #35617.

Figure A.2 shows the shadowing effect of deposited ^{15}N on the MEM as a result of the cap and the inclined field line angle. The left picture illustrates the shadowing effect. On the right hand side the ^{15}N density, as measured by NRA at a fixes radial position, is plotted over the rotation angle of the MEM. The shadowing effect results in reduced ^{15}N at angles between 353° and 360°. The NRA measurements after the discharge series around #35616 were taken at angles $80 + n\frac{\pi}{2}$ with $n \in [1, 2, 3, 4]$, i.e. 350 ° on the right hand side picture. In figure A.3 the composition of the MEM coating is shown as specified by the manufacturer. The tungsten coating on the surface sits on an molybdenum interlayer.
The influence of the normalisation method on ^{15}N deposition at the MEM is shown in figure A.4 for different perpendicular transport coefficients $D_{\perp}$. The default normalisation results in slightly higher deposition, but the overall effect

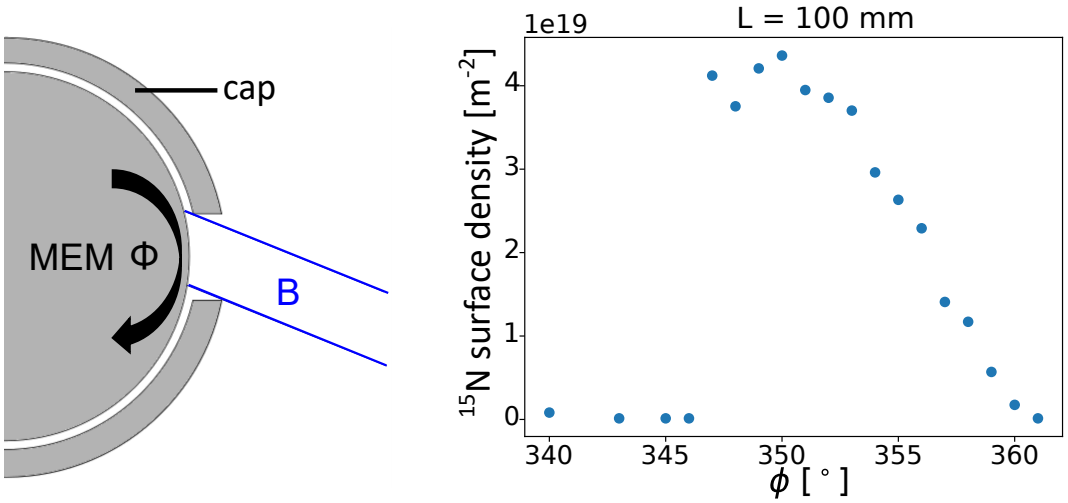

Figure A.2: Left: Depiction of the shadowing due to the field line angle, right: ^{15}N surface density from NRA measurements at a fixed radial position. Measurements in the analysis of #35616 were conducted at angles $80 + n\frac{\pi}{2}$ (i.e. 350 ° on the right hand side).

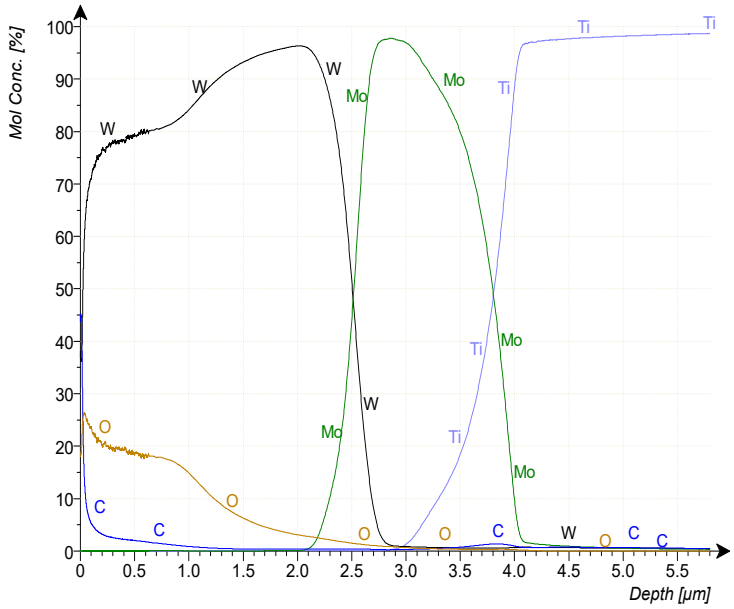

Figure A.3: Coating of the mid-plane collector probe used in the discharge series around #35616.

is very small. Simulated ^{15}N deposition results presented in this thesis were normalised with the adapted normalisation.
In section 5.4, the simulated ^{15}N deposition results in the divertor are shown with a y-axis that is capped at 5. Figure A.5 shows the full range of these plots. For both perpendicular transport coefficients the variation with $\Gamma_{seed} = \Gamma_{total}$ results in significantly more ^{15}N deposition as visible in section 5.4 and hence does not reproduce the experiment.

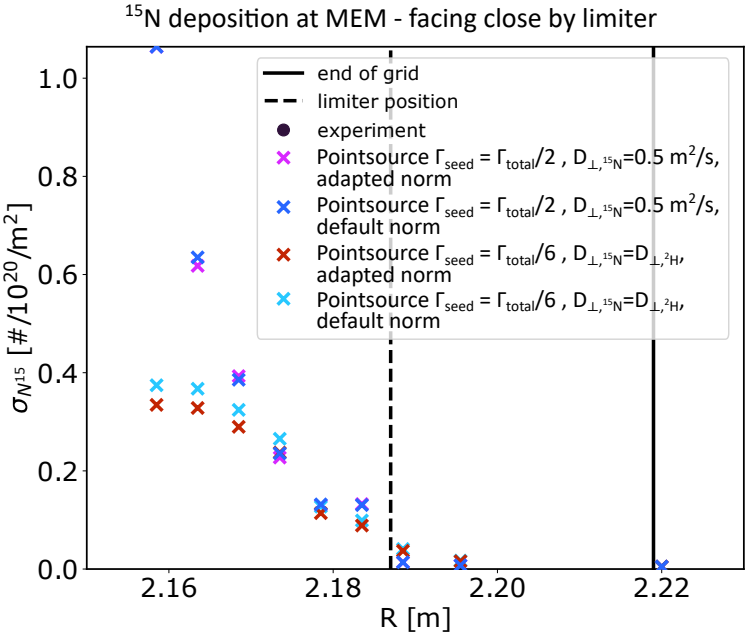

Figure A.4: Comparison of adapted and default normalisation for different transport parameters and seeding rates the the mid-plane collector probe.

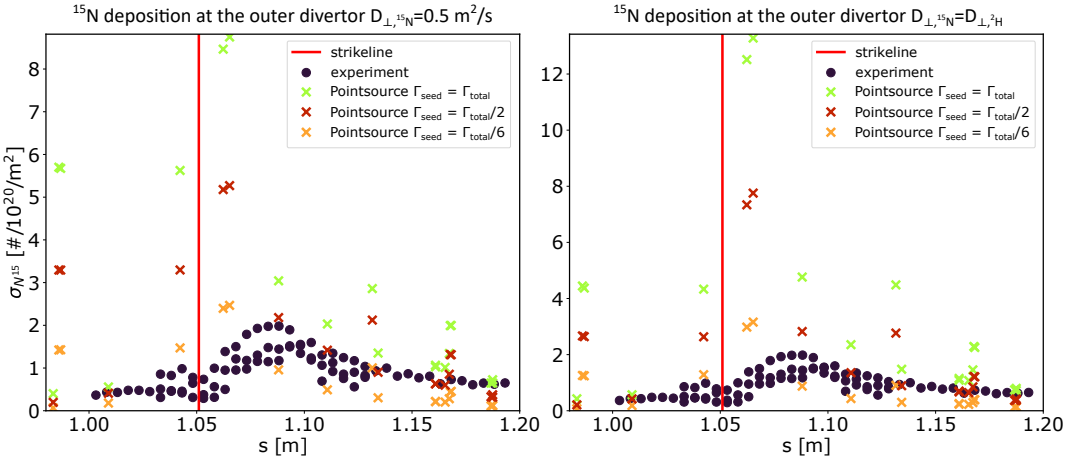

Figure A.5: Full range simulation results for WallDYN coupled to SDTrimSP for the outer divertor based on the plasma background for discharge #35616.

Bibliography

[1] R. Toschi, "Nuclear fusion, an energy source," in *Fusion technology 1996* (C. VARANDAS, F. Serra, and C. VARANDAS, eds.), pp. 1–8, Amsterdam: Elsevier, 1997.

[2] J. Wesson and D. J. Campbell, *Tokamaks*. Oxford University Press, 2011.

[3] P. C. Stangeby and G. M. McCracken, "Plasma boundary phenomena in tokamaks," *Nuclear Fusion*, vol. 30, no. 7, p. 1225, 1990.

[4] A. Kallenbach, M. Balden, R. Dux, T. Eich, C. Giroud, A. Huber, G. P. Maddison, M. Mayer, K. McCormick, R. Neu, T. W. Petrie, T. Pütterich, J. Rapp, M. L. Reinke, K. Schmid, J. Schweinzer, and S. Wolfe, "Plasma surface interactions in impurity seeded plasmas," *Journal of Nuclear Materials*, vol. 415, no. 1, pp. S19–S26, 2011.

[5] K. Schmid, A. Manhard, C. Linsmeier, A. Wiltner, T. Schwarz-Selinger, W. Jacob, and S. Mändl, "Interaction of nitrogen plasmas with tungsten," *Nuclear Fusion*, vol. 50, no. 2, p. 025006, 2010.

[6] G. F. Matthews, "Material migration in divertor tokamaks," *Journal of Nuclear Materials*, vol. 337-339, pp. 1–9, 2005.

[7] R. A. Pitts, P. Andrew, X. Bonnin, A. V. Chankin, Y. Corre, G. Corrigan, D. Coster, I. Duran, T. Eich, S. K. Erents, W. Fundamenski, A. Huber, S. Jachmich, G. Kirnev, M. Lehnen, P. J. Lomas, A. Loarte, G. F. Matthews, J. Rapp, C. Silva, M. F. Stamp, J. D. Strachan, and E. Tsitrone, "Edge and divertor physics with reversed toroidal field in JET," *Journal of Nuclear Materials*, vol. 337-339, pp. 146–153, 2005.

[8] A. Hakola, M. I. Airila, C. Björkas, D. Borodin, S. Brezinsek, J. P. Coad, M. Groth, A. Järvinen, A. Kirschner, S. Koivuranta, K. Krieger, T. Kurki-Suonio, J. Likonen, V. Lindholm, T. Makkonen, M. Mayer, J. Miettunen, H. W. Müller, R. Neu, P. Petersson, V. Rohde, M. Rubel, and A. Widdowson, "Global migration of impurities in tokamaks," *Plasma Physics and Controlled Fusion*, vol. 55, no. 12, p. 124029, 2013.

[9] G. Meisl, K. Schmid, O. Encke, T. Höschen, L. Gao, and C. Linsmeier, "Implantation and erosion of nitrogen in tungsten," *New journal of physics*, vol. 16, no. 9, p. 093018, 2014.

[10] G. Meisl, K. Schmid, K. Krieger, M. Oberkofler, S. W. Lisgo, and J. E. contributors, "Simulating the nitrogen migration in Be/W tokamaks with WallDYN," *Physica Scripta*, vol. T167, p. 014079, 2016.

[11] G. Meisl, K. Schmid, M. Oberkofler, K. Krieger, S. W. Lisgo, L. Aho-Mantila, F. Reimold, and T. Lunt, "Experimental analysis and WallDYN simulations of the global nitrogen migration in ASDEX Upgrade L-mode discharges," *Nuclear Fusion*, vol. 56, no. 3, p. 036014, 2016.

[12] G. Meisl, M. Oberkofler, A. Hakola, K. Krieger, K. Schmid, S. W. Lisgo, M. Mayer, A. Lahtinen, A. Drenik, S. Potzel, L. Aho-Mantila, and A. U. Team, "Nitrogen transport in ASDEX Upgrade: Role of surface roughness and transport to the main wall," *Nuclear Materials and Energy*, vol. 12, pp. 51–59, 2017.

[13] K. Schmid and T. Lunt, "3D global impurity transport modeling with WallDYN and EMC3-Eirene," *Nuclear Materials and Energy*, vol. 17, pp. 200–205, 2018.

[14] H.-S. Bosch and G. Hale, "Improved formulas for fusion cross-sections and thermal reactivities," *Nuclear Fusion*, vol. 32, no. 4, pp. 611–631, 1992.

[15] U. Stroth, *Plasmaphysik: Phänomene, Grundlagen, Anwendungen*. Berlin, Heidelberg: Springer Berlin Heidelberg, 2018.

[16] J. D. Lawson, "Some Criteria for a Power Producing Thermonuclear Reactor," *Proceedings of the Physical Society. Section B*, vol. 70, no. 1, pp. 6–10, 1957.

[17] J. Ongena, R. Koch, R. Wolf, and H. Zohm, "Magnetic-confinement fusion," *Nature Physics*, vol. 12, no. 5, pp. 398–410, 2016.

[18] D. Maisonnier, I. Cook, S. Pierre, B. Lorenzo, P. Di Luigi, G. Luciano, N. Prachai, and P. Aldo, "DEMO and fusion power plant conceptual studies in Europe," *Fusion Engineering and Design*, vol. 81, no. 8-14, pp. 1123–1130, 2006.

[19] A. Loarte, *Required R&D in Existing Fusion Facilities to Support the ITER Research Plan*. 2020.

[20] H. Zohm, *Magnetohydrodynamic stability of tokamaks*. John Wiley & Sons, 2014.

[21] D. M. Harting, *3-dimensionale Plasmarandschicht-Simulationen in unvollständig ergodisierten Magnetfeldern*. PhD thesis, 2008.

[22] M. A. Leontovich, *S. I. Braginskii in Reviews of Plasma Physics, Vol.1 p. 205*. New York, NY: Springer, 1970.

[23] J.-Y. Ji and E. D. Held, "Closure and transport theory for high-collisionality electron-ion plasmas," *Physics of Plasmas*, vol. 20, no. 4, p. 042114, 2013.

[24] P. C. Stangeby *et al.*, *The Plasma Boundary of Magnetic Fusion Devices*, vol. 224. Institute of Physics Publishing Bristol, 2000.

[25] Spitzer, *Physics of Fully Ionized Gases*. Wiley New York, 2 ed., 1962.

[26] K. Schmid, M. Reinelt, and K. Krieger, "An integrated model of impurity migration and wall composition dynamics for tokamaks," *Journal of Nuclear Materials*, vol. 415, no. 1, pp. S284–S288, 2011.

[27] W. Eckstein, *Computer Simulation of Ion-Solid Interactions*, vol. v.10 of *Springer Series in Materials Science Ser.* Berlin, Heidelberg: Springer Berlin / Heidelberg, 1991.

[28] C. García-Rosales, W. Eckstein, and J. Roth, "Revised formulae for sputtering data," *Journal of Nuclear Materials*, vol. 218, no. 1, pp. 8–17, 1995.

[29] Y. Yamamura, N. Matsunami, and N. Itoh, "Theoretical studies on an empirical formula for sputtering yield at normal incidence," *Radiation Effects*, vol. 71, no. 1-2, pp. 65–86, 1983.

[30] Y. Yamamura, "A simple analysis of the angular dependence of light-ion sputtering," *Nuclear Instruments and Methods in Physics Research Section B: Beam Interactions with Materials and Atoms*, vol. 2, no. 1-3, pp. 578–582, 1984.

[31] M. Mayer, S. Möller, M. Rubel, A. Widdowson, S. Charisopoulos, T. Ahlgren, E. Alves, G. Apostolopoulos, N. P. Barradas, S. Donnelly, S. Fazinić, K. Heinola, O. Kakuee, H. Khodja, A. Kimura, A. Lagoyannis, M. Li, S. Markelj, M. Mudrinic, P. Petersson, I. Portnykh, D. Primetzhofer, P. Reichart, D. Ridikas, T. Silva, S. M. Gonzalez de Vicente, and Y. Q. Wang, "Ion beam analysis of fusion plasma-facing materials and components: facilities and research challenges," *Nuclear Fusion*, vol. 60, no. 2, p. 025001, 2020.

[32] F. B. Hagedorn and J. B. Marion, "Further Investigation of N15 + p Reactions," *Physical Review*, vol. 108, no. 4, pp. 1015–1019, 1957.

[33] L. C. Feldman, J. W. Mayer, and M. Grasserbauer, "Fundamentals of surface and thin film analysis," *Analytica Chimica Acta*, vol. 199, p. 288, 1987.

[34] P. Virtanen, R. Gommers, T. E. Oliphant, M. Haberland, T. Reddy, D. Cournapeau, E. Burovski, P. Peterson, W. Weckesser, J. Bright, S. J. van der Walt, M. Brett, J. Wilson, K. J. Millman, N. Mayorov, A. R. J.

Nelson, E. Jones, R. Kern, E. Larson, C. J. Carey, İ. Polat, Y. Feng, E. W. Moore, J. VanderPlas, D. Laxalde, J. Perktold, R. Cimrman, I. Henriksen, E. A. Quintero, C. R. Harris, A. M. Archibald, A. H. Ribeiro, F. Pedregosa, and P. van Mulbregt, "SciPy 1.0: fundamental algorithms for scientific computing in Python," *Nature methods*, vol. 17, no. 3, pp. 261–272, 2020.

[35] H. Maier, S. Kötterl, K. Krieger, R. Neu, M. Balden, and A. Upgrade-Team, "Performance of tungsten coatings as plasma facing components used in ASDEX Upgrade," *Journal of Nuclear Materials*, vol. 258-263, pp. 921–926, 1998.

[36] R. Neu, "High- Z plasma facing components in fusion devices: boundary conditions and operational experiences," *Physica Scripta*, vol. T123, pp. 33–44, 2006.

[37] F. Wagner, G. Fussmann, T. Grave, M. Keilhacker, M. Kornherr, K. Lackner, K. McCormick, E. R. Müller, A. Stäbler, G. Becker, K. Bernhardi, U. Ditte, A. Eberhagen, O. Gehre, J. Gernhardt, G. v. Gierke, E. Glock, O. Gruber, G. Haas, M. Hesse, G. Janeschitz, F. Karger, S. Kissel, O. Klüber, G. Lisitano, H. M. Mayer, D. Meisel, V. Mertens, H. Murmann, W. Poschenrieder, H. Rapp, H. Röhr, F. Ryter, F. Schneider, G. Siller, P. Smeulders, F. Söldner, E. Speth, K.-H. Steuer, Z. Szymanski, and O. Vollmer, "Development of an Edge Transport Barrier at the H-Mode Transition of ASDEX," *Physical Review Letters*, vol. 53, no. 15, pp. 1453–1456, 1984.

[38] M. Keilhacker, "H-mode confinement in tokamaks," *Plasma Physics and Controlled Fusion*, vol. 29, no. 10A, pp. 1401–1413, 1987.

[39] A. Herrmann and O. Gruber, "ASDEX Upgrade - Introduction and overview," *Fusion Science and Technology*, vol. 44, no. 3, pp. 569–577, 2003.

[40] P. J. McCarthy, P. Martin, and W. Schneider, "The CLISTE interpretive equilibrium code, Technical Report IPP 5/85," 1999.

[41] I. H. Hutchinson, "Principles of plasma diagnostics," *Plasma Physics and Controlled Fusion*, vol. 44, no. 12, p. 2603, 2002.

[42] B. Kurzan and H. D. Murmann, "Edge and core Thomson scattering systems and their calibration on the ASDEX Upgrade tokamak," *The Review of scientific instruments*, vol. 82, no. 10, p. 103501, 2011.

[43] M. Bernert, T. Eich, A. Burckhart, J. C. Fuchs, L. Giannone, A. Kallenbach, R. M. McDermott, B. Sieglin, and ASDEX Upgrade Team, "Application of AXUV diode detectors at ASDEX Upgrade," *Rev. Sci. Instrum.*, vol. 53, no. 3, p. 104003, 2014.

[44] B. Sieglin, M. Faitsch, A. Herrmann, B. Brucker, T. Eich, L. Kammerloher, and S. Martinov, "Real time capable infrared thermography for ASDEX Upgrade," *Rev. Sci. Instrum.*, vol. 86, no. 11, p. 113502, 2015.

[45] A. Herrmann, W. Junker, K. Gunther, S. Bosch, M. Kaufmann, J. Neuhauser, G. Pautasso, T. Richter, and R. Schneider, "Energy flux to the ASDEX Upgrade diverter plates determined by thermography and calorimetry," *Plasma Physics and Controlled Fusion*, vol. 37, no. 1, p. 17, 1995.

[46] M. Weinlich and A. Carlson, "Flush mounted probes in ASDEX Upgrade - Can they be operated as triple probes?," *Contributions to Plasma Physics*, vol. 36, no. S1, pp. 53–59, 1996.

[47] K. Krieger, V. Rohde, R. Schwörer, K. Asmussen, C. García-Rosales, A. Hermann, R. Neu, J. Roth, A. Thoma, and M. Weinlich, "Migration of tungsten eroded from divertor tiles in ASDEX Upgrade," *Journal of Nuclear Materials*, vol. 241-243, pp. 734–738, 1997.

[48] A. Herrmann, N. Jaksic, P. Leitenstern, H. Greuner, K. Krieger, P. de Marné, M. Oberkofler, V. Rohde, and G. Schall, "A large divertor manipulator for ASDEX Upgrade," *Fusion Engineering and Design*, vol. 98-99, pp. 1496–1499, 2015.

[49] R. J. Fonck, "Charge exchange recombination spectroscopy as a plasma diagnostic tool (invited)," *Review of Scientific Instruments*, vol. 56, no. 5, pp. 885–890, 1985.

[50] R. M. McDermott, R. Dux, T. Pütterich, B. Geiger, A. Kappatou, A. Lebschy, C. Bruhn, M. Cavedon, A. Frank, N. den Harder, and E. Viezzer, "Evaluation of impurity densities from charge exchange recombination spectroscopy measurements at ASDEX Upgrade," *Plasma Physics and Controlled Fusion*, vol. 60, no. 9, p. 095007, 2018.

[51] E. Wolfrum, F. Aumayr, D. Wutte, H. P. Winter, E. Hintz, D. Rusbüldt, and R. P. Schorn, "Fast lithium-beam spectroscopy of tokamak edge plasmas," *Rev. Sci. Instrum.*, vol. 64, no. 8, pp. 2285–2292, 1993.

[52] J. Schweinzer, E. Wolfrum, F. Aumayr, M. Pockl, H. Winter, R. P. Schorn, E. Hintz, and A. Unterreiter, "Reconstruction of plasma edge density profiles from Li I (2s-2p) emission profiles," *Plasma Physics and Controlled Fusion*, vol. 34, no. 7, p. 1173, 1992.

[53] R. Fischer, C. J. Fuchs, B. Kurzan, W. Suttrop, and E. Wolfrum, "Integrated Data Analysis of Profile Diagnostics at ASDEX Upgrade," *Fusion Science and Technology*, vol. 58, no. 2, pp. 675–684, 2010.

[54] R. Fischer, C. Wendland, A. Dinklage, S. Gori, V. Dose, and t. W.-A. team, "Thomson scattering analysis with the Bayesian probability theory," *Plasma Physics and Controlled Fusion*, vol. 44, no. 8, pp. 1501–1519, 2002.

[55] R. Fischer, E. Wolfrum, J. Schweinzer, *et al.*, "Probabilistic lithium beam data analysis," *Plasma Physics and Controlled Fusion*, vol. 50, no. 8, p. 085009, 2008.

[56] B. Streibl, P. T. Lang, F. Leuterer, J.-M. Noterdaeme, and A. Stäbler, "Chapter 2: Machine Design, Fueling, and Heating in ASDEX Upgrade," *Fusion Science and Technology*, vol. 44, no. 3, pp. 578–592, 2003.

[57] G. Meisl, K. Schmid, M. Oberkofler, K. Krieger, S. W. Lisgo, L. Aho-Mantila, and F. Reimold, "Nitrogen retention in ASDEX Upgrade," *Journal of Nuclear Materials*, vol. 463, pp. 668–671, 2015.

[58] A. Kallenbach, R. Dux, J. C. Fuchs, R. Fischer, B. Geiger, L. Giannone, A. Herrmann, T. Lunt, V. Mertens, R. McDermott, R. Neu, T. Pütterich, S. Rathgeber, V. Rohde, K. Schmid, J. Schweinzer, and W. Treutterer, "Divertor power load feedback with nitrogen seeding in ASDEX Upgrade," *Plasma Physics and Controlled Fusion*, vol. 52, no. 5, p. 055002, 2010.

[59] Y. Feng, F. Sardei, J. Kisslinger, and P. Grigull, "A 3D Monte Carlo code for plasma transport in island divertors," *J. Nucl. Mater.*, vol. 241, pp. 930–934, 1997.

[60] Y. Feng *et al.*, "Formulation of a Monte Carlo model for edge plasma transport," in *27. EPS Conf. on Plasma Physics, Budapest, Hungaria, vol. 24B, pp. 1188-91*, 2000.

[61] D. Reiter, "EIRENE Documentation."

[62] Y. Feng *Contributions to Plasma Physics*, vol. 44, no. 1-3, pp. 25–30, 2004.

[63] D. Reiter and D. Harting, "3D Monte-Carlo-Simulation der ergodisierten Randschicht von TEXTOR-DED."

[64] W. Möller, W. Eckstein, and J. P. Biersack, "Tridyn-binary collision simulation of atomic collisions and dynamic composition changes in solids," *Computer Physics Communications*, vol. 51, no. 3, pp. 355–368, 1988.

[65] A. Mutzke, R. Schneider, W. Eckstein, R. Dohmen, K. Schmid, U. von Toussaint, and G. Badelow, "SDTrimSP Version 6.00."

[66] K. Schmid, A. Manhard, C. Linsmeier, A. Wiltner, T. Schwarz-Selinger, W. Jacob, and S. Mändl, "Interaction of nitrogen plasmas with tungsten," *Nuclear Fusion*, vol. 50, no. 2, p. 025006, 2010.

[67] S. Wiesen, D. Reiter, V. Kotov, M. Baelmans, W. Dekeyser, A. S. Kukushkin, S. W. Lisgo, R. A. Pitts, V. Rozhansky, G. Saibene, I. Veselova, and S. Voskoboynikov, "The new SOLPS-ITER code package," *Journal of Nuclear Materials*, vol. 463, pp. 480–484, 2015.

[68] P. C. Stangeby and J. D. Elder, "Calculation of observable quantities using a divertor impurity interpretive code, DIVIMP," *Journal of Nuclear Materials*, vol. 196-198, pp. 258–263, 1992.

[69] L. Bock, D. Brida, M. Faitsch, K. Schmid, T. Lunt, and t. A. U. team, "Comparison of the influence of 2D and 3D geometry of the main chamber on plasma parameters in the SOL of ASDEX Upgrade," *Nuclear Fusion*, vol. 62, no. 2, p. 026020, 2022.

[70] H. J. Sun, E. Wolfrum, B. Kurzan, T. Eich, K. Lackner, A. Scarabosio, I. P. Pérez, O. Kardaun, M. Faitsch, S. Potzel, and U. Stroth, "Study of near SOL decay lengths in ASDEX Upgrade under attached and detached divertor conditions," *Plasma Physics and Controlled Fusion*, vol. 59, no. 10, p. 105010, 2017.

[71] T. Eich, P. Manz, and t. A. U. team, "The separatrix operational space of ASDEX Upgrade due to interchange-drift-Alfvén turbulence," *Nuclear Fusion*, vol. 61, no. 8, p. 086017, 2021.

[72] A. V. Chankin and D. P. Coster, "Comparison of 2D models for the plasma edge with experimental measurements and assessment of deficiencies," *Journal of Nuclear Materials*, vol. 390-391, pp. 319–324, 2009.

[73] M. Wischmeier, M. Groth, A. Kallenbach, A. V. Chankin, D. P. Coster, R. Dux, A. Herrmann, H. W. Müller, R. Pugno, D. Reiter, A. Scarabosio, and J. G. Watkins, "Current understanding of divertor detachment: Experiments and modelling," *Journal of Nuclear Materials*, vol. 390-391, pp. 250–254, 2009.

[74] W. Hu, S. Dai, A. Kirschner, and D. Wang, "Surface roughness effects on plasma near a divertor plate and local impact angle," *Nuclear Materials and Energy*, vol. 12, pp. 313–317, 2017.